if we call light, those rays which illuminate objects, and radiant heat, those which heat bodies,
it may be inquired whether light be essentially different from radiant heat?

William Hershel, 1817

Seas, lakes and great bodies of water, agitated by winds, continually change their surfaces;
the cold surface in winter is turned under, by the rolling of the waves, and a warmer turned up;
in summer, the warm is turned under, and colder turned up.
Hence the more equal temper of sea-water, and of the air over it.

Franklin, 1765

Chapter 3
Radiation, Heat Transport, and Temperature

Overview: Primed by mental models (Chapter 1) and aware of data limitations (Chapter 2) we begin our exploration where the circulation initiates: radiant energy input, reflection, absorption, and emission. Corresponding observed transports of heat and energy balance are shown. Emission and heat transport depend on an associated distribution of temperature whose structure and general properties are explained with simple models.

In chapter 1 the zonal and annual average distribution of absorption and emission were described in general terms (recall Figure 1.1); in this chapter radiation and its links to heat flow and temperature are examined in more detail.

3.1 Radiation

3.1.1 Basic Concepts

Atmospheric radiation can be expressed as radiance (E) and irradiance (I). I is the total amount of radiant energy actually passing through (or arriving at) an area. E is the amount of I passing through (or arriving at) an area in (from) a particular direction. Both radiance and irradiance are expressed either for a single electromagnetic wavelength (Λ) or integrated over all such wavelengths; in the latter case, the units are usually W/m^2. It is common to use hemispheres to separate the radiation coming from below (‘up’) from that coming from above (‘down’). The

radiative balance models discussed later in this chapter employ this device. As detailed in Appendix D, the irradiance equals the radiance times the solid angle of the emitter for parallel beam radiation (assumed to apply to solar radiation at the Earth's orbit).

Various relationships between E, I, Λ, and temperature T are reviewed in Appendix D. Planck's law of blackbody radiation defines the *monochromatic radiance*, E_Λ (or *spectral radiance*) as the amount of electromagnetic radiant energy flux passing through a given area at wavelength Λ for a given blackbody temperature (*T*) from a specific direction.. Planck's law contains two functions of Λ that cause E_Λ to asymptote to zero both for very large and very small wavelengths with a maximum emission at an intermediate wavelength for a given temperature. The Λ of maximum emission for a specified T is given by Wein's law. The peak emission shifts to a longer wavelength for a cooler temperature of the emitter.

Solar irradiance is shown in Figure 3.1 and terrestrial radiation for several locations in Figure 3.2. The latter figure has smooth blackbody radiance curves of E_Λ calculated from Planck's law that show the shift of peak emission with temperature. Planck's law also shows that the higher the temperature, the larger the values of E_Λ at all wavenumbers. All these features are evident in Figures 3.1 and 3.2.

As illustrated in Figures 3.1 and 3.2, Earth and the surface of the Sun have very different temperatures. Though the Sun has far higher radiance from its surface than Earth, the Sun is far away compared to the distances between emitters and absorbers of terrestrial radiation. Since the net gain of radiant solar energy equals the net emission of terrestrial radiation to space (for energy balance) one can apply a multiplier to the solar spectrum relative to the terrestrial spectra at Earth's orbit which makes the radiance in the visible wavelengths much higher for the solar than the terrestrial radiance. The same multiplier makes the solar radiation much less than the terrestrial for wavelengths near the maximum of terrestrial radiation. Accordingly, the spectra of E_Λ for the Earth and the Sun (at Earth's orbit) have very little overlap. Hence, it is customary to assign one part of the electromagnetic spectrum to solar and one part to terrestrial radiation. The solar radiation is frequently referred to as the "shortwave" radiation while the terrestrial radiation is called the "longwave" radiation. These labels will be used interchangeably.

3.1.2 Global Average Observed Radiation

Planck's law predicts the radiant emission spectrum from a black body to vary smoothly with electromagnetic wavenumber. The emission spectrum from the Sun only approximately varies as predicted by Planck's law. The solar spectral irradiance I_Λ, reaching the Earth is shown

as the higher continuous curve in Figure 3.1. For reference, * symbols plot emission values for a blackbody with T=5620K, a temperature chosen to have a similar wavelength of maximum emission from Wein's law. About half of the solar irradiance reaching Earth occurs in near-infrared wavelengths of 0.7 to 3 μm; ~45% is in the visible range of 0.38 to 0.74 μm; and ~5% is in the ultraviolet range of 0.1 to 0.4 μm. The lower curve is the solar radiation reaching the Earth's surface for clear sky conditions and the sun directly overhead. Part of the region between these two continuous curves is shaded and estimates the amount of absorption of solar radiation by atmospheric gases; wavelengths with larger amounts of absorption are labeled with the primary absorbing gas at those wavelengths. The clear area between the two continuous curves is an estimate of the amount of scattered solar radiation. The scattering is comparatively small for the infrared wavelengths (0.8 – 1000 μm) but becomes much stronger in the near-ultraviolet (~0.3 - 0.4 μm). The human eye cannot see ultraviolet light; the closest wavelengths it can see are perceived as the color purple (~0.43 μm). While the fractional scattering is greater for purple, the solar radiance is greater for blue (~ 0.45 – 0.5 μm). Scattering is a type of reflection, where the incoming light is reflected into different directions. For clean air, these reflections are uniformly distributed in different directions. This strong scattering is why the sky is a rather uniform blue at midday. (Many other factors influence the actual sky color such as the presence of pollutants, the longer path through the air in directions close to the horizon, etc.)

The longwave terrestrial radiation varies greatly from place to place due to temperature variation of the primary emitting surface. The primary emitting surface varies with the wavelength of electromagnetic emission. For some wavelengths the atmosphere is nearly transparent and emission is from the Earth's surface. Temperature varies considerably across the surface and with altitude in the atmosphere. The emission from high mountains or cold polar regions differs from hot subtropical desert surfaces. If thick clouds are present, the infrared emission is primarily from the tops of those clouds. For other wavelengths the cloud-free atmosphere absorbs strongly and emission is primarily from a level in the atmosphere and temperature varies strongly with atmospheric elevation. The level of primary emission is related to the concentration of the absorber along the path followed by the radiation, as will be shown later in this chapter (when radiative balance models are described). For the discussion here, it is sufficient to know that wavelengths strongly absorbed by the atmosphere will, from Kirchhoff's law also be equally strongly emitted by the atmosphere. From Wien's law the maximum emission by a black body for terrestrial surface and atmospheric temperatures occurs at infrared wavelengths. Hence, the atmospheric gases that absorb radiation strongly in the infrared wavelengths, sometimes called 'greeenhouse gases', are the most important for terrestrial radiative balance. The primary greenhouse gas is water vapor (H_2O). The next most important

greenhouse gas is carbon dioxide (CO_2). There are other gases with minor, but notable absorption, such as ozone (O_3) and methane (CH_4).

Figure 3.2a shows the terrestrial radiance spectrum measured by a polar orbiting satellite looking down as it passed over Guam island at a specific date and time. Because temperature varies over the surface, the spectrum looks different measured from a polar region (generally lower values at most wavelengths) and from a hot desert region (generally higher values at most wavelengths). Figure 3.2b illustrates both extremes. These differences can be estimated from the smooth lines plotted on the figure that show blackbody radiance spectra for different emitter temperatures. Though the actual emission varies from place to place, there are some consistencies that are emphasized here.

Figure 3.2 indicates higher radiance values in the wavelengths from about 8 to 14 μm. This range of wavelengths is sometimes called the primary 'atmospheric window'. The name makes clear that emission at these wavelengths largely passes through the atmosphere without absorption. Consequently, the radiance reflects surface temperatures (~295K in figure 3.2a, a reasonable temperature near the surface at this locale). There is a secondary and less transparent atmospheric window for wavelengths of about 16 to 22 μm. The figure also shows wavelengths for which specific absorbing gases are more prominent, such as ozone from 9.4 to 9.8 μm, and both CO_2 and H_2O near 14-16 μm. Water vapor is the strongest greenhouse gas based on the prevalence of wavelengths absorbed and the amount of drop in radiance. (Water vapor is also a strong absorber of shortwave irradiance, as deduced from figure 3.1.) Where there is strong absorption, the main emission is effectively from a higher and thus colder atmospheric level. The blackbody emission curves illustrate Wien's law, with the maximum emission occurring at longer wavelengths for colder temperatures. Also notable in passing is the blackbody emission is less at all wavelengths for a colder temperature.

The units in figure 3.1 differ from 3.2 as does the magnitude. To discuss energy balance, it is useful to deduce the total amount of solar radiant energy reaching the Earth (known as the 'solar constant'). The solar constant is both an integral over the electromagnetic wavelengths of the solar irradiance and also must account for the distance between the Sun and Earth. That Earth-Sun distance defines a small solid angle on a sphere whose radius is the Earth-Sun distance. One can estimate the solar spectral irradiance from the solar blackbody radiance (D.5) times the ratio of the distances (Sun radius over one astronomical unit) squared times pi (to obtain solid angle and thus irradiance). The result for 5620K temperature is plotted in figure 3.1. One can estimate the solar constant (I_{Sol}, solar irradiance at the Earth's orbit) from the Stefan-Boltzmann law (D.11) times that same ratio squared times pi. Estimates of the solar constant vary between 1356 and 1370 W/m^2 (see Trenberth et al., 2009, for a review). The estimate for

6000K is I_{Sol} =1595 W/m^2 which is too high, hence an effective blackbody temperature of the Sun is lower (~5772K) for I_{Sol} =1365 W/m^2 used here.

The atmospheric absorption of the electromagnetic radiation has extremely important implications for the planet. Both the absorption and the scattering of the solar radiation at very short wavelengths ($\leq 0.4\mu$m) greatly favors many complex life forms on the planet. The high energy of ultraviolet light is known to damage many plants and may adversely affect the health of animals. (Life is relevant to our discussion since life is necessary to maintain the atmosphere's present chemical composition. Plants significantly alter the surface budgets of momentum, energy, and moisture, too.) Absorption of longwave radiation also greatly favors the development of life on Earth by elevating the temperature of the Earth and its atmosphere. Without the longwave atmospheric absorption, the Earth's surface would be much cooler. Instead, the average temperature of the Earth's surface is kept high enough to permit liquid water to occur. (This longwave absorption is sometimes erroneously referred to as the "greenhouse effect"; in actuality a greenhouse builds elevated temperatures by trapping air in a confined space.)

Solar spectral irradiance reaching the Earth is reflected, transmitted, and absorbed by the atmosphere and reflected and absorbed by the surface, in complex ways. Similarly, the longwave emission from the Earth's surface and atmosphere (including clouds) is also complex. A starting point for discussion of the atmospheric radiation is to consider energy balance between solar energy gain and infrared loss to space.

The global radiative energy balance is diagrammed schematically in Figure 3.3. Budgets for the earth's surface, the atmosphere, and outer space are given. Of course, the total amount absorbed or emitted must balance, otherwise the earth or atmosphere would experience a net heating up or cooling down. As anticipated above, Figure 3.3 partitions the energy into shortwave and longwave components. The presentation includes both actual irradiances as well as their percentage of the total shortwave energy encountering the top of the atmosphere (TOA). That total amount reaching the TOA varies with latitude, season, and time of day. However, a global annual mean balance is shown first. In this global balance the amount of radiation intercepted by the Earth equals its cross sectional area. The Earth rotates on its axis spreading the intercepted radiation over the entire Earth (at the equinoxes). The surface area of the Earth is four times the cross sectional area, hence the global incoming solar irradiance is $I_S = I_{Sol}/4 \sim 341$ W/m^2.

Figure 3.3 summarizes the global energy balances for the Earth system, where separate balances are shown for the Earth and space, for the whole atmosphere, and for the Earth's surface. The figure separates the partitioning of solar energy input on the left from the terrestrial

energy elements on the right. Various authors have estimated these elements and a summary can be found in the primary reference used for this figure (Trenberth et al., 2009). The numbers are challenging to obtain with precision and some numbers are estimated; it is customary to adjust the numbers so that there is a balance for each part of the Earth system. Trenberth et al. (2009) chose not to make a full adjustment and leave a net absorption of 0.9 Wm^{-2} energy gain (from Hansen et al., 2005) by the Earth. In addition, more recent work (Stephens et al., 2012) obtains different values. Some differences in Stephens et al include: less solar reflection by clouds (47.5 ±3 Wm^{-2}), less solar absorption by clouds (5 ±5 Wm^{-2}), but more atmospheric solar absorption (75 ±10 Wm^{-2}) and solar reflection (27.2 ±4.6 Wm^{-2}). In the longwave radiation, Stephens et al have greater surface fluxes (SHF =24 ±7 and LHF=88 ±10 W/m^2) that result in a greater downward longwave radiation from the atmosphere at the surface (345.6 ±9). Hence, the primary purpose of this diagram resides not in the precise numbers but to illuminate the relative proportionalities of the elements shown. To facilitate illustrating the proportions, both the unitary value and the percentage of the solar input (I_S) are indicated.

The shortwave radiation has these global properties in Figure 3.3: about 30% of I_S is reflected back to space; this reflection is labeled the albedo (A_{lbd}). Much of the reflection is from clouds (18%) while about 5% is the scattering (primarily of blue and purple wavelengths of sunlight). Only about half of I_S reaches the surface and a small fraction, about 12-13% of that is reflected back to space. While snow covered surfaces and deserts have high albedo, most of the Earth is covered by dark oceans and forests having small albedo. The remaining fraction of sunlight, less than a quarter of I_S, is absorbed by the atmosphere and its clouds.

The Earth's surface absorbs 47% of solar radiant energy but also absorbs a larger amount (energy equivalent to 98% of I_S) that is emitted downward by the atmosphere. Earth's surface loses energy by three means: infrared emission, evaporating water (surface latent heat fluxes, SLHF), and surface sensible heat fluxes (SSHF). The atmosphere also gained energy, from absorbing sunlight, from absorbing longwave emission by the Earth's surface, plus the SLHF and SSHF.

Examining the heat fluxes finds the latent heat fluxes to be 4-5 times as large as the sensible heat fluxes. The atmosphere gains energy from the sensible heating at its lowest levels, by conduction and small scale turbulent mixing leading to convective thermals or mechanical mixing into higher altitudes. The energy from the latent heat flux is mixed vertically in a similar manner however that energy is not released into heating the air until the moisture condenses. The condensation can occur a great distance from the location of the latent heat surface flux. Condensation of the moisture input by those latent heat fluxes also plays a major role in the

general circulation; for example, it is the major driving mechanism of the Hadley circulation (Chapter 10).

The emission from the tops of clouds (equivalent to 9% of I_S) has a significant role in the diabatic energy conversions (Chapter 7) and the diabatic forcing of the zonal mean meridional circulations (Chapter 10).

Excluding the solar radiation reflected and scattered by the atmosphere as not available to heat the Earth system, the atmosphere is more transparent to shortwave radiation (54/77*100=70% passes through) than to longwave radiation (40/396=10% passes through). Simple models (next) show that the atmosphere being more transparent to shortwave radiation than to longwave radiation elevates the temperatures of the Earth's surface above expectations based only on absorbed solar energy, a property sometimes called the 'greenhouse effect'. The effect is evident in Figure 3.3 as the large downward and upward longwave emissions between atmosphere and surface.

3.1.3 Models of Global Average Radiative Trapping

A simple analogy using a ping pong ball to represent a unit of radiant energy may be helpful in visualizing the effect. The solar radiation absorbed by the earth is represented by the impact of a ping pong ball as it is thrown toward the floor, one ball each minute. The floor represents the earth, so that the upward rebound of the ball represents the net infrared emission from the earth. The atmosphere might be thought of as a table. When tossed downward, the ball bounces off the floor, then off the underside of the table, and again off the floor before it escapes, that last representing exit to space. In this trivial model, the radiant energy received by the "Earth" is twice the incoming value because the ball must bounce off the floor *twice* before it escapes.

A simple quantitative model is the 'glass slab' model, versions of which can be found in various sources. 'Glass' in this context highly simplifies the atmosphere as a substance which is more transparent in visible than in infrared wavelengths and since it is a solid, so no effects from an 'atmospheric' circulation are included. The albedo from reflection and scattering off the atmosphere and off the surface is already removed to specify the shortwave radiation input (I_{IN}). Similarly, the longwave emissivity of the surface is assumed to be 1, i.e. the surface is a 'blackbody'. Figure 3.4 describes the model components, where subscripts designate: 'A' for atmosphere, 'G' for surface, 'S' for shortwave, and 'L' for longwave. The longwave emission from the atmospheric 'glass slab' is in all directions upward and all directions downward while the corresponding emission from the surface is only all directions upward. I_S is as before.

Irradiance from the surface and from the atmosphere are uniquely determined from radiative balance of the surface and atmosphere once the four absorptivities present are specified. From those irradiances, the Stefan-Boltzmann law, with appropriate emissivity, obtains surface and atmospheric temperatures.

Radiative balance for the atmosphere in the glass slab model is

$$a_{SA}\, I_{IN} + a_{LA}\, I_G = 2\, a_{LA}\, I_A \tag{3.1}$$

Corresponding radiative balance for the surface is

$$a_{SG}\, I_{IN} + a_{LA}\, I_A = I_G \tag{3.2}$$

The I_A as used in (3.1) and (3.2) is the black body irradiance because the gray body emissivity of the atmosphere (a_{LA}) is included explicitly in these equations and in the corresponding figure. This pair of equations can be solved to obtain

$$a_{LA}\ I_A = I_{IN}\left(\frac{a_{SA} + a_{LA} - a_{SA}\, a_{LA}}{2 - a_{LA}}\right) \tag{3.3}$$

And

$$I_G = I_{IN}\left(\frac{2 - a_{SA}}{2 - a_{LA}}\right) \tag{3.4}$$

To obtain the temperatures of atmosphere and surface, solve for T_A and T_G from

$$I_G = \sigma T_G^4 \tag{3.5}$$

And

$$I_A = \sigma T_A^4 \tag{3.6}$$

The 'greenhouse' effect is clear from (3.4) that if $a_{LA} > a_{SA}$ then $I_G > I_{IN}$ and the irradiance, and therefore the temperature of the surface, is greater than if it were based solely on the solar irradiance absorbed. The extremes of (3.4) are instructive. If the atmosphere were completely transparent to shortwave and completely opaque to longwave radiation, then the surface irradiance would be twice the solar input. For values in Figure 3.3, since $a_{SA} = 0.3$ and $a_{LA} = 0.9$ the factor multiplying I_{IN} in (3.4) is ~1.52. Similarly, Figure 3.3 implies that $I_{IN} = 239$ W/m^2 making $I_G = 363$ W/m^2 and $T_G = 283$ K. Solving for the atmosphere, $I_A = 0.9424\ I_{IN} = 225.24$ W/m^2 and $T_A = 251$ K. For comparison, if there was no atmosphere, with the same albedo (=0.3), then $I_G = 239$ W/m^2 and $T_G = 255$ K.

Other aspects of the greenhouse effect may be deduced from the TOA radiative balance. With respect to outer space, Figure 3.4 indicates that $I_{IN} = a_{LA}\ I_A + (1\text{-}a_{LA})\ I_G$. The greenhouse effect is when $I_A < I_G$ then $I_G > I_{IN}$. If the atmosphere slab temperature did not change but the

longwave absorptivity increased, by increasing CO_2 perhaps, then the surface would need to be warmer so that radiation to space matched the absorbed input. Also, if the atmosphere slab was somehow *cooled* without changing the atmospheric absorptivity, then Earth's surface would have to be *warmer*.

The glass slab model can incorporate LHF and SHF and reveal changes to atmospheric and surface irradiances and temperatures via transferring those surface fluxes as direct input into the atmosphere (with equal reduction from the surface). Clouds are still neglected in the atmospheric emission in this simple model (though they could be included). The surface is again assumed black in longwave wavelengths. Radiation emitted by the air is assumed to be emitted isotropically, so that half of the energy is lost to space and half is emitted back down to earth. Figure 3.5 illustrates the minor modification to the glass slab model. It is clear that the atmospheric energy balance becomes

$$a_{SA}\, I_{IN} + SLHF + SSHF + a_{LA}\, I_G = 2\, a_{LA}\, I_A \tag{3.7}$$

One may compare (3.7) with (3.1). Similarly the surface balance

$$I_G = I_{GIN} + a_{LA}\, I_A = a_{SG} I_{IN} - SLHF - SSHF + a_{LA}\, I_A \tag{3.8}$$

One may compare (3.8) with (3.2). After some simple algebra one obtains

$$a_{LA}\ I_A = \frac{\left(a_{SA} + a_{LA} - a_{SA}\, a_{LA}\right) I_{IN} + \left(1 - a_{LA}\right)\left(SLHF\ +\ SSHF\right)}{2 - a_{LA}} \tag{3.9}$$

where the identity $1=a_{SA} + a_{SG}$ is used. Comparing (3.9) with (3.3) it is immediately obvious that I_A is increased by positive surface heat fluxes making the atmosphere warmer as expected. More interesting is the amount of increase becomes smaller for larger atmospheric absorptivity, a_{LA}. For an atmosphere opaque to longwave radiation, adding the latent and sensible heat fluxes does not change anything since that atmosphere would intercept all energy from the surface whether radiant or from surface heat fluxes. The surface irradiance becomes

$$I_G = \frac{\left(2 - a_{SA}\right) I_{IN}\ - \left(SLHF\ +\ SSHF\right)}{2 - a_{LA}} \tag{3.10}$$

It is immediately obvious that for positive surface heat fluxes the surface irradiance I_G decreases and so does the surface temperature. The decrease of I_G is more for larger a_{LA}. Interestingly, the change is asymmetric: the reduction in surface irradiance is larger than the corresponding increase of atmospheric irradiance ($a_{LA}\ I_A$) unless the atmosphere is transparent to longwave radiation. The energy is shuffled between atmosphere and surface by including the surface

fluxes, but the radiative balance at the top of the atmosphere is independent of both LHF and SHF.

The model still neglects motions, including those that redistribute heat vertically and horizontally, so it still is only a model of global quantities. For the values in Figure 3.3, then I_A = 235.7 W/m^2 and T_A = 253.7 K while I_G = 274.7 W/m^2 and T_G = 263.8 K. Hence T_A increases by almost 3K and T_G decreases by 19K when the observed surface fluxes are included.

The difference between the longwave radiation emitted from the surface and the longwave amount reaching the surface from the atmosphere is $I_G - a_{LA} I_A$ = 274.7-212.1 = 62.6 W/m^2 in the calculation above using surface heat fluxes. This difference compares favorably with the corresponding observed difference (396-333 = 63 W/m^2) in Figure 3.3. However, the magnitudes of the fluxes at the surface are much larger than in the glass slab model with surface fluxes. In contrast the glass slab model with surface fluxes has larger atmospheric flux to space (212.1 W/m^2) than observed (198 W/m^2). The glass slab model can create a larger atmospheric emission into the surface than out the top by dividing the glass slab into separate layers.

Figure 3.5b illustrates the notation used here for an atmosphere having 2 glass slabs. To simplify the formulas that the amount of absorber is assumed the same in both layers and the surface fluxes are again ignored. Hence $a_s = a_{s1} = a_{s2}$ and $a_L = a_{L1} = a_{L2}$. The radiance values in each layer become

$$a_L I_2 = \frac{a_L a_S (1-a_S) + \left(a_L (1-a_S)\right)^2 + a_S + a_L (1-a_L)(1-a_S)^2}{2 - a_L (1-a_L)^2 - (a_L)^2 (2-a_L)} I_{IN} \qquad (3.11)$$

And

$$a_L I_1 = \frac{\left\{a_S + a_L (1-a_L)(1-a_S)^2\right\} a_L (2-a_L) + \left\{a_S (1-a_S) + a_L (1-a_S)^2\right\}\left(2 - a_L (1-a_L)\right)}{(2-a_L)\left(2 - a_L (1-a_L)^2\right) - \left(a_L (2-a_L)\right)^2} I_{IN} \qquad (3.12)$$

And the surface energy balance

$$I_G = (1-a_S)^2 I_{IN} + a_L I_1 + a_L (1-a_L) I_2 \qquad (3.13)$$

The formulas for I_2 and I_1 can be used to find the value of I_G. Since $0.67 = (1-a_S)^2$ then a_S = 0.18146 and since $0.1 = (1-a_L)^2$ then a_L = 0.68377. Using these values and I_{IN} = 239 Wm^{-2} finds I_2 =180.3 Wm^{-2} , I_1 =295.7 Wm^{-2} , I_G =401.3 Wm^{-2}.

These values have the asymmetry noted above, and are closer to the values seen in figure 3.3. The disparity between the net atmospheric emission towards the surface versus towards space can be explained by looking at figure 3.5b. Simplifying the figure further so that the

atmosphere has no solar absorption and each layer is 'black' obtains very simple balances for each atmospheric layer: $I_1 = 2I_2$ in layer two and $I_G+I_1 = 2I_1$ in layer one. It is immediately obvious that $I_1>I_2$ and that the longwave emission to space ($=I_2$) is half the longwave emission to the ground (I_1). The two atmospheric layers differ because the top layer receives longwave radiant energy from below but not from above while the bottom layer receives longwave radiant energy both from above and below. The atmosphere is not black but a similar argument follows. Generally, more radiant energy is entering the layer below than the layer above for atmospheric values of shortwave and longwave absorptivities. Since the atmosphere has less irradiance from the upper than the lower layer, the temperature must be least in the upper layer and greater in the lower layer. Using the irradiances above, then T_2 =237.5 K, T_1 =268.7 K, and T_G =290 K.

Later in this Chapter a radiative equilibrium model is introduced to initiate discussion of how the temperature profile of the atmosphere is created. In essence, that model uses an infinite number of 'glass' layers (no motions present), each one in radiative equilibrium (so there is no net gain or loss of radiant energy at any layer), and surface fluxes are not allowed. One major difference is that model ignores atmospheric solar absorption. The result is a temperature profile that decreases monotonically with increasing height.

3.1.4 Zonal Average Radiative Properties

The discussion above concentrates upon the global and annual average radiative properties of the atmosphere. In chapter 1, figure 1.2b shows annual average shortwave and longwave radiation measured at the top of the atmosphere (TOA). The annual average amount of solar radiation reaching the top of the atmosphere, when averaged over the entire surface of the earth, equals the total (341 W/m^2) in Figure 3.3. The actual amount of radiation absorbed by the earth, atmosphere, and ocean is given by the short-dashed line in Figure 1.2b. The absorbed radiation corresponds to the 70% absorbed by clear air, clouds, and the earth's surface shown in Figure 3.3. The solid line in Figure 1.2b shows the latitudinal distribution of the longwave emission to space. The integrated amount of the longwave emission must balance the absorbed, so the annual and global average amount is again 70% of the incident solar radiation used previously (now on the right side of figure 3.3).

The glass slab model creates a context for understanding these radiative values at the Earth's surface.

Figure 3.6 shows several shortwave radiative components during the extreme seasons and for an annual average. Incoming irradiance reaching the TOA is shown. The amount of solar radiation reaching the Earth's orbit differs between seasons. The Earth's orbit is closest to the

Sun in early January and furthest in early July with about a ±3% difference at perihelion and aphelion from the annual mean. So ~5% more solar radiation reaches the Earth's orbit in December-February (DJF, figure 3.6b) than in June-August (JJA, figure 3.6c). The solar radiation reaching the TOA (figure 3.6a) on the annual average is greater in the tropics than in the polar regions by a factor of two. At the TOA there is a relative maximum near each pole during local summer. At the summer solstice, the accumulated solar radiation falling on the surface of the pole (for clear sky conditions) exceeds that at all other latitudes because of the geometry of the Earth's tilt relative to its orbit. Even though the sun has a low angle, by being above the horizon most or all of the day, the accumulated solar radiation becomes largest. So during these extreme seasons there is a relative maximum near the summer pole with a general trend in solar radiation reaching the surface from a maximum at the summer hemisphere subtropics to near zero at the winter pole.

Figure 3.6 depicts corresponding solar irradiance absorbed in data from NDRA2 reanalyses over 1979-2014. NDRA2 reanalysis values differ by ±5% from comparable quantities from ERA-40. Differences between these two reanalyses tend to be larger at polar and tropical latitudes; further details are discussed in Grotjahn (2008). The absorption by the Earth's surface, by the atmosphere, and the total by both as measured at the top of the atmosphere are all shown. The amount absorbed has even more pronounced variation than the amount reaching the TOA: on an annual average it differs between tropics and poles by a factor closer to five. A factor of three difference in absorption is found between the summer subtropics and summer polar regions. The total shortwave (sw) values absorbed peak at latitudes around 15-20 degrees. In the summer hemisphere the peak is at higher latitude (30-35 degrees). Since the sw_s curve is the amount of radiation absorbed at the Earth's surface, the space between the I_sol and sw_s lines shows the amount of radiation that has been scattered, reflected, and absorbed by the atmosphere at each latitude. Even though the annual average sw reaching the TOA is largest at the equator, higher amounts are absorbed (sw_t) to the north and south due to persistent cloudiness associated with the intertropical convergence zone (ICZ). The amount of solar radiation absorbed by the atmosphere (sw_a) is smaller than for the surface (sw_s) except in polar regions. Hence, the absorbed sw at the surface largely mirrors the total absorption distribution away from the poles. Surface values of absorbed sw are low over polar regions during local summer since the icy-white surface is so highly reflective to visible light. Hence, the sw absorbed by the atmosphere also has less variation with latitude than does surface absorption. Indeed, sw_a is remarkably flat over the latitudes of each summer hemisphere. Interestingly, atmospheric absorption peaks at the latitude (~5N) where there is a minimum in total and surface absorption. These data imply that the atmospheric absorption is large near the equator even though it is shaded by relatively more

cloudiness. In midlatitudes, relative minima in the solar radiation reaching the surface result from relatively greater cloudiness associated with the midlatitude storm tracks. One might think of clouds as excellent at reflecting sw, but these results show that clouds are also more effective at absorbing sw than is clear air. To reinforce the point, the incoming solar (I_sol) and surface absorbed (sw_s) are largest in the subtropical summer, but the atmospheric absorption is a relative minimum in the NH summer subtropics.

The ratio of the total absorbed divided by the total incoming is called the (TOA) planetary albedo. Albedo differs from reflectance in that it is the fraction of the total amount of radiation that is reflected summed over all wavelengths of light whereas reflectance applies to a specified wavelength. Albedo has import to the general circulation in several ways (Stephens et al., 2015, describe a half dozen). For example, energy balance climate models (discussed below) are highly sensitive to planetary albedo values. Albedo participates in several general circulation feedbacks, such as cloud-albedo feedbacks: from clouds that may be negative (increased cloud water content with warming, Sommerville and Remer, 1984) or positive (reduced low cloud with warming, Clement et al., 2009). Another feedback loop, proposed by Lian and Cess (1977), is that an increase in radiation has a positive planetary albedo feedback (albedo reduction). Qu and Hall (2006) show that the snow-albedo feedback in areas with seasonal snow cover is the primary factor in that planetary albedo loop. The snow ice albedo feedback has two paths: cloud cover attenuating surface albedo changes (such as more clouds where there is less snow) and change of surface albedo with temperature (e.g. Qu and Hall, 2007).

The zonal-average albedo is shown in figure 3.7 in the annual average and for the two extreme seasons. Two estimates of albedo at the TOA are shown along with the NDRA2 estimate for the surface. Global averages of the TOA quantities correspond to the '30%' of SW radiation reflected in figure 3.3. The remaining '70%' corresponds to an area-weighted average of the solid curve in figure 3.6a and also the I_{IN} (~239Wm^{-2}) used by the glass slab models. Areas that are primarily ocean-covered have low reflectance (except at a small angle of incidence) as do forested land areas, while snow-covered and desert areas are highly reflective. The TOA values are zero or near zero for polar latitudes during local winter because the sun hardly rises above the horizon, if at all. (Albedo is not calculated when there is no sw.) Since the TOA albedo is around 25-40% at these latitudes where surface albedo is near 10-15% it is clear that the atmospheric contribution dominates the total albedo. Donohoe and Battisti (2011) estimate that 88% of the global average albedo is due to the atmosphere. They also estimate the atmosphere contribution by hemisphere to be 90% for the SH and 86% for the NH owing largely to the greater desert areas of the NH.

The two albedo estimates have differences up to ~10%. The ERBE satellite data tend to be lower than the NDRA2 values in the tropics but higher in middle latitudes. The ERBE data, when globally averaged, are closer to the 30% used in global energy balances (figure 3.3) and the glass slab model. Other general properties are similar: relative peak in the TOA albedo near 5N but no such peak in the surface albedos (which are a factor of three lower). Hence the albedo and the near-equator dip in sw radiation are consistent with reflection by persistent ICZ cloudiness. Cloud cover data shown later will confirm this atmospheric contribution to the albedo. Similarly, the greater ocean fraction (fig. 1.2) in the SH leads to lower midlatitude albedos compared to corresponding NH latitudes. The ERBE estimate of total albedo tends to increase monotonically towards each pole. On the hemispheric trend is a smaller, opposite trend driven by the relative maximum near 5N with minima in each subtropics. Total (TOA) albedo is 25-30% in the tropics, climbing to 35-45% in midlatitudes with 60-70% in the polar regions. The global average of the surface albedo in figure 3.7a is comparable to the 13% estimated from the global balance (7/54 in figure 3.3).

Seasonal changes in middle to high latitude snow cover and sea ice are apparent in the NH when comparing figures 3.7b,c. The tropical peak in albedo is larger in JJA than DJF. In midlatitudes, NDRA2 and ERBE albedos tend to agree better in winter than summer.

Figure 3.8 summarizes zonal mean radiative energy balance. The curves of I_sol and sw_t are repeated using a stretched coordinate in latitude. The other curves are total longwave (lw) emission from the Earth (lw_t) and the difference sw_t minus lw_t, known as the net radiation (nr_t). The horizontal global average of lw_t in figure 3.8a is the '70%' net annual emission to space in figure 3.3 as well as sum { $a_{LA}I_A + (1-a_{LA})I_G$ } in the glass slab model. That global average is the annual average '70 units' used above. Visualizing this global average is facilitated by the stretched coordinate, where latitude spacing on the diagram is proportional to cosine of latitude, and thus proportional to the surface area in each latitude band. To reinforce the point, in the absence of a trend over time, the annual and global average net radiation should be zero. In figure 3.8a, the nr_t curve has positive area cancelled by the negative areas. These TOA data are from ERBE instead of the NDRA2 data shown in figure 1.1a as the NDRA2 net radiation data do not sum to zero.

As mentioned in Chapter 1, the net radiation is zero near latitude 38 on an annual average. Absorption exceeds emission for lower latitudes, the opposite for higher latitudes; to sustain this circumstance there must be heat transport from lower to higher latitudes that becomes a relative maximum where net radiation is zero. It is clear from figure 3.8 that there is a net transport from the summer to the winter hemisphere. One might think the negative net radiation (nr_t < 0) is cooling the winter hemisphere and the positive nr_t warming the summer

hemisphere. But, the change in temperature between the start and the end of the seasons plotted, is pretty small, so there is not much net heating or cooling. (Those changes happen in the transition seasons: September-November and March-May.) Since the temperatures are little changed, there must be strong heat transport between the hemispheres. Such required heat transport drives the general circulation as noted in Chapter 1. Considering the conceptual model developed in Chapter 1, it is immediately clear that in the tropics, the interhemispheric transport requires the *winter* hemisphere Hadley cell to expand across the equator and to be stronger than the summer Hadley cell.

The seasonal values show positive net radiation in each summer hemisphere (except near the poles) and negative net radiation in each winter hemisphere (except near the equator). The emission in the winter high latitudes is so strong that it exceeds the incoming solar at the TOA. (lw_t exceeds I_sol for latitudes greater than ~ 30S and 38N.) There is large poleward heat transport in each winter hemisphere which is maximum at a tropical latitude (~10S and 15N) in the respective winter hemisphere. Poleward heat transport for each summer hemisphere is comparatively small in the net with a maximum at a high latitude (~70 degrees).

Also noted before, the lw curves are much flatter than the incoming sw curves, implying the temperature gradient with latitude is less than would be the case for local radiative equilibrium. Longwave emission is proportional to the temperature of the emitter. Figure 3.8 shows lw_t peaking in subtropical latitudes and diminishing towards each pole. The lowest value is at the winter pole. The highest is near 12-15 degrees latitude of the summer hemisphere. The subtropical latitudes are where most deserts lie which are regions of subsidence and suppressed cloud cover.

Similar to the absorption curves shown in figure 3.6, the emission curves have dips near the equator that correspond with the tropical cloudiness, though the match between sw_t and lw_t curves is stronger during JJA. As noted in the discussion of terrestrial radiation, the atmosphere is much less transparent to lw than to sw for most infrared wavelengths. The glass slab model captures the property with $a_{LA} > a_{SA}$. There are atmospheric 'windows' as shown in figure 3.2 for clear skies. Except for thin clouds, clouds are excellent absorbers of longwave radiation and so regions with sufficiently thick clouds will have emission prominently from the tops of the clouds instead of prominently from the Earth's surface. The glass two-slab model can illustrate the effect. If the additional cloudiness was confined to layer 1 in figure 3.5b, the emission to space would have a reduced I_G term since a_{L1} would increase. Of course that greater cloudiness would reflect more solar radiation and thus increase the global albedo value. Longwave emission to space would become less due to less solar absorption. The air temperature

in layer 1 as well as the surface temperature both decrease to reduce the net emission to space. The opposite line of arguments applies to less cloudy regions.

Figure 3.9 shows at the surface that: the longwave emission downward exceeds the solar radiation at many latitudes. At many latitudes the upward lw from the surface exceeds the net solar radiation absorbed, sw_t. This is illustrative of the 'greenhouse effect' shown in the glass slab model, especially the two slab model. As noted in figure 3.3, the downward radiation from the atmosphere at the surface is quite large, amounting on an annual average to ~330 Wm^{-2}. To the extent that global averages of these seasonal averages match the annual global average, one can see that global averages of the lw curves in figures 3.9a,b result in approximately the same radiant flux.

General summary comments about the zonal average radiation budget are:

- *Solar radiation*. The solar radiation reaching the top of the atmosphere varies sharply with latitude (by more than a factor of 2). Thirty percent is reflected back to space though polar regions and the cloudy storm tracks and ICZ have higher reflectance. The remainder is absorbed: ~2/3 by the surface and ~1/3 by the atmosphere, including cloudy regions. However, atmospheric absorption exceeds surface absorption at polar (>75 degrees) latitudes. Annual average absorption varies by a factor of 5 from tropics to poles.
- *Albedo.* The fraction of incoming sw radiation reflected (over all wavelengths) is the abedo. With a peak due to atmospheric cloudiness near ~5N, values generally increase from 10 to 90 degrees latitude. Surface values are much lower ~5-15% than atmospheric values (~30-40%) for latitudes less than ~60 degrees. Obviously, polar regions have extensive areas of highly-reflective ice and snow surfaces. However, the cloudiness during summer is very high in the polar regions, too. The high reflectance during summer (when the incoming radiation is large), coupled with little or no radiation during winter, gives the curious result that the amount of *annual* average reflected radiation is nearly constant with latitude. Desert areas tend to be highly reflective and have less cloudiness so the surface contribution to total albedo is more in the NH than SH. However, ~9/10 of the planetary albedo comes from the atmosphere.
- *Terrestrial radiation*. The terrestrial emission has much less variation with latitude than the absorption (a factor of ~1/3 between tropics and poles). As a consequence, most of the atmosphere is not in local radiative balance. In figure 1.2b, Near latitudes 38 N and 38 S, the atmosphere is in local radiative balance.
- *Net radiation* On an annual average, the solar (sw) radiation absorbed exceeds the terrestrial (lw) radiation being emitted resulting in positive net radiation between 38 N and 38 S. For the higher latitudes, emission exceeds absorption, yielding negative net radiation. Almost the

entire summer hemisphere experiences positive net radiation while most of the winter hemisphere has negative net radiation.

- *Net energy balance*. Positive net radiation indicates radiant energy gain, while negative net radiation indicates energy loss. Areas of zonal average positive net radiation amount balance corresponding areas of negative net radiation. Over time, there must be transport of heat away from latitudes of positive to latitudes of negative net radiation to sustain radiative energy balance. Part of the excess is heating up the summer hemisphere while the deficit is cooling down the winter hemisphere. Part of the excess and deficit causes a transport of heat between hemispheres; such cross-equator flow is evidenced by the dominance of the winter hemisphere Hadley cell.
- *Hemispheric differences*. The differences between NH and SH radiative properties are relatively small compared with the seasonal variation. Radiative properties for the two hemispheres are roughly symmetric with three notable exceptions. (1) One asymmetry is centered near 5 N, where there is a pronounced dip in both the surface absorption and emission. This dip is caused by relative cloudiness of the ICZ. Over much of the globe, the ICZ is centered about five degrees north of the equator (more in Chapter 5). The high cloudiness of the ICZ causes sw absorption to dip at the surface and peak in the atmosphere. Along the ICZ some longwave emission is from the anvil tops of very deep thunderstorms where temperatures are very cold and hence longwave emission is less than from surrounding areas (where clouds are absent or lower). (2) net radiation is generally greater in SH tropical and middle latitudes (equator to 60 degrees) than corresponding NH latitudes. The cause is mainly greater sw absorption. (3) Albedo has greater seasonal change in the NH due to the greater land fraction. Generally higher values occur for subtropical (deserts) and middle latitudes (winter snow cover plus deciduous plants leaf loss) though the atmosphere dominates the total albedo, the NH has 40% larger surface contribution to the total albedo than does the SH.

3.1.5 Zonally-varying Radiative Properties

Albedo has complex longitudinal variation dictated partly by different land surfaces and partly by cloud patterns. Figure 3.10 shows annual average albedos parsed into atmospheric and surface contributions to the planetary albedo. Consistent with figure 3.7, the atmospheric contribution is larger both because clouds are so highly reflective and because less radiation reaches the Earth's surface than the TOA. Beginning with the surface albedo (figure 3.10a) desert areas (like the Sahara) have 35-50% albedos but only contribute about 20% (figure 3.10b) to the total planetary albedo (figure 3.10c) of 35-45%. (Percentage contributions shown here are

additive, hence over the Australian interior: the ~10% surface contribution, figure 3.10b, plus the ~20% atmospheric contribution, figure 3.10d, add up to the ~30% planetary albedo.) Polar sea ice has surface values of 60-70% but contribute only 15-20% to the planetary total. Greenland and Antarctica have surface values >70% resulting in 25-30% of the planetary total. Most of the midlatitude and tropical land masses have 20-30% surface albedos that contribute <10% of the total planetary value. The ocean surface (where ice-free) has ~10% as mentioned above. The atmospheric contribution (figure 3.10d) is high (35-45%) across the midlatitude oceans, with notably less over land masses; clouds associated with frontal cyclone storm tracks are the primary cause. Even in the polar regions, the atmospheric contribution is large (35-55%) of the total (55-80%). The atmospheric contribution is least over the subtropical oceans where the planetary albedo is also least. The atmospheric contribution on the east side of each subtropical ocean is a little higher due to persistent low cloudiness shown later. The ICZ has been mentioned above and is visible as a band of higher atmospheric albedo most easily seen between the subtropical oceanic minima. Somewhat surprisingly, the atmospheric contribution over major deserts (Sahara, South Africa, and Australia) is comparable to the surface contribution.

The zonal and annual average radiative balance components at the top of the atmosphere are shown above in figure 3.8a; the horizontal pattern is shown in figure 3.11.

The solar radiation that is not reflected is absorbed. Figure 3.11a shows the rate of sw absorption averaged over a year. The absorption decreases rapidly toward the poles as one expects from the zonal mean absorption pattern (figure 3.8a). The absorption pattern is rather similar to the albedo distribution (figure 3.10c) with one main exception. The incoming solar radiation has a strong dependence upon latitude, so the absorbed radiation strongly decreases towards higher latitudes. The higher values of absorbed radiation are over the tropical and sub-tropical oceans, except where the ICZ causes higher albedos.

The contours are strongly oriented zonally (roughly constant latitude) outside the tropics. This zonal symmetry validates the use of zonal average depictions as a first approximation to the general circulation parameters. Strongly zonal contours cross the mid latitude continental regions. Zonal-orientation is disrupted by 1) tropical land masses, 2) major ice sheets (primarily Greenland), and 3) subtropical deserts. The tropical land masses have generally higher albedo, mainly from increased cloudiness as noted in figure 3.10d, than adjacent ocean. Similarly, ice-covered and cloudy Greenland has higher albedo and less sw absorption than adjacent ocean. Desert regions that have a highly reflective surface also have reduced sw absorption.

For energy balance there must be longwave radiation back to space to match the sw absorption. The annual average rate of lw radiation is shown in Figure 3.11b. The lw reaching the TOA is emitted from atmospheric layers, the surface of the earth (if the sky is clear or clouds

are thin), and from the top of a cloud. The Stefan-Boltzmann law (Appendix D) states that the irradiance is proportional to the temperature of the emitter raised to the fourth power. The stippled areas in figure 3.11b have emission from warm temperatures of the Earth's surface and lower atmosphere. A thick cloud is opaque to lw radiation, so the lw emission is mainly from the cloud top with little from below. For deep convective clouds, the cloud top is very high, very cold, and therefore emits comparatively little lw radiation. The regions of deep tropical convection show up as lw values <240 W/m^2. The lower tropical values are over the continents of South America and Africa with the lowest values over Indonesia indicative of frequent, very tall thunderstorms. The stratiform clouds to the west of subtropical: Africa and North and South America have tops that are quite low (below 800 hPa), so the cloud tops are relatively warm, and the lw emission is moderately high. Ice-covered areas such as Greenland and Antarctica are very cold at the surface and so have very low values of longwave emission. In general, the gradient of the longwave emission is much less than that for the solar absorption as expected from figures such as 3.8a. The differences between the magnitudes of emission and absorption locally imply zonal as well as meridional heat transports.

Subtracting the outgoing lw radiation (Figure 3.11b) from the absorbed sw radiation (Figure 3.11a) obtains the TOA local net radiation shown in figure 3.11c. Areas with positive values absorb more radiant energy than they emit. Areas with negative values (dashed contours) denote regions where the outgoing radiation exceeds the absorbed radiation. Zonal average figures shown earlier have negative values poleward of ~38 degrees latitude with positive values between ~38N and ~38S. Figure 3.11c is consistent since, as with the other panels in this figure, the contours have a strong zonal component in middle and high latitudes as well as parts of the subtropics and tropics. Exceptions to zonal orientation of net radiation contours occur a) over deserts, b) in the eastern subtropical oceans, c) for Greenland, d) tropical land areas, and e) for some higher elevations. The first four region types have higher albedos than the global average which can partly explain these regions having less net radiation (including more strongly negative values) than other regions at the same latitude. Deserts are discussed in the next paragraph. The subtropical eastern oceans have persistent fog and low level stratiform clouds so the emission from cloud tops is relatively warm, but the clouds are highly reflective to sw radiation. For example, south of Peru, the net radiation is negative at 20-30S. Greenland has slightly less (more negative) net radiation than other longitudes because the reflective reduction of sw is a stronger effect than the colder emission temperatures. There are also longitudes of higher net radiation along latitude lines. Over land, some higher elevation regions tend to have a bit larger net radiation than adjacent lowlands since those regions are colder (lower lw) but dark enough to have similar sw absorption; examples seen in figure 3.11c are the Andes and the

Tibetan Plateau. Finally, areas of deep convection are enhanced over parts of tropical land masses; those locations have a larger reduction in lw from very cold cloud tops than from reduced sw by reflection. A curious example is the remarkable coincidence that a contour value matches well the coast of Borneo (with values nr_t <80 W/m^2 over the island).

The Sahara, Arabian, and Australian Deserts are relative minima in absorbed sw despite having much hotter surface temperatures than adjacent ocean at the same latitude. These regions have hot surface temperatures coupled with relatively few clouds (as judged from figures 3.10a,d) so that the lw reaching the TOA is large. Indeed the lw emitted exceeds the sw absorbed making these deserts have areas of negative net radiation. It may at first be surprising that such hot regions lose more radiant energy to space than gain by absorbing sunlight. To sustain that excess emission there must be transport of heat into the region. The heat transport cannot be solely horizontal, since these deserts are surrounded by cooler regions. Hence there must be a combination of horizontal and vertical advection of heat with sinking required so adiabatic compression can convert high potential temperatures into high sensible temperatures. Such sinking, of course, is consistent with the suppressed cloudiness. The primary source of the high potential temperature will be tropical precipitation, discussed in detail later. The complete description of the circulation that transports the heat is discussed later, but for now can be approximated by the notion of a locally enhanced Hadley cell type of circulation.

Changes in the primary radiative balance components between the extreme seasons can be seen in figure 3.12. Similar to the annual averages of figure 3.11, many contours have a strong zonal orientation. The zonal orientation extends more deeply into the winter stubtropics than the annual average. Correspondingly, the deviations from zonal contours are more apparent during summer. This is not surprising since the meridional gradient (as seen in figure 3.8) is stronger in winter and weaker in summer than the annual average. The stronger gradient masks the longitudinal variations, and *vice versa*. Hence, the larger values of sw absorption occur in the subtropical central oceans of the summer hemisphere. Notable in the sw absorbed is the large minimum over Southeast Asia during JJA (minimum values <260 W/m^2) due to extensive, persistent cloud cover from the Asian Monsoon that is not apparent in DJF. Those Asian summer monsoon clouds create a relative minimum in lw emission seen in figure 3.12e and lower values (<60 W/m^2) net radiation. The Sahara and Arabian deserts are hotter during summer and have larger lw emission, but the sw radiation absorption is even greater, so the net radiation is more strongly negative during winter than during summer. Seasonal changes of tropical convection location and magnitude are most easily inferred from the lw emission. For example the areas of minimum lw over Africa and South America migrate northward from DJF to JJA. There is a similar migration from Indonesia and the island of New Guinea towards Southeast Asia. This lw

minimum shift also occurs for the Indian Ocean ICZ, but not for the Atlantic and eastern Pacific ICZ. Seasonal change of net radiation over Polar regions is one of magnitude, as net radiation remains negative all year.

A key question in climate studies emerges from the discussion above: what is the net effect of clouds upon radiative balance? The high albedo of clouds reflects incoming solar radiation; increasing cloudiness would cool the earth by this effect. However, clouds are very efficient at absorbing infrared radiation emitted by the earth's surface; increasing cloudiness would warm the earth by inhibiting radiative cooling of the surface. Which effect dominates? Measurements from the Earth Radiation Budget Experiment (ERBE) confirm that, on average, cooling by the albedo change has greater effect (e.g., Ohring, 1990). ERBE measurements show, on average, a 14 W/m^2 net loss of radiation due to clouds. A review by Arking (1991) places the net loss between 17 and 27 W/m^2. Harrison et al. (1990) find smaller values of net cooling (14 to 21 W/m^2 on the annual average); they find near cancellation of the two effects in winter, so that the summer cloud cooling is quite strong. Clouds are thus reducing the seasonal change in net radiative heating.

The radiation budget presented above emphasizes the time averaged properties, yet it also has complex natural variability. Natural variability can include periodic and quasi-periodic climate modes such as ENSO and the PDO as well as external forcing events (like major volcanic eruptions). Natural variability can also include more 'random' aspects like the variation from one frontal cyclone to another. An illustration of how natural variability can be complex has been uncovered in tropical radiative balance. Chen et al. (2002) discovered a 5 W/m^2 increase in lw_t and a 2 W/m^2 decrease in sw radiation reflected to space at the TOA over 30S to 30N from 1985 to 2000. They attributed the trend to changes in tropical large scale circulations. Specifically, the changes in cloudiness (Wielicki et al., 2002) as reduced deep clouds decrease sw reflection and allow greater lw emission from lower elevations than would occur from the tops of deep clouds. These changes occur even when large volcanic eruptions and ENSO phase effects are removed. Hartmann (2002) noted that this change in radiative balance occurred in the absence of notable surface temperature changes and thus absent an obvious boundary forcing.

The figures 3.11-3.12 present the complicated result of a general circulation that tries to even out the distribution of incoming solar (I_sol in figure 3.6) in the presence of clouds and different surface types having complex reflective (figure 3.10) and radiative properties. In going from figure 3.6 to figures 3.11-3.12, the atmosphere must also be transporting heat in complex ways.

3.2 Heating and Heat Transport

3.2.1 Surface Heat Fluxes

The atmosphere's energy budget (figure 3.3) has non-radiative exchanges between the atmosphere and the Earth's surface. Solar energy heats the Earth's surface which conducts heat into the atmosphere that is carried away from the surface by turbulent eddies. Solar energy reaching the surface could also evaporate water; the vapor might also be carried away by turbulent eddies. The former is surface sensible heat flux (SSHF) and the latter is surface latent heat flux (SLHF). Both are positive when heat is gained by the atmosphere.

The SSHF can be approximated adequately for our purposes here with the bulk aerodynamic formula:

$$SSHF = C_{Ht} |V| \{ T_G - T_{sfc} \} \tag{3.14}$$

Equation (3.14) is a parameterization of the SSHF in a simple formula that illustrates the proportionality to the air (T_{sfc}) temperature difference with the Earth's surface (T_G). The larger the surface-air temperature difference, the larger the heat flux; when the surface is warmer than the air SSHF is positive. |V| is the wind speed at the height the temperature is measured, and C_{Ht} is the bulk transfer coefficient for heat.

A similar bulk aerodynamic formula can represent the SLHF:

$$SLHF = \left(\frac{L}{C_P} \right) C_{Ev} |V| \{ f_q \, q_{sat}(T_G) - q_{sfc} \} \tag{3.15}$$

In (3.15) the bulk aerodynamic coefficient for evaporation, C_{Ev}, is similar in size to C_{Ht}. $q_{sat}(T_G)$ is the specific humidity if air was saturated at the temperature of the Earth's surface. The specific humidity of the air at instrument height is q_{sfc} . The larger the difference between the moisture content of the air and the moisture content the air would have if saturated at the temperature of the Earth's surface, the larger SLHF. However, $q_{sat}(T_G)$ is a not a linear function of temperature. When the q_{sfc} is less than $q_{sat}(T_G)$, SLHF is positive. The factor out front (L/C_P) is the inverse of the psychometric constant, needed in part to make the units from the difference in mass ratio of water to air match the units W/m^2. An important difference from (3.14) is that the SLHF formula assumes the surface can provide water as needed for evaporation; that assumption is valid over ice-free ocean areas (which cover most of the Earth, figure 1.2). Over land areas, the available moisture is less, but complicated since the surface soil can dry out, limiting SLHF but plants can draw moisture from their roots and transpire it from their leaves, effectively boosting SLHF. The factor f_q is to acknowledge that the water available to be evaporated from the surface may be limited; hence, f_q =1.0 for the ocean, but near zero for dry land.

SSHF (figure 3.13a.b) is positive over tropical oceans and most of the middle latitudes of the winter hemisphere. SSHF over ocean is larger where horizontal temperature gradients are larger; specifically, near the western boundary currents (WBCs) and sea ice margins in winter. SSHF is negative over most of the Arctic. Over North America and Eurasia in DJF, SSHF is negative. In contrast, during JJA, the Northern Hemisphere continents have positive SSHF. Variations between reanalyses cause [SSHF] (figure 3.14a) to be systematically larger in ERA-40 compared with NDRA2 data. The differences in [SSHF] between datasets tend to increase towards higher latitudes, exceeding 10 W/m^2 in polar regions. The global mean of SSHF in DJF is 6.06 in NDRa2 and 14.00 in ERA-40; in JJA the global means are 10.05 and 16.99, respectively.

SLHF (figure 3.13c,d) is larger in global energy budgets and has similarities and differences with SSHF in geographic distribution. As with SSHF, larger values are found near the WBCs. In chapter 1, the wind driven ocean model circulation (figure 1.6) transports warm water poleward along most continental east coasts even in winter. The westerly prevailing winds (e.g. the schematic circulation from the 'thought experiment' of figure 1.5d) blow off the cold winter continent and over the WBCs. One easily imagines how both surface fluxes can be large when cold and dry continental air masses blow over the warm waters of WBCs to generate large temperature and moisture differences. Unlike [SSHF], [SLHF] (figure 3.14b) is positive for all latitudes. SLHF tends to be positive definite (figure 3.13c,d) because the water mass cycle returns most of the water to the Earth's surface as precipitation (P_w) and not as dew or rime. P_w is not part of the SLHF formula and handled separately in an energy budget in terms of latent heat release within the atmosphere where the precipitation forms. Alternatively, one can say that evaporation (atmosphere gains latent heat from the surface) greatly exceeds riming and dew formation (atmosphere releases latent heat to the surface). [SLHF] is much larger than [SSHF] at most latitudes (the polar regions have larger, negative [SSHF]). [SLHF] has relative maxima in the subtropics. Evaporation is large over the subtropical oceans as might be deduced from skies being clear (as noted in the albedo, figures 3.7 and 3.10, except in the eastern oceans) and radiation reaching the surface is seasonally large (figure 3.6). These two subtropical maxima are similar in DJF; in JJA the Southern Hemisphere max is about 25% larger. The fluxes generally decrease towards the poles, with a weak secondary maximum at high northern latitudes.

The [SLHF] is systematically less in ERA-40 than NDRA2 data for most latitudes north of 30S. The two reanalyses differ in [SLHF] by 5-20 W/m^2 at many latitudes. This large difference motivates the comparison made here. The corresponding [SSHF] difference has opposite sign in these latitudes. The two datasets have quite similar [SLHF] in latitudes south of 30S. The global mean of SLHF in DJF is 88.86 in NDRa2 and 81.55 in ERA-40; in JJA the

global means are 93.27 and 84.91 W m^{-2}, respectively. Geographically, NDRa2 data is larger than ERA-40 data over nearly all of the tropics, both ocean and continental areas. The difference is largest where the field is larger, such as the non-ICZ portion of the tropical Atlantic (during JJA: 5N to 20N and 10S to 15S where differences exceed 40 W m^{-2}). The two reanalyses partition SSHF and SLHF differently: ERA-40 favors SSHF while NDRA2 favors SLHF; the sum of these two surface fluxes globally is more similar than the individual parts. (ERA-40 is plotted here for simplicity; comparison plots with NDRA2 are found in Grotjahn, 2008).

3.2.2 Horizontal Heat Fluxes

As noted in the discussion of net radiation, there must be horizontal heat transport so that the high latitudes can emit more radiation than they absorb and the low latitudes emit less than they absorb. Heat is transported by both the atmosphere and the ocean. For the atmosphere, surface fluxes inject surface absorbed radiant energy into the atmosphere in sensible and latent energy forms.

One might estimate the heat transport by starting with the satellite measurements of the TOA radiant energy budget. For stationary conditions (no net gain or loss of energy, such as might be assumed on an annual average) then the atmosphere must export energy if the input does not match the output of energy. Input can be the net flux of energy from the surface while the output can be the TOA net downward radiation. Hence the divergence of the vertical, zonal, and time mean atmospheric energy flux is

$$\nabla \bullet \widetilde{\overline{[AEF]}} = \widetilde{\overline{[SLHF]}} + \widetilde{\overline{[SSHF]}} + \widetilde{\overline{[nr\_t]}} \qquad (3.16)$$

Where the curly overbar, straight overbar, and brackets notation are pressure, time, and zonal averages defined in Appendix A. Eqn (3.16) may be integrated over latitude intervals (weighted by the surface area around each latitude band), starting at the South Pole (where AEF is zero by definition) heading northward. Negative values indicate southward transport. A similar procedure applies to the ocean heat transports. The estimated heat transports required for radiative balance are presented in figure 3.15.

The atmosphere transports energy in kinetic and moist static energy forms, of which the MSE transport dominates. Subdividing the MSE transport reveals an important property of tropical mean meridional circulations. Hence:

$$\widetilde{\overline{[AEF]}} \simeq \frac{2\pi r \cos(\varphi)}{g} \int_0^{p_{sfc}} \overline{[v(C_p T + \Phi + Lq)]}\, dp \qquad (3.17)$$

Sensible heat transport includes advection of warm tropical air to higher latitudes as well as equatorward flow of cold polar air. Much heat is transported in latent form. The latent heat of water vapor is released when the water vapor condenses or freezes.

The following general comments can be made about the heat transports shown in Figure 3.15.

- *Uncertainty*. Lighter shading in figure 3.15a illustrates the uncertainty in the estimates. Wunsch (2005) shows that ocean transport is even more uncertain than indicated.
- *Net heat transport*. The total energy transport (solid line in Figure 3.15a) has maxima between 35 to 40° latitude in each hemisphere. The maxima occur there since that is where the net radiation curves (Figure 3.8a) cross zero. For latitudes lower than about 38° there is an excess of net radiation, implying that heat must be removed from each of those tropical latitudes. As one integrates the heat flux proceeding poleward from the equator, more and more heat must be transported until one reaches the latitude where there is a deficit of net radiation. At those higher latitudes more and more of the transported heat is used to counter the deficit in net radiation. Hence, the maximum heat transport occurs at the latitudes where the net radiation crosses from positive to negative values. Figure 3.15a is therefore consistent with the zero crossings found in Figure 3.8a.
- *Sensible heat transport*. The largest of the three contributions is the sensible heat transport by the atmosphere (labelled DSE). Sensible heat transport is monotonically poleward in both hemispheres on this annual average. It has a broad maximum from about 15° to 60° latitude in both hemispheres.
- *Latent heat transport*. The latent heat transport in the atmosphere has a mixture of poleward and equatorward transport. Latent heat transport in midlatitudes is poleward, but in the equatorial zones the transport is clearly *equatorward*. Equatorward latent heat flux (LHF) is most easily understood from a Hadley cell circulation. Low-level air gains moisture as trade winds blow equatorward over the ocean. In general, a layer of moist, well-mixed air exists between the surface and the trade wind inversion (at 1 to 2 km elevation); the trade wind inversion deepens as air moves equatorward. (Successive development of cumulus clouds deepens the moist layer. The clouds pump moisture from below to above the inversion.) The air flowing towards the intertropical convergence zone becomes more and more moist; eventually rising near the ICZ and most water precipitates out, releasing latent heat. The higher elevation poleward-moving air has much less moisture. Since specific humidity, q, is not negative and q is large only in the lower troposphere and little LHF. Thus, the low-level flow dictates the vertically-integrated LHF. The poleward LHF in midlatitudes will be shown later to be concentrated

in oceanic storm tracks where moist subtropical air is carried poleward in the warm sector of frontal systems. However, the flow is shown schematically in figure 1.5d.

- *Oceanic heat transport*. The oceanic heat transport has a deceptively simple distribution in Figure 3.15a. The oceans transport heat poleward at nearly all latitudes in this figure. The zero crossing for zonal and vertical average oceanic transport is close to the equator. The zonal averaging across all longitudes ('full zonal mean') hides transport that is complex within and very different between individual ocean basins. The full zonal mean averages various circulations, such as WBCs and the THC, some of which transport heat equatorward (Zheng and Giese, 2009; Marshall and Speer, 2012; Talley, 2013). Oceanic heat flux (OHF), defined as:

$$\left\{\widehat{OHF}\right\} = C_p \int_{-zbot}^{0} \int_{\lambda_W}^{\lambda_E} \rho v \left(T - 273\right) \cos(\varphi)\, d\lambda\, dz \qquad (3.18)$$

  is estimated in Figure 3.16. It is immediately clear that poleward flux in the SH is from a large southward flux in the Indian Ocean that exceeds the sum of *northward* fluxes in the southern Atlantic and Pacific. Figure 1.9 assists with explaining the pattern shown in Figure 3.16. A large fraction of the Indian Ocean southward OEF is injected from the western Pacific through the islands of Indonesia. The strong northward flux across the Atlantic is primarily from the global THC which has northward moving warmer surface water above southward moving colder deep water. In the southern Pacific the circulation has counter-rotating cells above each other, with the upper one transporting warmer near-surface water northward and intermediate-deep water southward..

The atmospheric heat fluxes in Figure 3.15b have these differences between the hemispheres.

- *Latent heat flux.* Latent heat fluxes, both in midlatitudes and tropics, are larger in the Southern Hemisphere (SH). This distinction is especially true for the tropical regions. Much of the difference can be explained by the tropics and midlatitudes having much less land area in the SH than in the NH (Figure 1.2). As shown in Figure 3.13, SLHF is much larger over oceans and so latent heat is more readily available to SH low-level circulations. Secondly, the distribution of land can locally reverse the zonal and annual mean temperature gradient. During summer, hot land areas over South Asia are poleward of relatively cooler ocean and drive the summer Monsoon. Detailed discussion of the Monsoon is left for later; the relevant point is the circulation, primarily between the equator and South Asia, is in the opposite sense of the zonal mean Hadley cells. Low-level flow has a northward component across the northern Indian Ocean bringing

moisture northward. At most other longitudes, especially across the Pacific and Atlantic oceans, the low-level winds are more similar to a Hadley circulation.

- *Sensible heat flux*. The sensible heat flux across the *tropics* is greater in the SH than NH. A primary reason for this asymmetry is again the Asian summer monsoon. The moisture carried towards South Asia condenses to release an enormous amount of latent heat, thereby warming the middle and upper atmosphere above the continent. When this heated air is carried equatorward by the return flow, a net southward sensible heat flux results when vertically averaged over the longitudes of the summer Monsoon. In simpler terms, it is as if the SH Hadley cell extends further north at these longitudes than elsewhere.

The annual mean geographical distribution of total atmospheric energy and its primary components are shown in Figure 3.17. The total energy is plotted in Figures 3.17a-c, but since the kinetic energy part is much smaller than the MSE part, those panels are considered an approximation to the MSE. The DSE and LE parts of MSE are also shown. The total energy in each column is divided into contributions from the 'quasi-stationary' part of the flow, which includes inter-annual variability, plus the transient part of the flow which includes fluctuations with periods shorter than a month.

The annual mean MSE transport (Figure 3.17a) is primarily poleward out of the tropical western Pacific and Atlantic Oceans and most of this transport is stationary over time (Figure 3.17b). The quasi-stationary MSE transport is also notable where there are persistent long wave troughs (shown later) at the east coasts of Asia and North America. The transient contribution to the total transport occurs across the midlatitude oceanic storm tracks from the equatorward to the poleward side of the storm track. Notice that the transient heat fluxes are opposite to the stationary fluxes along much of the storm track. Transient fluxes converge where the stationary heat fluxes diverge on the poleward side of the storm track and *vice versa* on the equatorward side. The anti-correlation between MSE transient and stationary midlatitude fluxes reflects a 'handing off' of the poleward heat transport from a quasi-stationary circulation to the midlatitude baroclinic eddies (and back to the stationary part off east Asia).

The DSE shown in Figure 3.17d is a vertical and annual average. If one applies a zonal average but relaxes the vertical average, while restricting the time averaging to the extreme seasons, then a pattern like the meridional cross-sections of $[v\Theta]$ shown in Figure 3.18 results. One sees that the net poleward heat in the Figure 3.17d is a relatively small difference between opposing upper and lower troposphere heat fluxes. The static stability of the atmosphere causes the flux in the high-altitude part of the Hadley circulation to exceed the opposite flux in the lower tropospheric part of that circulation.

The annual mean DSE transport and divergence (Figure 3.17d-f) and LE transport (Figure 3.17g-i) illustrate the contrasting heat fluxes of the tropical quasi-stationary circulation. Over the tropical Indian and western Pacific oceans, the DSE has large positive divergence and strong poleward transport, somewhat consistent with the upper branch of a 'Hadley' circulation. Hadley is in quotes because the circulation is not strictly meridional, but also has comparable zonal transport. In contrast, the LE transport has the opposite sign in these regions, having convergence into the ICZ, reflecting the moisture transport being much greater in the lower troposphere than aloft, due to the scale height for moisture (~2km) being much less than the dry atmosphere scale height (~6-8km). The reversal between sensible and latent heat transport was noted in the zonal mean transports of Figure 3.15b.

Precipitation follows closely areas of low level moisture convergence which are notable in Figure 3.17g-i. One should expect that regions of LE convergence should be regions where there is stronger precipitation. The thought problem of Chapter 1 and the albedo discussion in this chapter suggest a tropical band of enhanced precipitation labelled the ICZ. The ICZ is seen to have a rich structure, being enhanced in certain regions (the Indian Ocean, western Pacific, and Amazonia and Central America. While the LE convergence traces a line across the Pacific, it is much less in the central Pacific. Also noteworthy is the quasi-stationary enhanced LE convergence over these tropical land areas: Southeast Asia and Amazonia. The former indicates the Southwest Asian monsoon. In higher latitudes moisture convergence on the downwind ends of the Pacific storm tracks are notable in both the stationary and transient patterns and seem clearly reflecting enhancement of precipitation as the air is driven upslope by the mountains of North and South America. In the midlatitude storm tracks the LE pattern is similar to the DSE pattern. Moisture is transported from the equatorward to the poleward side of each storm track. Unlike DSE, the stationary and transient parts of the LE work together more places than not over the oceans to transport moisture from the subtropics to higher latitudes, especially in the central and eastern oceans. Where the stationary portion of the South Pacific convergence zone (SPCZ) interacts with midlatitude storms the transient and stationary parts have opposite sign and the stationary part converges moisture that the baroclinic eddies then transport further poleward. More will be said about the SPCZ later, but it includes a tropical band and a 'diagonal' band from (~180, ~10S) to (~120W, ~30S).

Returning to Figure 3.18, the seasonal dominance of the winter Hadley circulation is apparent. Similarly, seasonal components of the precipitation can be seen in the annual averages of figure 3.17g-i. The Southeast Asia, Central American, and Chilean LE convergence maxima mainly occur during JJA. The Amazonian and Indian Ocean maxima, along with the Northern Hemisphere storm tracks (including the west coast of North America) largely occur during DJF.

3.2.3 Internal Diabatic Heating

Sections 3.1.4 and 3.1.5 described the distribution of radiative heating and cooling in the atmosphere. Section 3.2.1 described external heat input to the bottom of the atmosphere while Section 3.2.2 included horizontal heat transport as well as convergence of moisture which is related to precipitation. The atmosphere has internal sources of heating from radiative processes and from water changing phase. So, the sections above plus the thought problems of Chapter 1 provide useful background for discussing the distribution of diabatic heating within the atmosphere.

Diabatic heating processes can be grouped into five categories (Grotjahn, 2015b) Shortwave and longwave radiation, latent heating, surface sensible heat flux, and friction. Friction as a source of heat is negligible. The radiation can be combined to indicate a net radiation.

For much of the atmosphere emission of longwave emission exceeds the absorption of shortwave radiation as noted in figure 3.3 (for the atmosphere as a whole) and figure 3.6 (SW_a as a function of latitude and season) and at the surface from figure 3.9. The vertical and seasonal structure of the atmospheric net radiative cooling (NRC) is finally shown in Figure 3.19). NRC is the dominate diabatic process over much of the troposphere, with maxima at lower subtropical elevations (where temperatures are warmer and clouds are fewer) and in polar regions (where there is little solar radiation) in winter. NRC is clearly stronger in the winter hemisphere. In the stratosphere, absorption of solar radiation by ozone leads to net radiative heating (NRH) that is strongest in the tropics and summer hemisphere.

A prominent source of tropospheric heating is from latent heat release (LH). LH is strongest in the tropics. Since LH is linked to areas of precipitation, the deep ICZ is clearly visible. Midlatitude maxima of LH do not extend as high since NRC is stronger and the moisture available to change phase is small at higher altitudes in these time averages. In the summer hemisphere the NRC decreases and so there is net heating, labelled LH, extending to higher midlatitude elevations. The lower elevation heating maxima in winter midlatitudes may be mainly from LH. Part of the maximum in the JJA Northern Hemisphere subtropics is likely from the Asian summer monsoon. Part of the midlatitude maximum is from LH released in the baroclinic eddy storm tracks, though again, NRC partly cancels.

Many latitudes of DJF in the Northern Hemisphere have prominent heating at the surface. Higher latitudes have strong surface heating in the winter hemisphere. These may be due to surface sensible heat fluxes (SSHF) but the picture is not that simple. Surface sensible heat fluxes are already described in Section 3.2.1. SH in Figure 3.19, are, of course, maximum at the

surface, diminishing rapidly in the lowest 100 hPa. Figure 3.14 finds SSHF larger in midlatitudes during JJA in both hemispheres whereas Figure 3.13 reveals that fluxes over the western boundary currents are larger in winter, but the land (especially over deserts) has larger values in summer. In both seasons, Figure 3.13 shows a lot of cancellation between land and ocean areas around a middle and higher latitude circle. Thus, the areas labelled SH in Figure 3.19b are restricted to the subtropics.

3.3 Temperature

The radiation and heat transports are closely linked to the patterns of temperature. The first crude zonal average large scale temperature fields were published by von Humboldt in the first half of the 19th century (reproduced in Hildebrandsson and Teisserenc de Bort, 1907). Upper air observations were made from balloons or approximated from observations on mountains. According to Hartmann (1985), Teisserenc de Bort discovered and named the tropopause and stratosphere, publishing his balloon measurements in 1902.

Figure 3.20 shows the zonal mean temperature distributions for December through February and June through August. Five general features of the temperature field are seen in Figure 3.20. A) The change in lapse rate distinguishes the troposphere from the stratosphere in the figure. The tropopause has more than one definition; 2K/km is one standard (WMO, 1957). Other definitions are based on the lapse rate reversing sign or the chemical composition change. Further discussion is at the end of this chapter. The temperature generally decreases with height (positive lapse rate) with smaller lapse rates in the stratosphere. Over much of the stratosphere, the isotherms are oriented nearly vertically, indicating nearly isothermal vertical temperature profile (and near zero lapse rate). Isothermal lapse rates are much more statically stable than where the vertical temperature gradient is greater in the troposphere. The lapse rate varies, but much of the troposphere has lapse of 5-7 K/km; similar to the 6.5K/km moist adiabatic lapse rate (for lower troposphere conditions). Exceptions to isothermal stratospheric lapses are in the lower stratosphere polar regions, especially during winter, and near the equator. In the troposphere, winter polar regions have higher static stability due to cold air above ice sheets, though the high elevation of Antarctica means temperatures shown for p>700 hPa near the South Pole are not real. B) The tropopause elevation varies with latitude. The tropical tropopause, at 14 to 17 km, is much higher than elsewhere. In polar latitudes the tropopause is at 8 to 10 km. C) The colder temperatures are found along the equatorial tropopause and at high altitudes near the pole in

winter. The former is a consequence of positive lapse rates extending through the depth of the deeper troposphere. The latter is obviously due to the lack of sunlight at the winter pole. D) Figure 3.20 shows various meridional gradients of temperature. In the troposphere, most of the meridional gradient of temperature is found in the middle latitudes. The temperature gradient in the tropics is small. Charney (1961) uses scaling arguments to show that temperature (density and pressure) gradients are order Froude number ($Fr \sim 10^{-3}$) in the tropics and about ten times smaller than middle latitude scaling. In much of the lower stratosphere outside of polar latitudes of the winter hemisphere, the temperature gradient is reversed with warmer temperatures found at higher latitudes and the gradient is poleward. In the tropics the reversed gradient is partly due to the sloping tropopause. Higher up in the stratosphere, the gradient is directed from the winter hemisphere toward the summer hemisphere. The warmest temperatures at each level above 20 km elevation in Figure 3.20 are located at the summer pole; the coldest are at the winter pole. The upper stratosphere temperature pattern is most consistent with the incoming solar radiation (Figures 3.6 and 3.8). (E) The seasonal shift in the temperature is obvious in the stratosphere and more subtle in the troposphere. The warmer stratospheric temperatures occur over the summer pole. The seasonal change in the lower troposphere is more apparent in the Northern Hemisphere than in the Southern.

Figure 3.20 has complexity because the annual mean temperature at a point is influenced by at least four things: (1) radiation processes like: incoming solar absorption, emission from the atmosphere and earth, and how these are affected by chemical composition and cloudiness, (2) temperature advection by the prevailing wind, (3) adiabatic heating by ascent or descent, and (4) diabatic processes like: latent heat release and interaction with the Earth's surface. These four processes are not independent, so it is difficult to assign areas on this figure where an individual process is the prime determinant of the temperature field. The coupling of dynamics, thermodynamics, and radiation make the explanation of the temperature pattern a challenging undertaking. The initial theoretical explanation here (§3.4) will only include simple radiation physics and local convective motions.

Averaged over space and time, the annual mean surface temperature in the Southern Hemisphere is about 1 to 2 K cooler than that for the Northern Hemisphere. The cooler average temperature results from land at the South Pole, leading to much colder temperatures over Antarctica compared with the Arctic.

The temperature field undergoes cyclic variation that differs between Hemispheres. If the temperature were only influenced by the change of warm to cold to warm seasons over a year, then the time variation would be accounted for by the annual cycle. (The annual cycle has period of one year; the semi-annual period is six months.) In addition, it seems logical to expect the

amplitude of the annual variation to be rather small in the tropics and progressively larger at higher latitudes. Near the equator the sun is overhead twice each year, so a semi-annual cycle could be prominent there. Figure 3.21 displays the amplitude of the annual and the semi-annual cycles for [T] at three levels. The levels illustrate surface, middle troposphere, and lower stratosphere time variation. Figure 3.21 has these properties. A) The annual and the semi-annual cycle amplitudes generally increase from equatorial to polar latitudes. The pattern is not a linear function of latitude; it has interesting complexity. B) The figure makes clear that the annual cycle has larger amplitude than the semi-annual, at most places and levels shown. While the sun passes overhead twice a year at low latitudes, the Hadley cells are not symmetric but as will be shown in Chapter 4, the winter hemisphere Hadley cell is much stronger than the summer hemisphere cell. That would cause the meridional wind component to reverse on an annual cycle, and apparently the hemispheric differences in temperature are enough to make the annual cycle stronger than the semi-annual near the surface and in the lower stratosphere as shown. However, van Loon (1972) found the semiannual cycle may account for more than 50% of the total temperature variance between 10N and 20S somewhat more than shown here. In Figure 3.21, at 500 hPa the annual and semi-annual cycles have similar amplitude but both are very small near the equator. C) Outside the tropics the 500 hPa annual cycle is about twice as strong in the Northern Hemisphere. This figure reinforces the repeated assertion that seasonal change is generally greater in the Northern Hemisphere. At the surface, the Northern Hemisphere annual cycle is again stronger in subtropical to polar latitudes, though the difference is greatest for middle latitudes. D) In the lower stratosphere, the Southern Hemisphere has comparable or stronger annual cycle than the opposite Hemisphere in contrast to the troposphere. The largest amplitude shown is above the South Pole at 100 hPa.

Since the annual cycle is much larger than the semi-annual cycle most places, then one has some justification in looking at the ‘extreme’ seasons of the annual cycle: summer or warm season versus winter or cool season. This book, like many documents, captures the variation over the year compactly by comparing averages over these ‘extreme’ seasons. However, the key question is how to define those seasons? It is common but not always the case that the months June through August and December through February are used as ‘meteorological’ seasons (Trenberth, 1983). That specification is central to the next figure.

Interhemispheric temperature differences are difficult to see in Figure 3.20, but are evident in Figure 3.22. The figure is constructed by assuming that monthly average temperatures can represent equivalent points in the seasonal cycle of temperature. Specifically, Northern Hemisphere January is treated as the same part of the winter season as Southern Hemisphere July, and so forth for other months. This assumption ignores how surface temperatures lag

behind the solar cycle Trenberth (1983) by 44 days in the Southern Hemisphere and 32 days in the Northern Hemisphere. Accordingly, only general comments follow. In Figure 3.22, winter is along the left and right edges, summer is in the middle, spring and autumn are a quarter and three-quarters of the way across the abscissa. Three levels are shown, similar to a diagram in van Loon (1972): surface level (2 m), a mid-troposphere level (500 hPa), and a lower stratospheric level (100 hPa). Shaded regions are where the Southern Hemisphere is warmer for the approximately equivalent season. Items worth noting are as follows.

- *Surface and near surface seasonal temperature change*. Between the 30° and 70° latitude, the sizes of the shaded and unshaded areas are similar and which hemisphere is warmer alternates with season. The Southern Hemisphere is warmer during winter months (from 35-70° latitude) but colder during summer. Clearly, the Southern Hemisphere has smaller seasonal change over these latitudes. The greater oceanic coverage of the Southern Hemisphere easily explains this interhemispheric difference. The explanation is partly given in the statement by Benjamin Franklin that commences this chapter. The main missing part, the greater specific heat of water, was known to Franklin's contemporaries; Dalton's 1793 meteorology book refers to smaller heat capacity as the cause of greater seasonal surface temperature changes over land. The seasonal change is less over the oceans. The temperature difference pattern using surface values shows land areas are colder in winter by a greater amount than the land is warmer in summer making the winter values slightly larger magnitude than the summer values. The asymmetry arises from atmospheric stability. In summer, the surface heating destabilizes the atmosphere and consequently, convection can mix the heat in the vertical, which moderates the surface temperatures. In winter, the stronger surface cooling stabilizes the atmosphere near the ground, and large drops in surface temperature can result from the restricted vertical mixing. The latter effect is shallow and hence not apparent at higher levels (e.g. 925 hPa). Averaged over a year, the Southern Hemisphere midlatitudes are warmer at the surface, but slightly cooler at the 925 hPa. Between 10 and 30 degrees latitude, the Northern Hemisphere is warmer. The subtropical belt is warmer all year. Deserts occur at these latitudes in the Northern Hemisphere, while there are primarily oceans in the opposite hemisphere. These latitudes are low enough so that seasonal changes are rather small. Hence, these regions are warmer throughout the year. For latitudes higher than 70°, the Southern Hemisphere is much colder, and is colder all year. That is not surprising since the Arctic polar region is ocean and much of Antarctic is a high-elevation ice field. This temperature difference is somewhat uniform during winter and spring; but as summer goes into early autumn the temperature difference increases, presumably as the Arctic sea ice diminishes, reaching its minimum extent in September.

- *Middle troposphere* (*500 hPa level*). In middle latitudes, the differences between the hemispheres are not as symmetric as they are near the surface. Summer is still colder in the Southern Hemisphere, but winter is no longer much warmer. An explanation for this asymmetric seasonal response again pivots on atmospheric static stability. In winter, the lapse rate is more stable over the continents than over the oceans. Wintertime radiational cooling at the base of the atmosphere increases the static stability of the near-surface air, and the increased stability restricts the vertical mixing of the cooled air. The result is that the greater cooling over the land is mainly limited to the lower troposphere. The effect of surface heating is quite the opposite. Convective activity in summer may mix the stronger surface heating over land area through a larger depth of the atmosphere.
- *Lower stratosphere (100 hPa level).* Very low temperatures occur in the Antarctic stratosphere. Several explanations are proposed by van Loon (1972). Ultra-low temperatures are possibly a complicated result of the surface temperatures being so low that ozone in the stratosphere cannot absorb much terrestrial radiation. Hence, the stratospheric heating by this mechanism is reduced. On the other hand, chemical and dynamical processes are now known to reduce the stratospheric ozone concentrations over Antarctica. The ozone reduction occurs over the course of a winter, with minimum concentrations being reached in spring, a time when the Northern Hemisphere has its largest difference with the Southern in Figure 3.22c.

The first large-scale maps of surface air temperature were probably made by von Humboldt in the early 1800s; the maps were not officially published until 48 years after his death (Hildebrandsson and Teisserenc de Bort, 1907). Though highly smoothed, the isotherms drawn by von Humboldt showed cooler temperatures over eastern Asia and North America, with warmest temperatures over Europe. Other early maps were made by Kupffer (1829; annual mean) and Dove (1862; monthly means).

The surface air temperature pattern is plotted in Figure 3.23 for December-February and June-August. A) Clearly, the surface temperature has both more complex structure and much greater seasonal variation over the continents than over the oceans. The orientation of the isotherms is generally parallel to latitude lines over the oceans while major zonal asymmetries occur near the boundaries of continents. B) Though approximately parallel to latitudes, there is a tendency for colder temperatures on the western sides of the northern oceans. That pattern might seem counter-intuitive given the western boundary currents advect warm water poleward. Sea surface temperatures south of ~30N (~40N) do tend to be warmer on the western than eastern sides of the northern Pacific and Atlantic. The near-surface air temperatures above the WBC have a different history; the air has generally blown off the cold continent. This figure shows colder air temperatures over the WBC than the eastern side of the ocean. But that pattern creates

strong contrasts with the WBC ocean temperatures and results in large surface latent and sensible heat fluxes shown in Figure 3.13a and c. C) The midlatitude and polar land areas are generally colder in winter than the oceans at the same latitude. During summer the land areas are warmer. The seasonal change in temperature is estimated by taking the difference between Figures 3.23a and b. D) Again, as anticipated from Figure 3.22, the seasonal variation is greater over the Northern Hemisphere.

The surface air temperature is strongly influenced by several local effects. Many of the contours in Figure 3.23 outline regions of high elevation (the Andes, Tibet, etc.). Surface properties strongly influence the air temperature (e.g., cold eastern ocean boundary currents like the California current (Figure 3.23b) or cold glacier-covered regions like Greenland and Antarctica). Much of the detailed structure diminishes as elevation above ground increases. A level above the atmospheric boundary layer provides a more comprehensive picture of the thermal structure of much of the troposphere.

The 700 hPa level is a representative level for the tropospheric temperature field. A lower troposphere level is chosen for several reasons. First, one finds almost the same temperature *pattern* at the 300 through 850 hPa levels. Second, using a thermal wind shear argument, this temperature can be related to the surface and 500 hPa geopotential height patterns. Third, the eddy heat fluxes are largest near the 850 to 700 hPa levels (Chapter 7). Figure 3.24 depicts the average temperature fields at 700 hPa for 39 years of winter and summer months.

While isotherms in the Southern Hemisphere line up strongly with latitude, both hemispheres have notable zonal asymmetry, mainly in zonal wave numbers 1, 2, and 3. This long wave pattern reappears in the geopotential and other fields (Chapter 4) as a consequence of the hypsometric equation. During Northern Hemisphere winter, the main thermal troughs are centered near 75 W and 135 E, with a much weaker trough over southeastern Europe (roughly 30 E). The horizontal temperature gradient is strongest near the bases of the two major troughs in the Northern Hemisphere while the Southern Hemisphere winter has stronger gradients over South America and southeast of Africa. During summer, the troughs are less prominent and the gradient is weaker, though again, the seasonal change is more obvious in the Northern Hemisphere. Northern Hemisphere thermal troughs are located over the eastern sides of continents because cold air forms over the central continent and is advected eastward as well as equatorward behind frontal cyclones. The situation in the Southern Hemisphere is different because only South America extends into middle latitudes and it has narrow zonal extent. Southern Hemisphere thermal troughs are weak in Figure 3.24. While the time mean pattern is quite zonal in the Southern Hemisphere, long waves are prominent on any given day. In the

Southern Hemisphere these long waves propagate more readily (due to a comparative lack of topography; Chapter 10) and therefore contribute less to a time average.

3.4 Simple Radiative-convective Models (Temperature Vertical Structure)

Two variations on a radiative balance model can explain the gross features of the vertical profile of temperature. The first model uses radiative equilibrium; however, this model develops super adiabatic lapse rates in the lower atmosphere. The super adiabatic lapse rates are removed by simple convective adjustments in the second model. Though crude, these models can be used to illuminate (a) why the atmospheric lapse rates vary with altitude, including the presence of a tropopause, (b) why the height of the tropopause varies with latitude, and (c) why the lapse rates vary with latitude. Fully explaining these three properties requires further embellishment: incorporating heat transports by large-scale circulations. To keep the discussion as simple as possible, important and complex effects due to clouds are ignored. Hence, the discussion is not intended to be complete. Several books (e.g., Paltridge and Platt, 1976) treat radiation and radiative convective models with greater care and in greater depth than the scope of this book allows.

The original derivation of a radiative balance model for the atmosphere is attributed to Emden (1913). The standard development can be found in Goody and Yung (1989). The discussion here is streamlined and based upon Houghton (1977) and Paltridge and Platt (1976).

Absorption of radiation along a vertical path may be described by Lambert's law or Bouguer's law (Tagirov and Tagirov, 1997), Beer's law, or a combination of these names. The different names arise from expressing the attenuation as a function of distance or absorber concentration. Applied to the atmosphere, there is an additional consideration of scattering that will be assumed captured by the albedo.

Lambert's law states that as a beam of radiation travels through a slab of atmosphere it will be absorbed at a rate proportional to (a) the thickness of the slab dz, (b) the angle of the beam measured from normal to the slab ϕ, (c) the density of the absorber ρ_a, and (d) the intensity of the incident beam of radiation. The incoming radiation could be parallel beam irradiance (I) or radiance (E_I). The path length through the absorber is thus $dX = \sec\phi\, dz$, as shown in Figure 3.25a. Using irradiance, the loss of incident radiation (I) per unit horizontal cross-sectional area as it passes through the absorber is:

$$dI = -I\, k_a\, \rho_a\, dX \tag{3.19}$$

In (3.19) k_a is the mass extinction (absorption) coefficient. To keep the mathematics simple, (3.19) is independent of the radiation wavelength, i.e. the atmosphere is assumed to be a 'gray body'.

Radiation may be diffuse or parallel beam. Parallel-beam radiation describes the solar radiation reaching the Earth to a good approximation. Earth and its atmosphere emit radiation in all directions, so terrestrial radiation is diffuse. The terrestrial radiation could be expressed as radiance or as irradiance from a hemisphere (upward or downward).

Since the Sun is very far away (compared to its radius), solar radiation reaching the earth can be treated as parallel-beam radiation to high accuracy. *In that case*, I is the solar *irradiance*. The solar radiation $I(z)$ is directed downward (z *decreasing*) so that $I(z)$ must increase with height. Integrating (3.19) in the vertical from height z to ∞ gives the irradiance arriving at level z.

$$I(z) = I_0 \exp\left(-\sec\phi \int_z^\infty k_a \, \rho_a \, dz \right) \tag{3.20}$$

where I_0 is the intensity of incident radiation at the top of the atmosphere. The integral

$$O_a = \int_z^\infty k_a \, \rho_a \, dz \tag{3.21}$$

Defines the quantity O_a commonly known as the *optical depth* for absorber a. (Some authors use the optical *path*, which is usually defined as $O_a \sec\phi$.) The optical depth stretches the vertical coordinate as a function of the amount of absorber.

The atmosphere emits as well as absorbs radiation. The emission is not parallel-beam radiation but is diffuse. The emission is a function of solid angle and is expressed as radiance. The irradiance is calculated by integrating this diffuse radiance over all solid angles. One may approximate the atmosphere by plane parallel layers, each indexed by a subscript, j. When radiance is isotropic, then the irradiance I_{ej} is related to radiance by a constant. For all directions and using radiance E_{ej} emitted from layer j, then

$$\int_0^{2\pi} \int_0^{\pi} E_{ej} \sin\phi \, d\phi \, d\lambda = \int_0^{\pi} E_{ej} \, d\omega = 4\pi E_{ej} = 4I_{ej} \tag{3.22}$$

where $d\omega$ is an element of solid angle, ϕ is the angle of incidence relative to the direction normal to the unit horizontal area (Figure 3.25) and λ is the azimuth angle. The second step in (3.22) assumes that the E_{ej} from layer j is isotropic. From the Stefan-Boltzmann law, irradiance is proportional to the temperature (T_j) of the emitter ($I_{ej} = \sigma T_j^4$).

The net radiative transfer dI_j through the slab j is the difference between the radiation absorbed by the slab and the radiation emitted by the slab. *Thus*

$$dI_j = -I_j\, k_a\, \rho_a \sec\phi\, dz + E_{ej}\, k_a\, \rho_a \sec\phi\, dz = dO_a \left(I_j - E_{ej} \right) \sec\phi \tag{3.23}$$

Use is made of $dO_a = -k_a\, \rho_a\, dz$ where the sign reversal is because dz and dO_a increase in opposite directions. Use is also made of Kirchoff's law by using the same k_a in both terms on the right hand side of (3.23). Rearranging (3.23) obtains this radiative transfer equation

$$\cos\phi \frac{dI_j}{dO_a} = I_j - E_{ej} \tag{3.24}$$

Since (3.24) holds for a particular path, the next step is to collapse the angular variation into components (up or down) in the vertical.

This simple radiative equilibrium model will not include absorption of solar radiation directly. Instead, absorption of terrestrial radiance is used. Doing so is justified in a manner similar to separating terrestrial from solar radiation in the glass slab model. Thus, this simple model can be thought to apply to all the wavelengths of terrestrial radiation. In order to integrate over hemispheres pointing up and down incident radiation, I in equations (3.23) and (3.24) will be expressed by incident radiance E_I. Furthermore, (3.24) is a general expression for how radiance changes with optical depth and the subscript 'j' is dropped in favor of vertical integration later. Hence,

$$\cos\phi \frac{dE_I}{dO_a} = E_I - E_e \tag{3.25}$$

The subscript notation E_I in (3.25) is useful since E_I is radiance from layers above or below in a single direction at present.

To collapse the directional dependence, one introduces some definitions. The first definition uses a $\cos\phi$ weighting to obtain the *net* vertical flux of radiant energy I_F (an irradiance) from the radiant energy flux, E_I (a radiance). Hence, integrating over the unit sphere,

$$I_F \equiv \int_0^{\pi} E_I \cos\phi\, d\omega \tag{3.26}$$

Second, define

$$E_I^{\omega} \equiv \frac{1}{4\pi} \int_0^{\pi} E_I\, d\omega \tag{3.27}$$

The E_I^{ω} is the "mean intensity" (Goody and Yung, 1989) or average radiance through a unit horizontal area from all angles integrated over a unit sphere. Next, the 'method of moments' (Goody and Yung, 1989) repeatedly applies the operator: $\cos^n\phi\, d\omega$ to the equation of transfer (3.25) then integrates the resulting equation over solid angles of the unit sphere. The result is several equations that are related. The goal is to remove the troublesome dE_I/dO_a term.

Multiplying (3.25) by $d\omega$ and integrating over all solid angles yields the n=0 moment equation

$$\int_0^{\pi} \cos\phi \frac{dE_I}{dO_a} d\omega = \int_0^{\pi} E_I \, d\omega - \int_0^{\pi} E_e \, d\omega$$
$$\frac{dI_F}{dO_a} = 4\pi E_I^{\omega} - 4\pi E_e^{\omega} = 4\pi E_I^{\omega} - 4I_e \tag{3.28}$$

The second line uses (3.26) and (3.27); I_e is the irradiance of the layer as in (3.22). The second moment equation (n=1) is

$$\int_0^{\pi} \cos^2\phi \frac{dE_I}{dO_a} d\omega = \int_0^{\pi} E_I \cos\phi \, d\omega - \int_0^{\pi} E_e \cos\phi \, d\omega = I_F - \int_0^{\pi} E_e \cos\phi \, d\omega = I_F \tag{3.29}$$

The isotropy of E_e is used to obtain the last form.

A closure assumption is made that separates radiance E_I into upward E_U and downward E_D radiances. Radiant intensity E_I could vary with angle. Upward directed radiance comes from the Earth's surface and from atmospheric layers beneath layer *j*. Downward directed radiance comes from the layers above, and possibly from a source in outer space. Hence the upward could be notably different from the downward flux. Since $\cos\phi$ changes sign between upward and downward facing hemispheres, I_F could be the small difference between two large quantities. So, replacing dE_I/dO_a with its average value over all solid angles in (3.28) would not be wise. In contrast, the $\cos^2\phi$ factor in (3.29) is always positive, so it is more reasonable to replace dE_I/dO_a in (3.29) by its average value $\left(= dE_I^{\omega} / dO_a\right)$. Making that substitution and integrating obtains

$$\int_0^{\pi} \cos^2\phi \frac{dE_I}{dO_a} d\omega = \int_0^{\pi} \cos^2\phi \, \frac{dE_I^{\omega}}{dO_a} \, d\omega = \frac{dE_I^{\omega}}{dO_a} \int_0^{2\pi} \int_0^{\pi} \cos^2\phi \sin\phi \, d\phi \, d\lambda$$
$$= \frac{dE_I^{\omega}}{dO_a} \left(\frac{-2\pi}{3}\right) \cos^3\phi \Big|_0^{\pi} = \left(\frac{4\pi}{3}\right) \frac{dE_I^{\omega}}{dO_a} = I_F \tag{3.30}$$

Taking the derivative of (3.28) with respect to O_a obtains

$$\frac{d^2 I_F}{dO_a^2} = 4\pi \frac{dE_I^{\omega}}{dO_a} - 4\frac{dI_e}{dO_a} = 3I_F - 4\frac{dI_e}{dO_a} \tag{3.31}$$

A layer of air could be heated or cooled radiatively if there is a divergence of the radiant energy flux, I_F. Furthermore, horizontal divergence is essentially zero since horizontal differences of I_F can be assumed to be much smaller than vertical differences. Hence the divergence of I_F is given by dI_F/dO_a. If the atmosphere is in radiative equilibrium, then it is neither heating up nor cooling down. Recall, absorption of solar radiation in a layer is ignored. For any layer dO_a thick, *the amount of energy entering that layer must equal the amount leaving*

that layer otherwise the layer heats up or cools down; that situation implies I_F is a constant in the vertical and that $dI_F/dO_a = 0 = d^2I_F/dO_a^2$.

Radiative equilibrium with neglected horizontal variations reduces (3.31) to

$$3I_F = 4\frac{dI_e}{dO_a} \tag{3.32}$$

From partitioning E_I in (3.26)

$$\begin{aligned} I_F &= \int_0^{\pi/2} E_U \cos\phi\, d\omega + \int_{\pi/2}^{\pi} E_D \cos\phi\, d\omega \\ &= \int_0^{2\pi}\int_0^{\pi/2} E_U \cos\phi \sin\phi\, d\phi d\lambda + \int_0^{2\pi}\int_{\pi/2}^{\pi} E_D \cos\phi \sin\phi\, d\phi d\lambda = \pi\left(E_U - E_D\right) \end{aligned} \tag{3.33}$$

Equation (3.33) means that I_F is the difference between the irradiance directed upward and the irradiance directed downward for radiative balance. Figure 3.25d-f shows the geometry consistent with (3.33). *Since (i) no solar absorption by the air is included and (ii) the air cannot be heating up, then the difference I_F must be the same as the amount of solar radiation absorbed by the ground*. A second equation involving E_U and E_D is obtained from (3.27)

$$E_I^{\omega} = \frac{1}{2}\left(E_U + E_D\right) \tag{3.34}$$

Use is made of the assumption that E_U and E_D are isotropic within their respective hemispheres. Assuming that $dI_F / dO_a = 0$ then (3.28) becomes

$$0 = 4\pi E_I^{\omega} - 4I_e \tag{3.35}$$

Eliminating E_U and E_I^{ω} from (3.33) and (3.34) then (3.35) becomes

$$I_e\left(O_a\right) = \frac{I_F}{2} + \pi E_D \tag{3.36}$$

At the top of the atmosphere, $E_D = 0$ (figure 3.25d), so

$$\sigma T_{sa}^4 = I_e\left(O_a = 0\right) = \frac{I_F}{2} \tag{3.37}$$

This equation defines the 'skin temperature' T_{sa} at the top of the atmosphere. Eliminating E_D and E_I^{ω} from (3.33) and (3.34) by using (3.28) obtains

$$I_e\left(O_a\right) = -\frac{I_F}{2} + \pi E_U \tag{3.38}$$

At the bottom of the atmosphere, the only contribution to E_U is from Earth's surface (not the atmosphere, figure 3.25f) hence E_U can be expressed in terms of the surface temperature T_G. Hence

$$\sigma T_G^4 = I_G = I_e(at\ ground) = \pi E_U = I_e\left(O_{ab}\right) + \frac{I_F}{2} \tag{3.39}$$

The optical depth at the bottom of the atmosphere is O_{ab} and the irradiance from the Earth's surface is I_G. To obtain the atmospheric irradiance at other levels, one integrates (3.32) downward from $O_a=0$ to O_a using (3.37) and noting that I_F is constant.

$$\int_0^{O_a} dI_e = I_e\left(O_a\right) - I_e\left(0\right) = I_e\left(O_a\right) - \frac{I_F}{2} = \frac{3}{4} I_F\, O_a \tag{3.40}$$

And thus

$$\sigma T_A^4 = I_e\left(O_a\right) = I_F\left(\frac{1}{2} + \frac{3}{4} O_a\right) \tag{3.41}$$

(3.41) defines the temperature of the atmosphere as a function of optical depth. Substituting (3.41) at O_{ab} into (3.39) obtains the Earth's surface temperature.

$$\sigma T_G^4 = I_e\left(O_{ab}\right) + \frac{I_F}{2} = I_F\left(1 + \frac{3}{4} O_{ab}\right) \tag{3.42}$$

Three things are noteworthy about these last two equations.

(i) The temperature T_G exceeds the value it would have if solely due to absorbing solar radiation (= I_F) as long as the atmosphere absorbs some (terrestrial) radiation ($O_{ab}>0$). Atmospheric absorption is given by the optical depth, so $O_a >0$ the right hand side of (3.42) is $>I_F$.

(ii) There is a discontinuity between the atmospheric temperature at the base of the atmosphere and the ground temperature in this model. O_a is the same in both cases but the right hand sides of (3.41) and (3.42) differ.

(iii) Since there is a net upward flux, then $E_U>E_D$ and that requires the temperature to be greater below than above at *every* level. To have a stratosphere, where temperature is isothermal or increases with elevation, then another process is needed, specifically, absorption of solar radiation by an atmospheric constituent.

Before temperature profiles, skin temperatures, and surface temperatures may be estimated, one needs to know I_F and O_{ab}.

The solar flux received at the earth's average orbital distance from the sun is I_{Sol} = 1380 W m^{-2}. The use of daily averages of the insolation ($Q_{sol}/24$) is reasonable since the radiative cooling rates are small (a few degrees per day, Bernstein et al., 1996) compared to the range of temperature over the depth of the troposphere (or as seen in Figure 3.20 of [T]). The average Earth albedo (Figure 3.7) A_{lbd} = 0.31. If I_F is the solar energy absorbed, then for energy balance the skin temperature is

$$\mathrm{T}_{sa} = \left(\frac{I_F}{2\sigma}\right)^{\frac{1}{4}} = \left(\frac{I_{Sol}[1 - A_{lbd}]}{8\sigma}\right)^{\frac{1}{4}} = 214\mathrm{K} \tag{3.43}$$

where the factor of four in the denominator arises because the solar flux hits the cross-sectional disk of the earth (πr^2 where r is the earth's radius) but the emission is assumed uniformly spread over the whole earth's surface ($4\pi r^2$).

If the absorber O_a (including the value at the bottom of the atmosphere, O_{ab}) has a simple exponential variation with elevation, then one obtains a comparatively simple T_A profile. Goody and Yung (1989) use an exponential profile proportional to the distribution of *water* vapor (not dry air) density in the atmosphere.

$$O_a(z) = O_{ab} \exp\left(-\frac{z}{H_w}\right) \tag{3.44}$$

where H_w = 2 km is an appropriate scale height for water vapor according to Goody and Yung (1989). Substituting (3.44) into (3.41) gives

$$\mathrm{T}_A(z) = \left[\frac{I_F}{2\sigma}\left\{1+\frac{3}{2}O_{ab}\exp(-\frac{z}{H_w})\right\}\right]^{\frac{1}{4}} \tag{3.45}$$

For radiative equilibrium, the solar energy absorbed by the earth must balance that lost to space by infrared emission.

Radiative equilibrium temperature profiles are easily calculated from (3.41) and (3.42) once the optical depth is known. The optical depth will respond to different absorbers, which have different vertical profiles. Equation (3.44) assumes water vapor varies exponentially. In contrast, naturally occurring ozone has highest concentrations in the middle stratosphere. Figure 3.26a approximates the ozone profile with a simple function

$$\rho_{o_3} = Bz^2 \exp(bz) \tag{3.46}$$

The corresponding optical depth, due only to ozone, is

$$O_{o_3} = \frac{k_{O_3} B}{b}\left(2\frac{z}{b} - z^2 - \frac{2}{b^2}\right)\exp(bz) \tag{3.47}$$

Radiative equilibrium profiles for the ozone and water vapor absorptions, separately and together, are illustrated in Figure 3.26. However, the figure intentionally exaggerates the different temperature profiles created by using an ozone density that is five orders of magnitude larger than typical atmospheric values.

The solutions asymptotically approach 214 K as $O_a \rightarrow 0$ (Figure 3.26b, dashed line). For $O_a \rightarrow 0$ the atmosphere is nearly transparent and is isothermal at the skin temperature; the ground temperature is 40.5 K larger.

For water vapor, the equilibrium temperature profile follows the skin temperature in the high atmosphere because there is no vapor there. At low levels the temperature changes rapidly with height (Figure 3.26b, solid line). The temperature discontinuity at the bottom is 23.6 K. The lapse rate ($\Gamma = -\partial T_A / \partial z$) with height increases as z decreases and increases for larger values of O_{ab}. Larger O_{ab} diminishes the temperature discontinuity. Goody and Yung (1989) make a similar calculation and find the discontinuity between surface and air temperatures to be 11.3 K for $O_{ab} = 4$, but 16.7 K for $O_{ab} = 2$. The lapse rates in the lower troposphere become so large that they exceed the dry adiabatic lapse rate when O_{ab} is greater than about 0.5. Obviously, such convectively unstable lapse rates are another unrealistic feature of a radiative equilibrium model. Superadiabatic lapse rates are partly a reflection of the rapid exponential change of the water vapor due to the 2 km scale height.

The ozone profile chosen has a smoother variation with height (8 km scale height). The ozone profile does not develop superadiabatic lapse rates (Figure 3.26b, dot-dashed line). The ozone concentration becomes small in the troposphere so the optical depth changes more slowly with elevation. Consequently, the equilibrium temperature profile does not change much in the troposphere. The surface temperature discontinuity is 27.8 K.

When the ozone and water vapor absorptions are combined (dotted line), the result exhibits properties of both absorbers. In these calculations solar absorption is absent. Ozone is an effective absorber of solar radiation in the stratosphere. Incorporation of that effect can lead to increasing temperature with height in the lower stratosphere, a feature not present in Figure 3.26b.

Unrealistic features of the radiative equilibrium model include:

1) temperature discontinuity at the Earth's surface and a possible superadiabatic lapse rate,
2) no solar absorption by the atmosphere (related: no stratosphere),
3) no horizontal heat fluxes, and
4) no effects caused by clouds.

We consider solutions to these issues in turn.

1) Superadiabatic lapse rate and temperature discontinuity correction. One expects dry convection to quickly remove superadiabatic lapse rates and surface heat fluxes to reduce the atmosphere-surface discontinuity to a few degrees. A model that can make both corrections is called a radiative-convective equilibrium (RCE) model. RCE models balance the *vertical* energy transfer across a layer by both radiative processes and convective transport.

One solution is to specify a maximum lapse rate, Γ_x. A trivial example replaces any lapse rate in excess of Γ_x with that maximum lapse rate. For the water vapor T_A profile, the result looks like the dotted curve in Figure 3.26c. Clearly, everywhere the profile was adjusted is colder than before so there is less radiance from these layers and the model is not in equilibrium, furthermore, it does not recognize that convection transfers heat vertically. The radiant flux at the top of the convective layer must match the radiative equilibrium flux I_F being transported across all the other levels above. The amount coming from below is an accumulation, so the amount exiting the adjusted layer is too small. Therefore, the convectively-adjusted profile must have upper levels that are warmer than the purely radiative profile and lower levels that might be colder. To properly include the role of convection one needs to formulate how that convection transports heat vertically. To address the unrealistic discontinuity at the surface, the RCE model must also include surface heat fluxes into the atmosphere; these cool T_G while elevating $T_A(z)$ near $z=0$. Conceptually, the result may look similar to the dashed line in Figure 3.26c.

A constant lapse rate $\Gamma = 6.5$ K km^{-1} is used in Figure 3.26c (the dashed lines). Near the surface, this lapse rate would be similar to the moist adiabatic lapse rate for typical middle latitude conditions. The actual moist adiabatic lapse rate varies with the moisture content of the air; it can be as little as 3 K km^{-1} near the surface in the tropics and approaches the dry adiabatic rate (9.8 K km^{-1}) in the upper atmosphere.

The radiative flux is no longer constant in the radiative-convective model troposphere, so an equation like (3.31) must be used instead of (3.32). In addition, the convective layer extends higher than the level at which the radiative-equilibrium temperature profile (3.45) has lapse rate equal to Γ (dashed versus dotted lines in Figure 3.26c). The resulting temperature profile is similar to the observed annual and global horizontal average temperature profile. This agreement is partly built in by using a fixed Γ that is similar to the observed lapse rate. The height of this moist adiabatic layer, the model "tropopause" is not specified, but is a model result; it is comparable to observed heights (Figure 3.20).

Manabe and Strickler (1964) and Manabe and Wetherald (1967) introduce several further modifications to the RCE model. Their model differs from that just shown in the following ways: (a) a specific latitude (35 N), time of year (April), and local albedo (0.102) are used; (b) observed profiles of H_2O, O_3, and CO_2 are employed; and (c) the atmosphere is allowed to absorb solar radiation. The amount of water vapor present at saturation is temperature-dependent, so the concentration and hence the optical depth from water vapor in these models can produce a positive feedback. A runaway "greenhouse" warming is possible (Renno and Huang, 2015 have a review).

2) Solar absorption can make a "Stratosphere" inversion: Much of the stratosphere shown in Figure 3.20 has temperature increasing with elevation; it does mainly due to absorption of solar radiation by ozone. The two layer glass slab model can reproduce this negative lapse rate if we give the upper layer *ad hoc* "stratospheric" values and the lower layer corresponding "tropospheric" values. This variation differs from the two layer model of (3.11) - (3.13) in allowing both the shortwave and the longwave absorptivities to differ between the layers. Averaged over the globe, the tropopause is at roughly 200 hPa implying our upper layer has about a quarter the mass of the lower layer. Figure 3.3 indicates that 23% of the solar radiation is absorbed by the atmosphere. The scale height for water vapor (~2km) is small so nearly all of it is in the lower layer. Nearly all the ozone is in the upper layer. From Figure 3.1, ozone and water vapor are primary solar absorbers; the solar absorptivities assumed are a_{s1}=0.15, and a_{s2}=0.08. Figure 3.3 indicates a net atmospheric transmission fraction of surface longwave radiation to space of 40/(356+40) = ~10%, implying $a_{L2} + a_{L1}$ =0.9. Figure 3.2 shows that water vapor is a major absorber (entirely in the lower layer); there is some ozone absorption (all in the upper layer); and CO_2 absorption follows the mass within each layer; the longwave absorptivities chosen are a_{L1}=0.8, and a_{L2}=0.1. Using I_{IN} = 239 W/m^2 obtains I_2 =216.4 Wm^{-2}, I_1 =212.7 Wm^{-2}, and I_G =362.6 Wm^{-2}. Those blackbody irradiances translate into temperatures T_2 =248.5 K, T_1 =247.5 K, and T_G =282.8 K. This example has increasing temperatures with elevation, T_2>T_1 because the upper layer has a higher enough ratio of shortwave over longwave emissivity compared with the lower layer. The upper layer has four times larger ratio. Hence, the lower layer can emit longwave more effectively than it absorbs shortwave. But, the upper layer does not emit longwave radiation as effectively as it absorbs solar radiation.

Local radiative balance is proposed to approximate the stratospheric temperatures, with convection invoked in the troposphere. Both approaches are too simplistic but provide a starting point for improvements. With some embellishment from meridional heat fluxes, calculated temperature profiles can reflect the observed latitudinal differences. Horizontal heat fluxes are necessary because the incoming radiation (Figure 3.6) has a greater latitudinal variation than the outgoing radiation. Local radiative balance may not be compatible with a balanced circulation (Shine, 1987). Nonetheless, radiative equilibrium provides a first approximation to the stratospheric temperatures. The troposphere is sensitive to earth surface temperatures that have more "thermal inertia" (take more time to change with seasons) than stratospheric air. In addition, the stratosphere contains few clouds, whose seasonal changes in the troposphere partially oppose the seasonal changes in radiation (Figure 3.7). Hence, stratospheric temperatures respond to solar radiation more directly than do tropospheric temperatures. And, seasonal

changes of tropospheric weather lag the solar cycle by about a month, but little lag is apparent in stratospheric data (e.g., Geller and Wu, 1987).

3) Horizontal heat transport. Horizontal heat transports are expected from the net radiation curves described in §3.1. Liou and Ou (1983) compare solutions from two types of models. The temperature profiles obtained by their one-dimensional model (using climatological cloud distributions that vary with latitude) are further improved by adding horizontal heat transports in three hemispheric belts (tropical, midlatitude=, and polar). The observed transport of sensible heat is plotted in Figures 3.15 and 3.17. Below about 4 km the poleward heat transport into the midlatitude from the tropical belt exceeds the transport out to the polar belt. Higher up, the transport out to the polar belt slightly exceeds the input from the tropical belt. One can anticipate the following changes from RCE: net heat transport out of the tropics will lower the tropospheric temperatures in that belt; net convergence in the polar belt and in midlatitudes (below 4 km) will raise the temperatures in those belts relative to local RCE.

4) Cloud effects. Clouds have a complex effect upon the temperature profile. The net effect varies with cloud altitude because of two competing effects. First, clouds reflect solar radiation (a cooling effect). Second, clouds can trap infrared terrestrial radiation (a heating effect). Because the cloud is opaque to infrared radiation, a sufficiently thick cloud absorbs nearly all the radiation emitted from the earth's surface; the heat trapping occurs because the typical cloud emits less radiation to space than does the earth's surface because the cloud is cooler. For example, Liou and Ou (1983) find, as in previous studies with clouds (e.g., Manabe and Strickler, 1964), that middle clouds reduce the temperatures throughout the troposphere. Low clouds reduce the temperatures even more. In contrast, high clouds (located just below or even above the tropopause) can increase the temperatures throughout the troposphere. The first effect, the reflection effect, dominates for low and middle clouds. For high clouds, their temperatures are so low that the second effect, the trapping effect, dominates. Clouds occur at many elevations in the atmosphere. On a global average, the cooling effect from reflection dominates, according to satellite observations (e.g., Rossow and Schiffer, 1991). They found the heating and cooling to be very large but nearly canceling in the tropics; the global average cloud cooling was largely due to middle latitude clouds.

The two-layer glass slab model can illustrate the two effects. Consider two versions of the model, one as depicted in Figure 3.5b and the other with a thick cloud in the upper layer that absorbs all radiation upwelling from below the cloud. Let the model represent a region having a mixture of clear sky and upper layer cloud with the cloud occupying fraction F_{cld} of the region. The atmosphere is assumed to not absorb solar radiation. The upper layer is assumed to a) not absorb longwave radiation where the skies are clear but b) absorb all longwave radiation where

there is cloud. The albedo of the clear sky is assumed to be A_{lbd_nc} and for the cloudy sky A_{lbd_c} where the latter exceeds the former. The TOA energy balance becomes:

$$\left(1-F_{cld}A_{lbd\_c}-\left\{1-F_{cld}\right\}A_{lbd\_nc}\right)I_s=F_{cld}\sigma T_2^4+\left\{1-F_{cld}\right\}\left(a_{L1}\sigma T_1^4+\left\{1-a_{L1}\right\}\sigma T_G^4\right) \qquad (3.48)$$

The upper layer temperature, T_2 is treated as the cloud top temperature. Consider two special cases. The first case illustrates the trapping effect by assuming the fraction of cloud and its albedo are held constant but the cloud top is raised. Doing so will initially lower T_2 which means that the ground T_G and likely the lower layer, T_1 temperatures must increase to compensate. The second case illustrates the reflection effect by holding the cloud top at constant temperature but increasing the albedo of the cloud (A_{lbd_c}). Doing so reduces the left hand side of (3.48) which must be compensated by reduced T_G and likely T_1 temperatures. Specifying the cloud top temperature (T_2), both albedos, and the cloud fraction, one can solve for ground temperature T_G. Choosing A_{lbd_c}=0.8 and A_{lbd_nc}=0.1 (roughly consistent with Figure 3.7) a_{L1}=0.85, and solar constant I_S=341, then the ground temperature T_G decreases as T_2 becomes colder when the nonzero cloud fraction is < ~0.46; the reflection effect. T_G increases as T_2 decreases for cloud fractions > ~0.46; the trapping effect. This model shows both effects. Hartmann (1994) has a similar simple model of clouds with the constraint of net radiative balance relaxed. He calculates the change in TOA net radiation as a function of the albedo change versus the change in cloud top temperature (proportional to altitude assuming a constant lapse rate). For large albedo changes and warmer cloud tops the net radiation declines because the higher albedo reflects more incoming radiation and the lower cloud is more effective at losing energy to space; for higher cloud altitudes and smaller albedo the opposite happens. When the reduced OLR balances the reduced absorbed solar radiation, Hartmann finds a cloud top elevation of ~10km for an albedo change of 0.4 which corresponds to about 225K broadly consistent with the glass slab model results described and the tropopause elevation at latitude ~38 degrees (where net radiation is zero) in Figure 3.20.

Figure 3.27, from Zhang et al. (2004) shows meridional cross sections of annual average radiant energy *gained below the indicated pressure level*. Ozone and other atmospheric shortwave absorption reduce I_F reaching levels below (I_F decreases as optical depth increases). Figure 3.27a shows the decreasing I_F as elevation decreases. The decrease is more obvious in the tropical troposphere due to the higher water vapor content and flat gradient with respect to latitude. The ozone absorption can be seen in Figure 3.27a as contours that deviate slightly from vertical at pressures <100 hPa. The longwave radiation (Figure 3.27b) is negative because layers below are losing radiant energy. The distribution of longwave radiation is comparatively flat as anticipated from earlier figures such as 3.8a. Because the atmosphere is more effective at absorbing longwave than shortwave radiation, the vertical trend is stronger in (b) than in (a). The

net radiation (Figure 3.27c) for clear sky is zero ~50 degrees latitude at TOA which is much poleward of the ~38 degrees latitude observed (Figure 3.8a). At lower elevations the net radiation is zero for clear sky conditions at much higher latitudes. This discrepancy is removed by adding clouds. The change due to adding clouds is shown in the right column of Figure 3.27. Clouds reflect sunlight so they always reduce I_F in Figure 3.27d. The reduction of I_F reflect these categories of cloudy areas: deep tropical convection, stronger but lower altitude cloudiness in middle latitudes with a relative minimum in the subtropics. In contrast, the clouds are trapping longwave radiation (Figure 3.27e), especially at high elevations near the equator and middle and lower levels of the middle and high latitudes. The cloud increment is longwave radiation again reveals the vertical distribution of clouds (shown later). Figure 3.27f shows that clouds reduce the net radiation for most latitudes but increase it for high latitudes. The cloud increment reduces the clear sky net radiation at TOA more strongly in middle latitudes. The combination of clear and cloud increments leads to net radiation becoming zero where we expect it ~38 degrees latitude. Figure 3.8a has latitude profiles at TOA for solar, longwave, and net radiation that compares with the corresponding sum of each of these pairs of Figure 3.27: (a+d), (b+e), and (c+f) along their top edge. Figure 3.6a has surface solar (sw_s) that compares with the bottom edge of combining panels (a) and (d).

3.5 Towards deeper understanding of the Stratosphere and Tropopause

In the RCE model the ‘troposphere’ was cast as a layer of constant lapse rate beneath a stratosphere in RCE. The full picture is more complex and interesting. First, the troposphere is more than a layer of lower static stability. It is also a layer of vigorous vertical mixing by a mixture of tropical convection and in middle latitudes by extratropical frontal systems, both of which are organized on a range of scales. Indeed, the word ‘tropos’ in Greek translates as ‘turning’ in English. The upward portion of the large scale overturning often leads to condensational diabatic heating, and heating obviously impacts temperature.

What is it about the overturning that determines the depth H_T?

A relation between the depth, H_T of the constant lapse rate ‘troposphere’ and ‘dynamical heating’ by baroclinic eddies was developed by Held (1982) but it requires arbitrary correction to approximate the observed tropospheric depth. Accepting the arbitrary choices finds H_T to increase with any of these changes: meridional temperature gradient magnitude increase, latitude increase ($|f/\beta|$ increase), and/or static stability decrease – such changes facilitate baroclinic instability. Figure 3.20 shows the tropopause elevation decreasing when moving from middle to high latitudes.

However, other works emphasize a balance between clear sky radiative cooling and subsidence warming. The balance is seen by equating the diabatic and vertical advection terms in (C.10), the tendency equation for dry static energy. The result can be rearranged as

$$\omega\left(C_P\frac{\partial T}{\partial p}+g\frac{\partial Z}{\partial p}\right)=\omega\left(C_P\frac{\partial T}{-\rho g\partial z}+g\frac{\partial Z}{-\rho g\partial z}\right)=D_J\ \rightarrow\ \frac{-\omega}{C_P\rho g}\left(\frac{\partial T}{\partial z}+\frac{g}{C_P}\right)=\frac{D_J}{C_P}\rightarrow$$
$$\omega\left(\Gamma_d-\Gamma\right)=-\frac{\rho g D_J}{C_P}\rightarrow\omega_D=-\frac{\rho g D_J}{C_P\left(\Gamma_d-\Gamma\right)} \qquad (3.49)$$

Hydrostatic balance (C.12) is used, the atmospheric lapse rate is $\Gamma=-(\partial T/\partial z)$, and other quantities are defined in the Appendices. The pressure velocity ω_D defined by (3.49) is sometimes called the 'diabatic vertical velocity' (e.g. Zelinka and Hartmann, 2010) since horizontal heat fluxes are ignored (due to weak tropical temperature gradients). Greater cooling or lower static stability increase sinking (ω_D >0). There is no latent heating in clear sky leaving D_J to be mainly from radiative cooling there. Water vapor has a scale height a third to a fourth of the dry air scale height, so there is little water vapor at high elevations (P<200 hPa) leaving CO_2 primal in radiative balance (Hartmann and Larson, 2002). Radiative cooling in the middle and lower troposphere is needed to create the static instability that is removed by convection that in turn produces condensation/deposition heating. Within the moist convection a relation similar to (3.49) can be assumed, this time condensation/deposition latent heating balances the cooling. Convection predominates in the tropics and is often deep, but the instability initiating it is set up by the clear sky radiation (Hartmann and Larson, 2002). Above 200 hPa, the radiative cooling rapidly decreases with pressure so another mechanism is needed to drive the sinking. From mass balance, the divergence at the tops of tropical clouds enhances convergence and subsidence in adjacent clear-sky areas. The divergence is greater at elevations where the highest clouds are most numerous (anvil tops of thunderstorms). The temperature of those cloud tops is nearly insensitive to the surface temperatures (Larson and Hartmann, 2003) in a mesoscale model calculation and hence, so is the level of this 'tropopause'.

Using the change of lapse rate (<2C/km) to identify the "tropopause" is problematic (Highwood and Hoskins, 1998). The actual tropical tropopause is even higher. Several factors interplay. 1) Most of the mass transport from the surface and troposphere occurs in the tropics. 2) The height of the tops of ICZ thunderstorm anvils is higher in certain regions: central and western Pacific (in DJF; 175-200E @ equator) and over India (in JJA; 45-100E @ 25N). 3) Mixing ratio is ~3ppm by volume in the stratosphere but no less than 10ppm the tropical troposphere (Highwood and Hoskins, 1998). To reach such low values the air transported into the stratosphere must be "freeze dried" by passing through a "cold point" minimum temperature <191K (Newel1 and Gould-Stewart, 1981). 4) Along the ICZ, on average, the cloud tops as

determined from OLR reach ~12km, but the cold point is closer to 16km (Forster et al., 1997). The likely resolution involves a combination of factors. First, the thunderstorms have overshooting tops that extend above the thunderstorm anvils. Second, those regions of the globe identified in this paragraph have clouds that extend to much higher elevations; while those regions cover a relatively small area of the tropics it will be shown later that most of the rising motion in the tropics is concentrated into a small space, about 1% of the tropics. Third, the 'stratospheric pump' (e.g. Holton, et al., 1995) provides additional lift to the air and further adiabatic cooling. Finally, the boundary between the troposphere and stratosphere in the tropics is more of a layer and is less distinct than in higher latitudes.

To summarize this chapter, the uneven spatial distribution of radiation sets up an uneven spatial distribution of temperature. The horizontal structure has weak temperature gradient in the tropics and concentrated temperature gradients in midlatitudes. The vertical structure of temperature can be approximated (roughly) with simple radiative balance in the stratosphere, but in the troposphere overturning circulations predominate and create a different temperature structure that largely matches the moist adiabatic lapse rate. What is absorbed as input must be lost as output. However, the input structure differs from the output structure which implies transports of heat in sensible and latent forms and via oceanic as well as atmospheric circulations. The hemispheres respond differently. The amplitude of the seasonal cycle is less in the more oceanic SH. There is more emission from the NH surface than in the SH, but the NH clouds tend to be higher and emit less from those cloud tops than in the SH; so, asymmetries at the surface are smaller at the TOA (Stephens and L'Ecuyer, 2015). Despite large differences in the polar region geography and in the areas of land versus ocean in midlatitudes, the latitude where zonal mean net radiation is zero (and zonal mean meridional heat flux is maximized) is very similar in both hemispheres (~35N and ~37S in Stephens and L'Ecuyer). However, the fluxes are not the same, the SH has greater emission to space during local winter (e.g. July) when the Earth is further from the Sun. More heat is extracted from higher latitudes of the NH summer (up to 20N) to balance the SH winter loss than the NH draws from the SH (up to -12S) during the opposite season (e.g. January). This result sets the stage for both the dominance of the winter Hadley cell and its interhemispheric differences, subjects of the next chapter.

Problem Sets

1. Radiative equilibrium. Daily total Q_{Sol} insolation at latitude φ, for solar declination angle δ, for the half length of daylight (in radians) H_L , and assuming the Earth's distance from the Sun is a constant is given by:

$$Q_{Sol} = \frac{24(hrs)}{\pi} I_{Sol} \left(H_L \sin\varphi \sin\delta + \cos\varphi \cos\delta \sin H_L \right) \tag{3.50}$$

(e.g. Peixoto and Oort, 1992). Where the length of daylight is given by

$$2H_L = 2\arccos\left\{ -\tan\varphi \tan\delta \right\}$$

(Note: if the sun does not rise or set at a location, the formula is undefined and $2H_L=2\pi$.)
Consider two locations (equator and North Pole) at the summer solstice (δ=23.5 in degrees).
a. Find δ in radians
b. Find the length of daylight at both locations. (Show your work.)
c. Find Q_{Sol} at both locations. Note that Q_{Sol} has units: W m^{-2} in 24 hours. All angles used should be in radians.
d. From the relation that $I_{IN} = a_{SG} Q_{Sol} / 24$, use the glass slab model equations to find T_A and T_G at both locations given: a_{SG} = 0.75 at the equator and =0.35 at the North Pole. Assume that a_{SA} = 0.3 and a_{LA} = 0.9 at both locations.
e. How do these T_G temperatures compare with Figure 3.20?

2. Radiative equilibrium. Using (3.50) find the radiative equilibrium temperature from Q_{Sol} for these situations: (i) equator at the equinox, (ii) 38N at the equinox, (iii) 38N at the summer solstice (23.5 degree declination) (iv) 38N at the winter solstice (v) north pole at the summer solstice. Hint: be aware that the units of Q_0 are W m^{-2} (24 hrs).

a. Find the daily insolation for the 5 situations in the problem description
b. Find the radiative equilibrium temperature for the 5 situations in part a) assuming a blackbody.
c. Repeat part b except using these greybody shortwave reflectivities: (i) 0.1, (ii)-(iv) 0.2, (v) 0.7 and greybody longwave emissivities of 0.9 in each case.
d. Find the radiative equilibrium temperature for the earth as a whole assuming it to be a blackbody.

e. Start with the expression for Q_{Sol} above then write down the general expression for the precise latitude where the *average* daily insolation (units = W/m^2) equals the radiative equilibrium value for the whole Earth. Then solve the expression for that latitude at the vernal equinox to 5 significant digits.
f. Using your general formula in part e, find the latitude where the average daily insolation equals the radiative equilibrium value for the whole Earth at the northern winter ('December') solstice. A graphical solution, using I_{Sol} =1368 is adequate with accuracy to the nearest 0.1 degree.

3. Radiation and temperature. The table shows radiative quantities at various locations.

Location	TOA solar (W/m^2)	Absorbed solar (W/m^2)	Terrestrial (W/m^2)
North Pole	175	75	195
38 N	340	235	235
Equator	415	320	250

a. Calculate the average annual albedo at each of the 3 stations from this data. Obtain albedo values at these 3 locations from Figure 3.7a. (Use ERBE data.) Discuss similarities and/or differences between the 2 sets of estimates.
b. Assume that emissivity is constant and equals 0.9 for the spectrum of terrestrial emission. Calculate the implied annual mean temperatures for each location based on local radiative balance, i.e. upon using the absorbed solar radiation in the Stefan-Boltzmann law. Calculate the implied annual mean temperature based upon the terrestrial emissions. (There are 5 distinct values, since absorbed solar radiation and terrestrial emission are the same at 38N.)
c. Calculate the difference (=ΔT) in temperature between using the actual emission minus temperature from solar absorption at the Equator and at the North Pole. What percent of the difference is due to heat transport at the two locations? 'Percent' means *{ΔT / local solar absorption-based T}*100%* so the percentage is <0 at the equator.

4. Glass slab model for Mars. The albedo of Mars ranges from 0.1 to 0.4. During a global dust storm assume the global average albedo is 0.3. The solar constant at Mars orbit is 590 W/m^2. The atmosphere is thin but the dust absorbs solar radiation so that a_{SA} = 0.1 also the atmosphere is composed mainly of a good longwave absorber CO_2 plus the dust is highly absorbent so a_{LA} =

0.4. Assume that 10% of the solar radiation is scattered back to space by the dusty atmosphere. Assume the surface is a blackbody for longwave radiation.
a. Find the amount of SOLAR radiation absorbed by the surface on a global average.
b. For these conditions calculate the temperature of the atmosphere and of the ground.
c. The dust storm clears so that the atmosphere is more transparent to sunlight and less absorbing of longwave radiation such that a_{SA} = 0.02 and a_{LA} = 0.1. Atmospheric scattering and a_{SG} are the same as in part a. With these changes, find the amount of solar radiation absorbed by the surface and then calculate the atmosphere and ground temperatures for these new conditions.

5. Glass slab model of the stratosphere. Figure 3.1 shows more solar radiation is absorbed by H_2O than by O_3, hence $a_{S1}>a_{S2}$ in the two layer glass slab model. Figure 3.3 shows more infrared radiation is absorbed by H_2O than by O_3, hence $a_{L1}>a_{L2}$ and the total solar absorption by the atmosphere is ~23%. Make a simplifying assumption that $a_{S1}+a_{S2}=0.23$ and constrain a_{S2} to have small size (<0.1).
a. Find (by iteration) the values of a_{S1} and a_{S2} where the upper layer temperature (T_2) exceeds the lower layer temperature (T_1) by no more than 0.5K for these combinations of longwave absorptivities: $a_{L1}=0.78$ with $a_{L2}=0.12$, $a_{L1}=0.8$ with $a_{L2}=0.1$, $a_{L1}=0.85$ with $a_{L2}=0.05$. Print each combination of a_{S1}, a_{S2} T_1, T_2, and T_G for each case.
b. Summarize how the shortwave absorptivities change to maintain the matching temperatures as more and more of the longwave absorption occurs in the lower layer.

6. Estimating what level corresponds to the air temperature in the glass slab model where the ground emissivity is no longer 1.0 but is a_{LG} = 0.97. Let a_{SA}=0.2852.
a. Modify (3.1) and (3.2) to include a_{LG}.
b. Derive the modified version of (3.4) and use it to estimate a_{LA} = 0.xxxx (round off to 4 decimal places) To find a_{LA} use surface T_G = 288K (a rough average of data in fig 3.20 at 38N) and the I_{IN} =1368 W/m^2.
b. Find I_A
c. Find T_A
d. What range of pressure levels in both seasons shown in fig. 3.20 correspond to the T_A you found?
e. Repeat steps a-d with latent and sensible heat fluxes appropriate for 38N: SSHF=27 W/m^2 (both seasons) and SLHF=75 W/m^2 (DJF), 60 W/m^2 (JJA)

7. Derive the Stefan-Boltzmann law (D.11) from Planck's law (D.5).

8. Cloudy versus clear sky in the glass slab model.
a. Starting with A_{lbd_c}=0.8 and A_{lbd_nc}=0.1, a_{L1}=0.85, and solar constant spread over the Earth I_S=341, use the two layer glass slab model to show that the ground temperature T_G decreases as T_2 becomes colder when the nonzero cloud fraction is < ~0.46 as discussed in regards to (3.48).
b. How does this threshold in cloud fraction change if clouds become thicker? (A_{lbd_c}=0.8, a_{L1}=0.85) How do the layer and ground temperatures change at the threshold?

9. Tropopause estimates from the RCE model.
a. Calculate the T values every 0.2 km assuming a constant lapse rate (6 K/km) starting from a surface temperature of 278K. At what level z does the I_{FC} (emitted from the atmosphere at level z) equal one half of the absorbed solar radiation reaching the ground? (i.e. where I_{FC} =0.35*I_S and with I_S=1366 W/m^2) Calculate I_{FC} from the Stefan-Boltzmann law assuming a gray body a_{LA}=0.9 . Note that T_G that equals the surface air temperature T_A at z=0km.
b. How does that level compare with the observed tropopause?
c. Using Figure 3.20, find the approximate latitude where the air temperature at this 'tropopause' level equals the observed Southern Hemisphere temperature at this level in winter (JJA)?

10. Trivial estimates of temperature change from the glass slab model. Use equations (3.9) and (3.10) to answer the following questions.
a. Reproduce the temperatures T_G and T_A in the text by assuming a_{SA}=0.33, a_{LA}=0.9, I_{IN}=239 W/m^2 and solving both for no surface fluxes and for SSHF=17 and SSLH=80 W/m^2.
b. Repeat part a by assuming that the longwave absorptivity and both heat fluxes increase by 5%. How much have T_G and T_A changed from part a?
c. The maximum that a_{LA} can be is 1.0. Substitute that into your formula for T_G to find the maximum value for the given parameters. Describe how the real atmosphere can have higher temperatures due to additional absorber than implied by this single slab model.

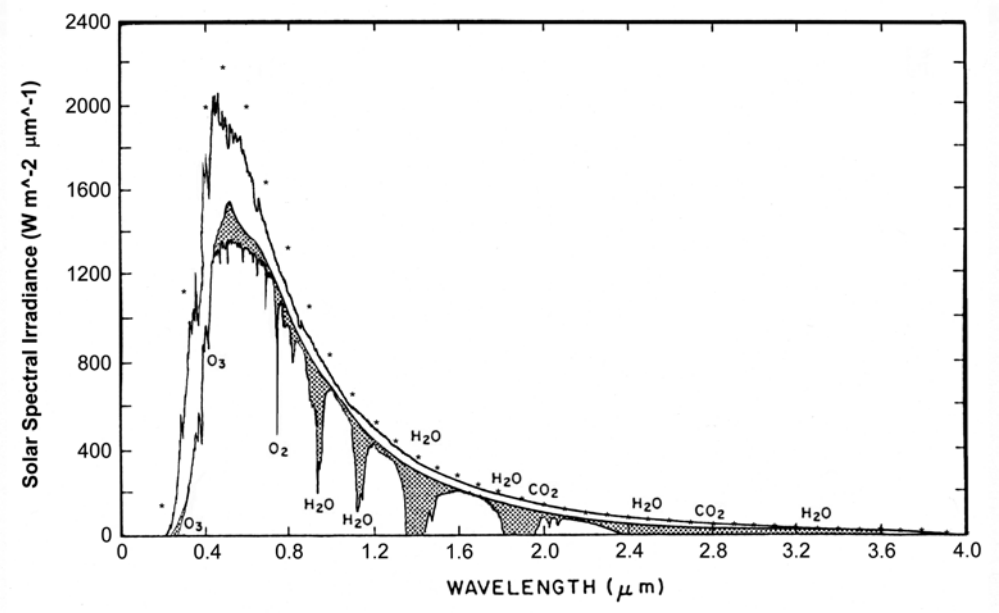

Figure 3.1 Solar spectral irradiance (shortwave radiation) where the upper curve is TOA downward solar, lower curve downward solar at the Earth's surface, shaded area is atmospheric absorption of solar radiation, molecular labels indicate the atmospheric constituents primarily responsible for the atmospheric absorption at those wavelengths. The gap between the top curve and the top of the shaded area is solar radiation that is reflected or scattered without absorption. Top of atmosphere (TOA) and surface spectrum values based on data provided by R. Rohde (2007; http://www.globalwarmingart.com/wiki/File:Solar_Spectrum_png). Shaded area estimates the terrestrial absorption based on Thekaekara (1976). Asterisks are point values for spectral irradiance at the Earth's orbit if the sun were a 5620K black body.

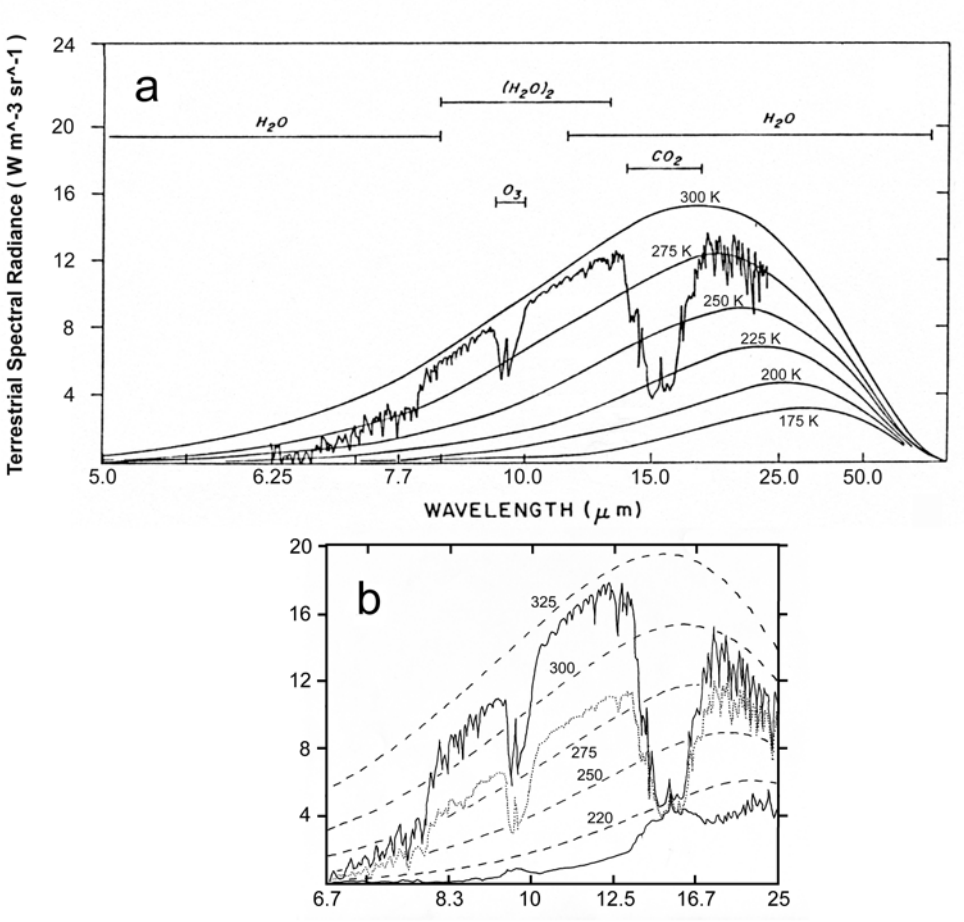

Fig 3.2 Terrestrial spectral radiance (a) for a region of the subtropical Pacific measured by a polar orbiting satellite as it passed over Guam. (b) Same scale but for the Sahara (top solid line), Mediterranean (dotted), and Antarctica (lower solid line). Dashed lines are blackbody radiances for the indicated temperature labels in K. The panels are redrawn from data in Liou (1980) and in Thomas and Stamnes (1999). The abscissa is equally-spaced in wavenumber, but stretched in wavelength.

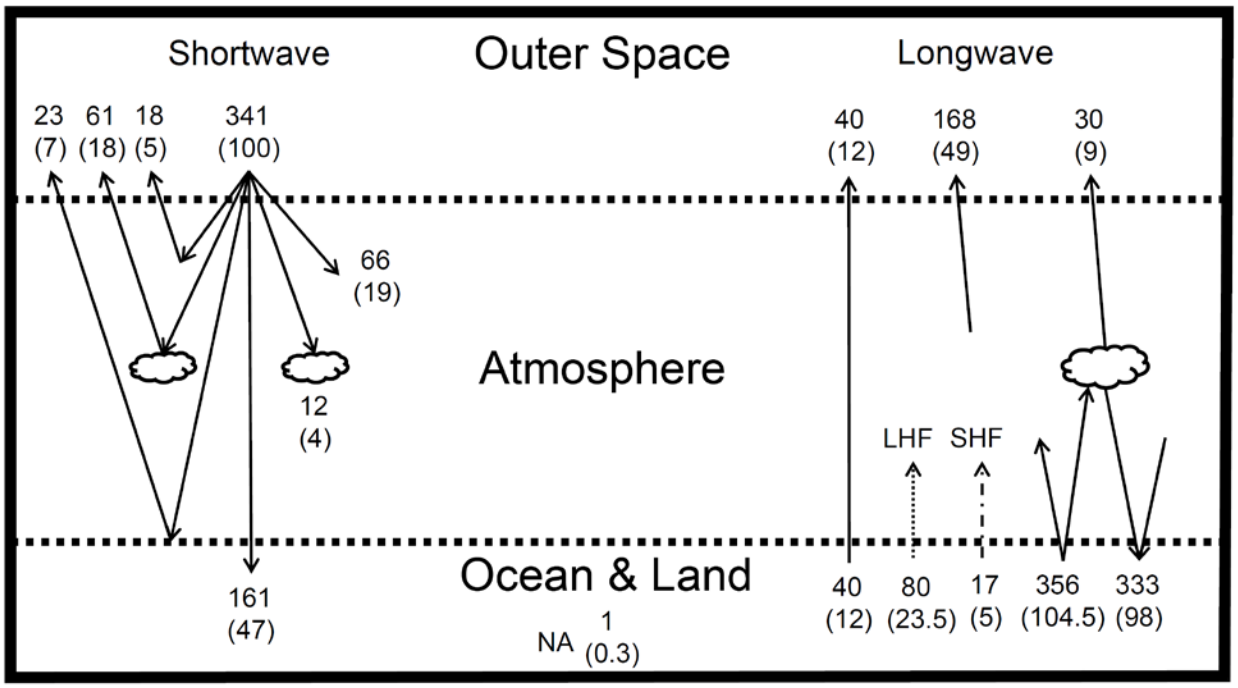

Figure 3.3 Estimates of major components of the global energy balance based upon data in Trenberth et al. (2009) with adjustments in Grotjahn (1993). Two numbers are presented, with the top number in units of W/m^2 while the number in parentheses is the corresponding percentage of the incoming radiation. Abbreviations: LHF is latent heat flux from the Earth's surface; SHF is sensible heat flux from the Earth's surface; NA is net absorption by the Earth system (ocean, land, atmosphere) as estimated by Hansen et al. (2005).

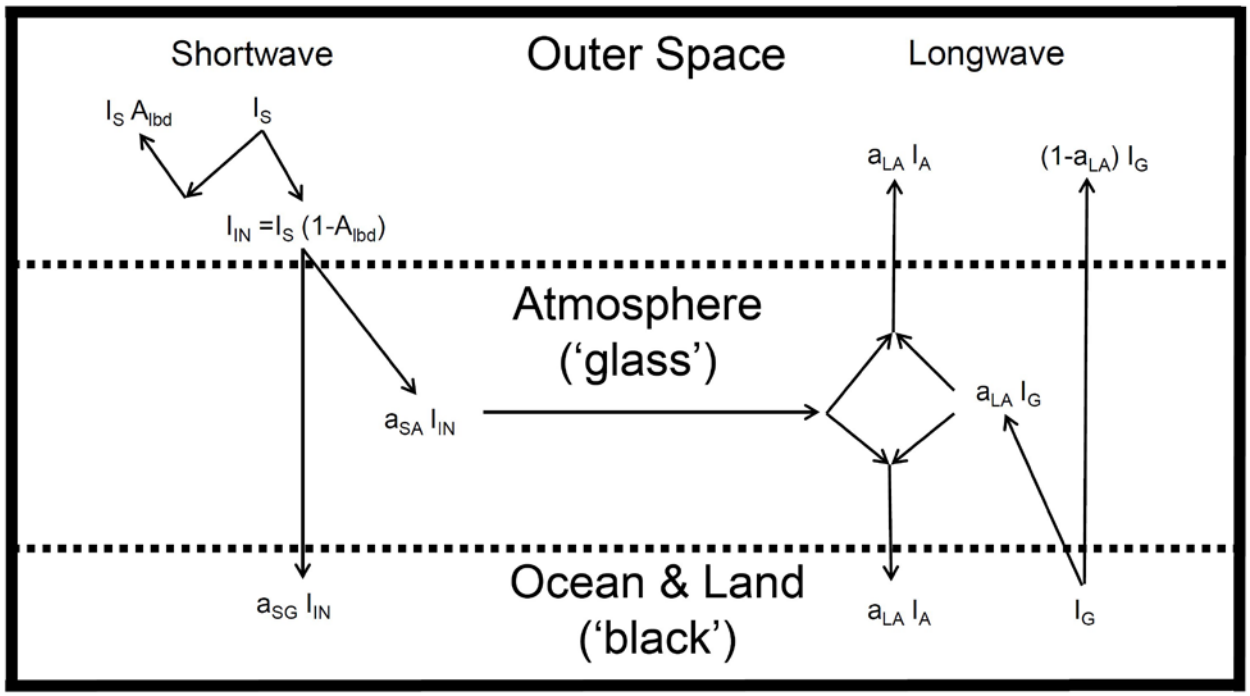

Figure 3.4 Parameters for the 'glass slab' model of radiative balance for the global atmosphere. The model is in balance since the energy passing upwards and downwards cancels for all three domains.-Using data in figure 3.3, the atmospheric longwave absorptivity, a_{LA} = 356/(356+40) = =0.9. The solid arrows show radiant energy where the atmosphere is just a single layer, labeled 'glass' since no horizontal or vertical motions are allowed to redistribute heat. To determine the atmospheric temperature, sum up all the emission values and apply the Stefan-Boltzmann law. Similarly, to determine the Earth's surface temperature, all the emission values (upward pointing arrows only at the surface) are summed.

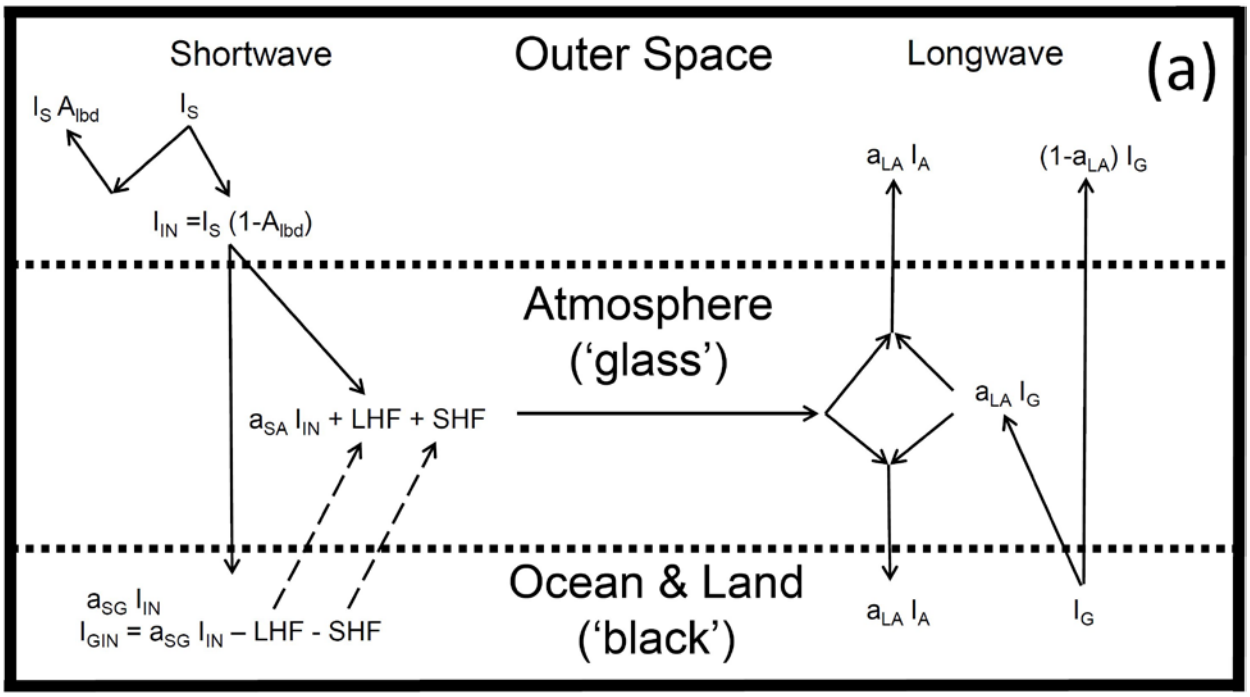

Fig. 3.5 Elaborations of the glass slab model a) adding surface heat fluxes to the glass slab model. The effect of the surface heat fluxes is to cool the Earth (decrease I_{G1}) and warm the atmosphere (increase I_{A0}). b) subdividing the glass slab into two separate slabs

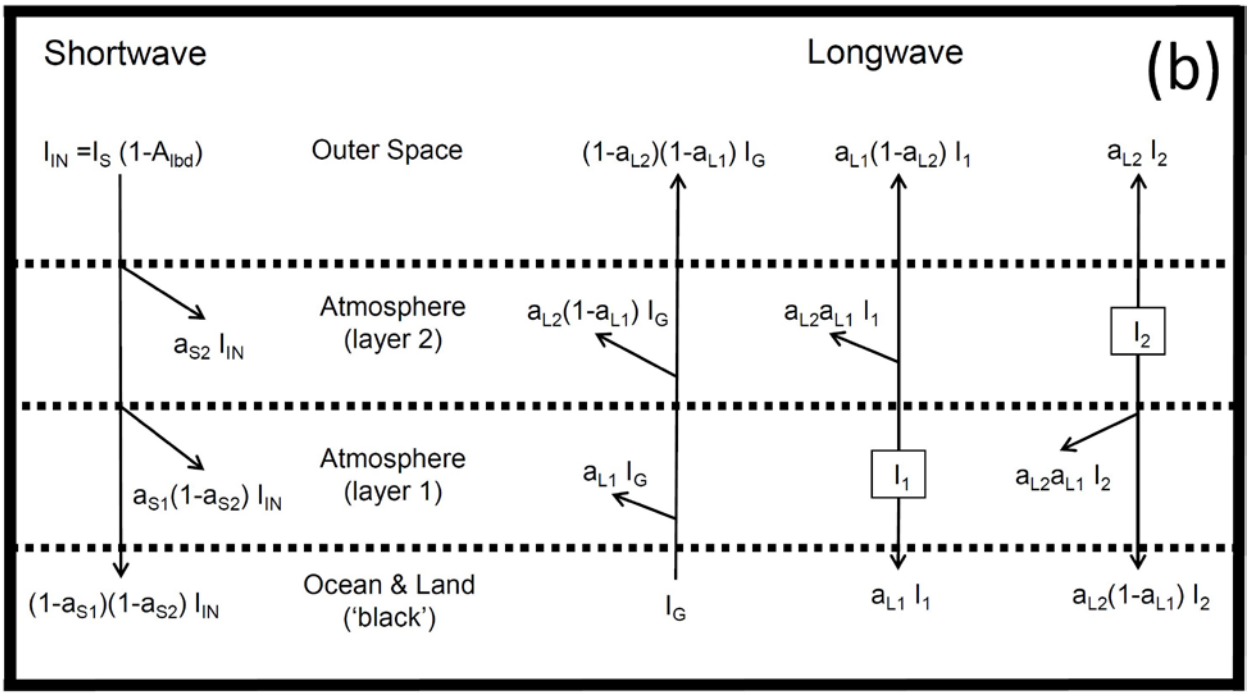
Shortwave
Longwave
(b)
$I_{IN} = I_S (1-A_{lbd})$
Outer Space
$(1-a_{L2})(1-a_{L1}) I_G$
$a_{L1}(1-a_{L2}) I_1$
$a_{L2} I_2$
Atmosphere
(layer 2)
$a_{L2}(1-a_{L1}) I_G$
$a_{L2}a_{L1} I_1$
$a_{S2} I_{IN}$
I_2
Atmosphere
(layer 1)
$a_{L1} I_G$
I_1
$a_{L2}a_{L1} I_2$
$a_{S1}(1-a_{S2}) I_{IN}$
Ocean & Land
('black')
$(1-a_{S1})(1-a_{S2}) I_{IN}$
I_G
$a_{L1} I_1$
$a_{L2}(1-a_{L1}) I_2$

Figure 3.5b

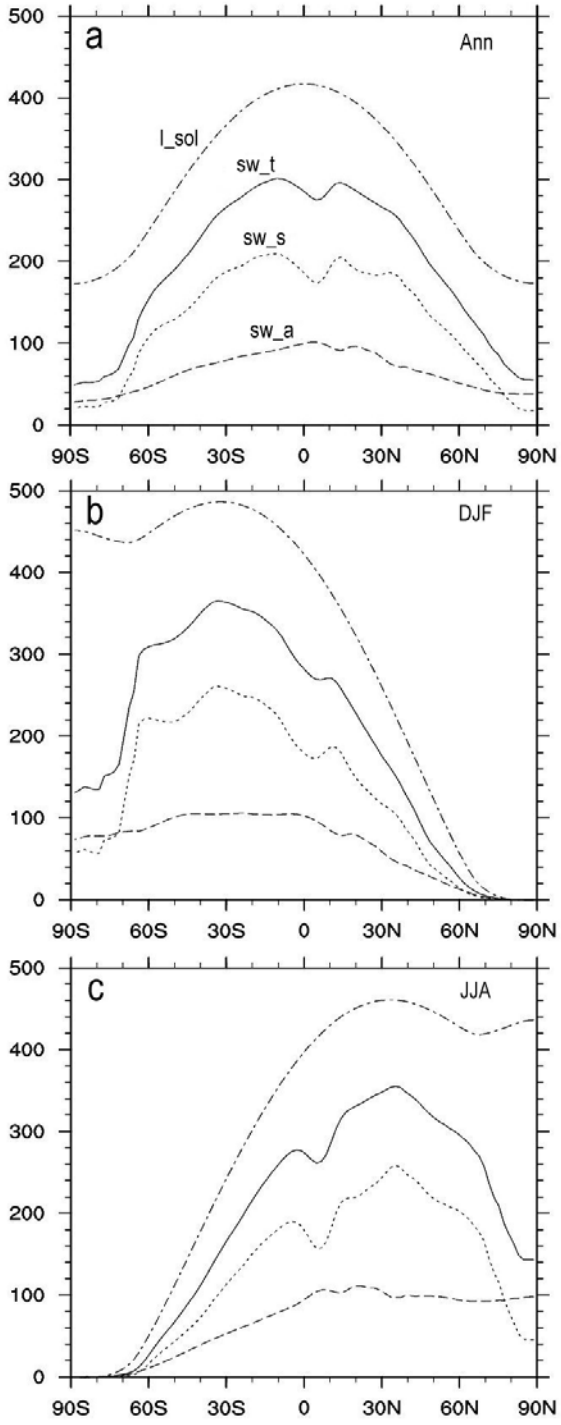

Fig. 3.6. Solar radiation components: I_sol is incident short wave (SW) radiation at the top of the atmosphere (TOA). SW_t is the total absorbed SW radiation; SW_s is the total absorbed SW at the Earth's surface; SW_a is the total absorbed sw radiation by the atmosphere. Panels: a) annual average, b) December-February, c) June-August of NDRA2 data during 1979-2014. Relative differences in the absorbed amounts should be emphasized as the numerical values of these data have differences with other reanalyses (e.g. Grotjahn, 2008).

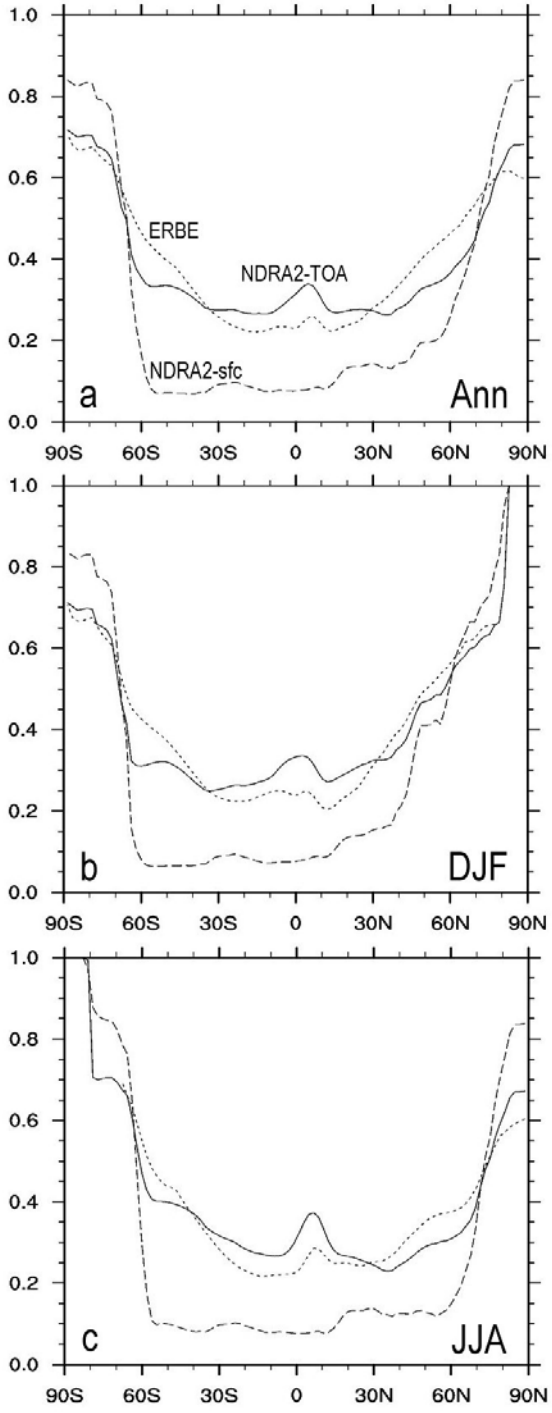

Fig. 3.7 Albedo (A_{lbd}) estimates from ERBE (dotted) data, from NDRA2 data at the TOA (solid), and from NDRA2 surface data (dashed). There are notable differences between the ERBE and NDRA2 data at most tropical and middle latitudes.

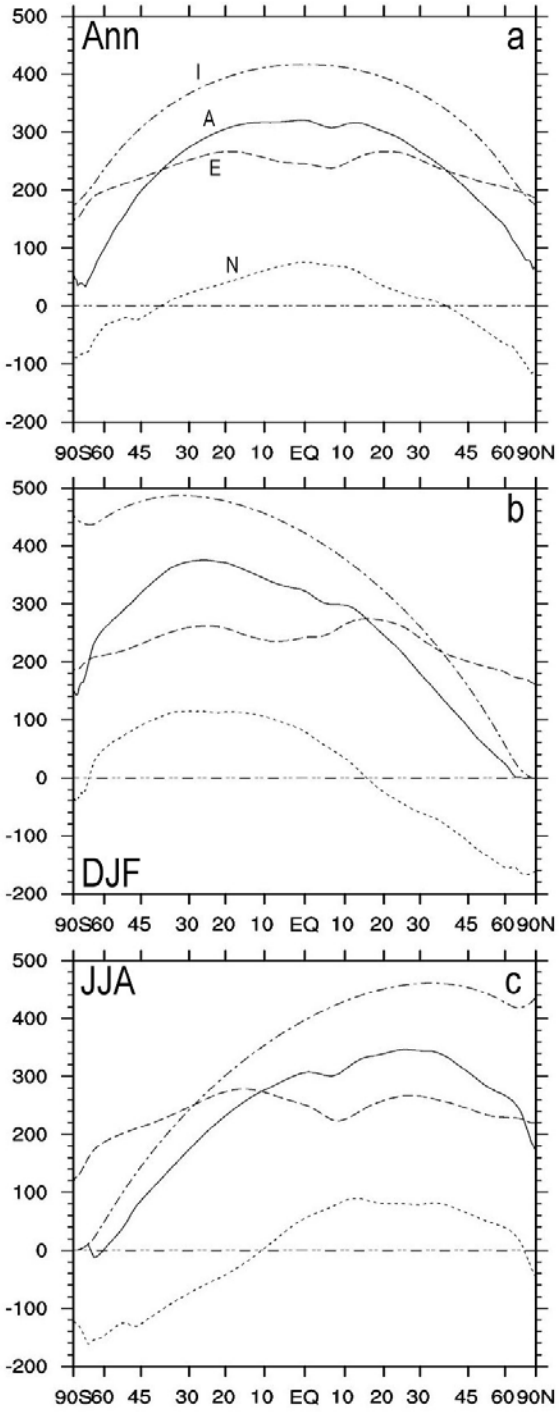

Fig. 3.8 Summary of zonal average energy balance for annual (a), December-February (b), and June-August (c) data. Shown are: incoming solar radiation at TOA (I, dot dashed), NDRA2 absorbed (A, solid) and emitted from TOA (E, dashed) and ERBE net radiation (N, dotted).

Use I_sol, sw_t, lw_t, and nr_t for the labels in this figure.

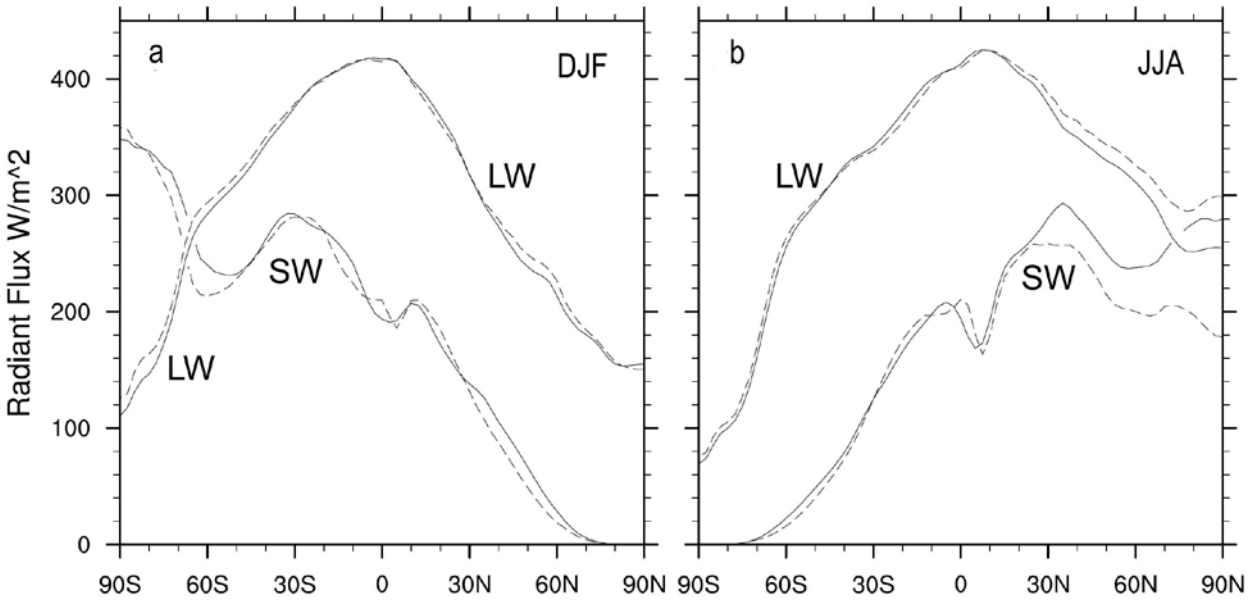

Fig. 3.9 Downward shortwave and longwave radiative fluxes at the Earth's surface, zonally averaged, for the two extreme seasons. Solid is NDRA2 while dashed is ERA-40. Net downward shortwave radiative flux (labeled sw) at the Earth's surface during a) December-February (DJF, left column) and b) June-August (JJA, right column). Corresponding longwave radiative fluxes (labeled lw) in a) DJF and b) JJA. Notable differences exist in polar summer regions. Panels redrawn from Grotjahn (2008).

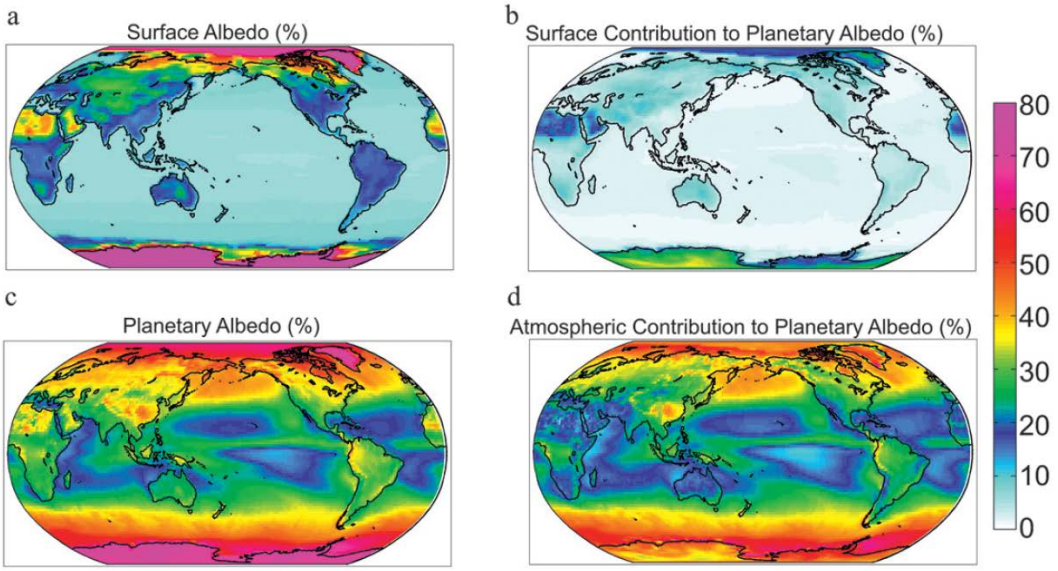

FIG. 2. (a) Surface and (c) planetary albedo, and (b) surface and (d) atmospheric contributions to (c). All quantities are expressed as a percentage, where 1% corresponds to 0.01 units of albedo.

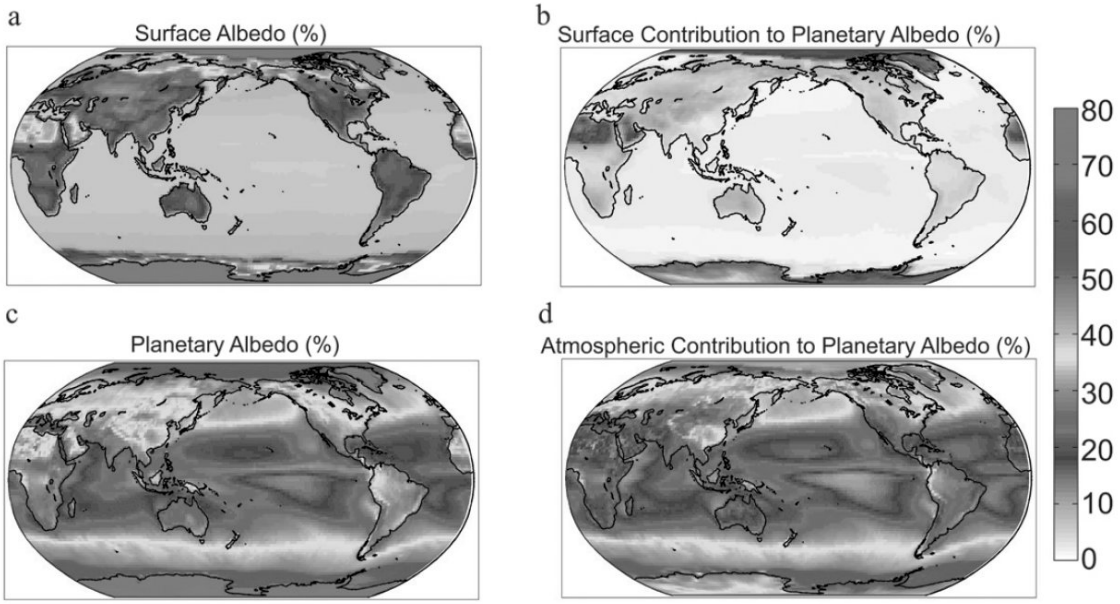

FIG. 2. (a) Surface and (c) planetary albedo, and (b) surface and (d) atmospheric contributions to (c). All quantities are expressed as a percentage, where 1% corresponds to 0.01 units of albedo.

Figure 3.10 Based on Terra data from 2000-2005 and Aqua data from 2002-2005. The bright band in middle latitudes is around 35-40 percent. The contributions (panels b and d) are additive and sum to the total planetary albedo (panel c). Reproduced from Donohoe and Battisti (2011).

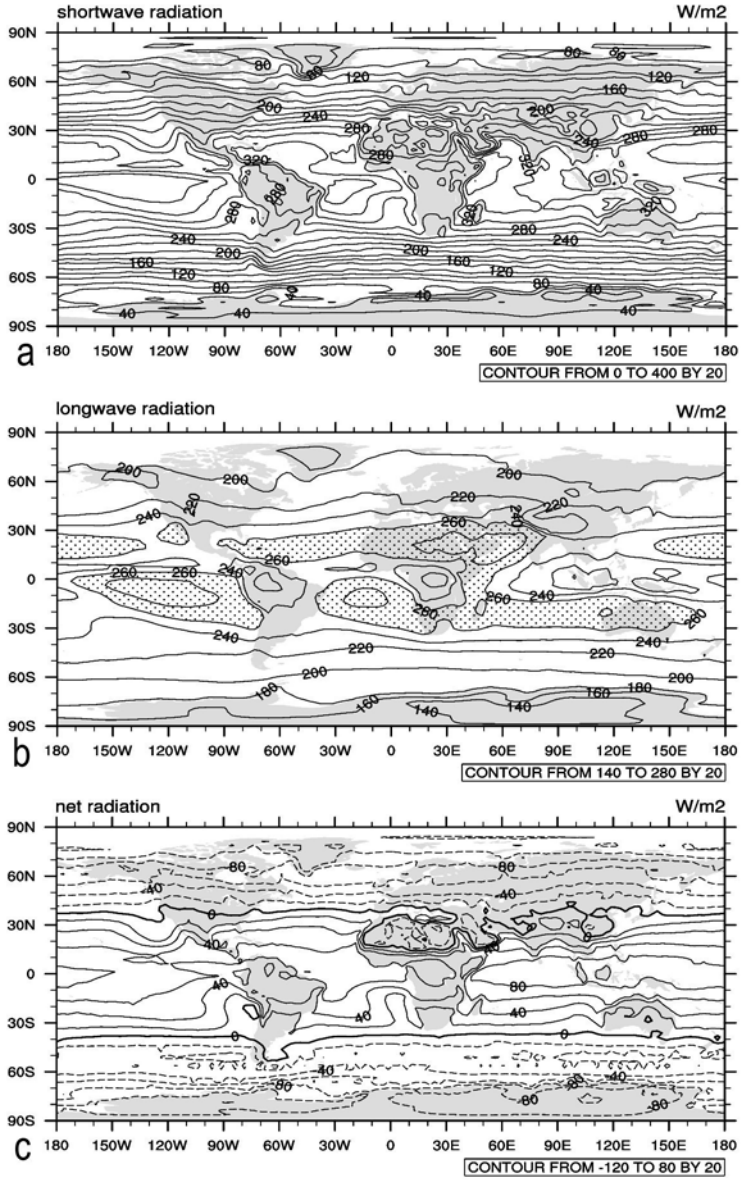

Figure 3.11 Annual radiation budget at the top of the atmosphere showing horizontal variation of the components. a. Absorbed solar radiation (sw) for the atmosphere and earth. b. Terrestrial longwave emission (lw) at TOA, with values greater than 260 W/m^2 stippled. c. Net radiation (sw – lw) at TOA with negative values dashed and zero line bold.

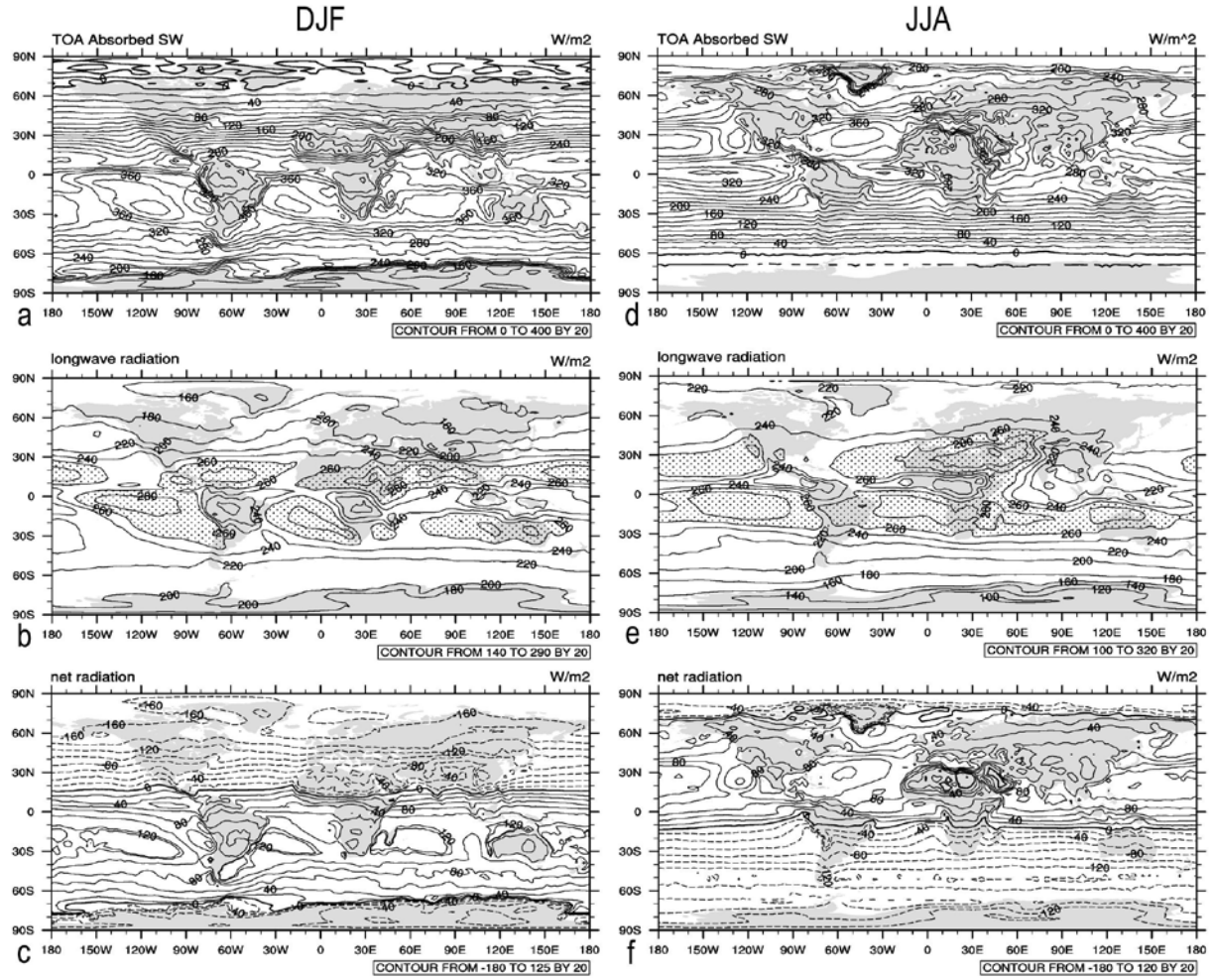

Figure 3.12 Seasonal patterns of TOA radiation components. Negative values are dashed and the zero line is bold.

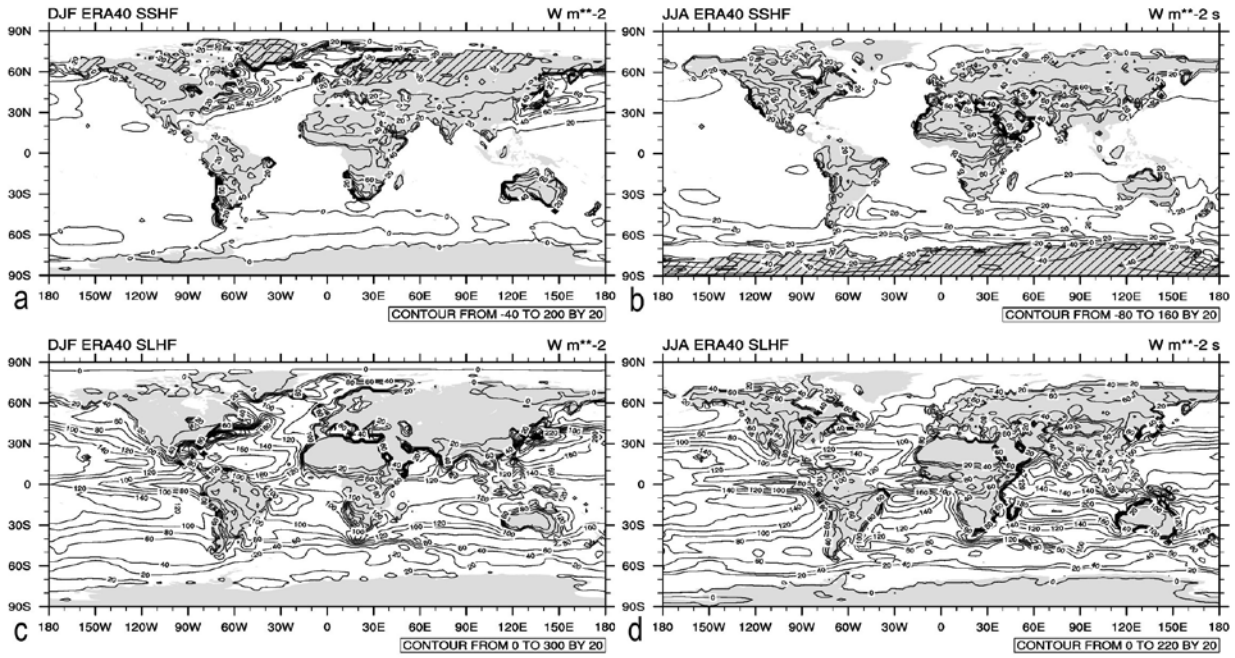

Figure 3.13. Surface sensible heat flux (top row) and surface latent heat flux (bottom row) during DJF (left column) and JJA (right column).

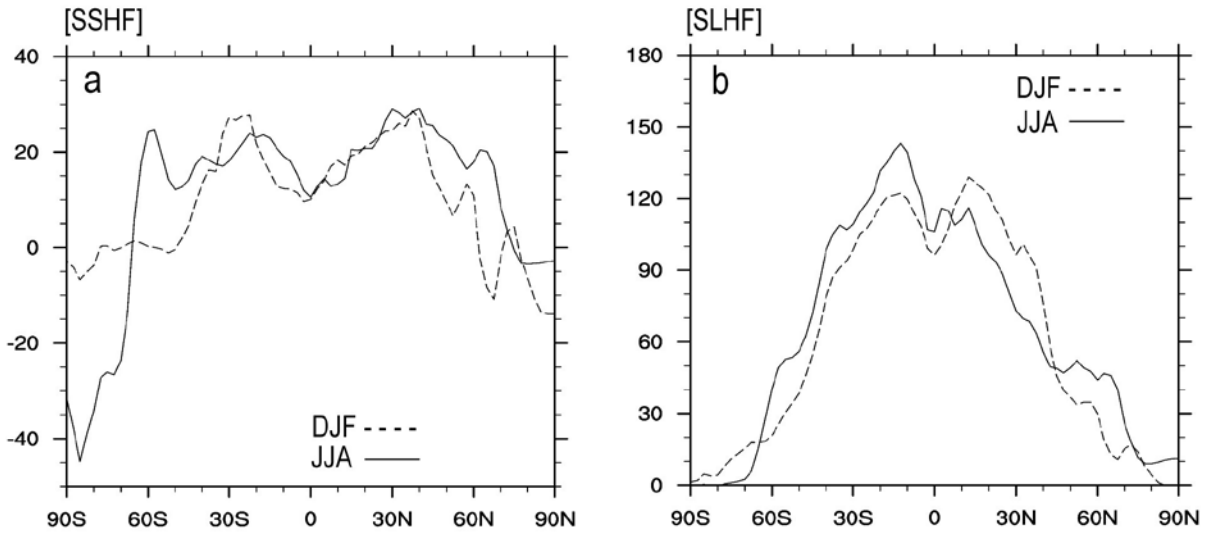

Figure 3.14. Zonal average: surface sensible heat flux (left) and surface latent heat flux (right) during DJF (dashed lines) and JJA (solid lines). Note that the scale of SLHF is twice that of SSHF. ERA-40 data

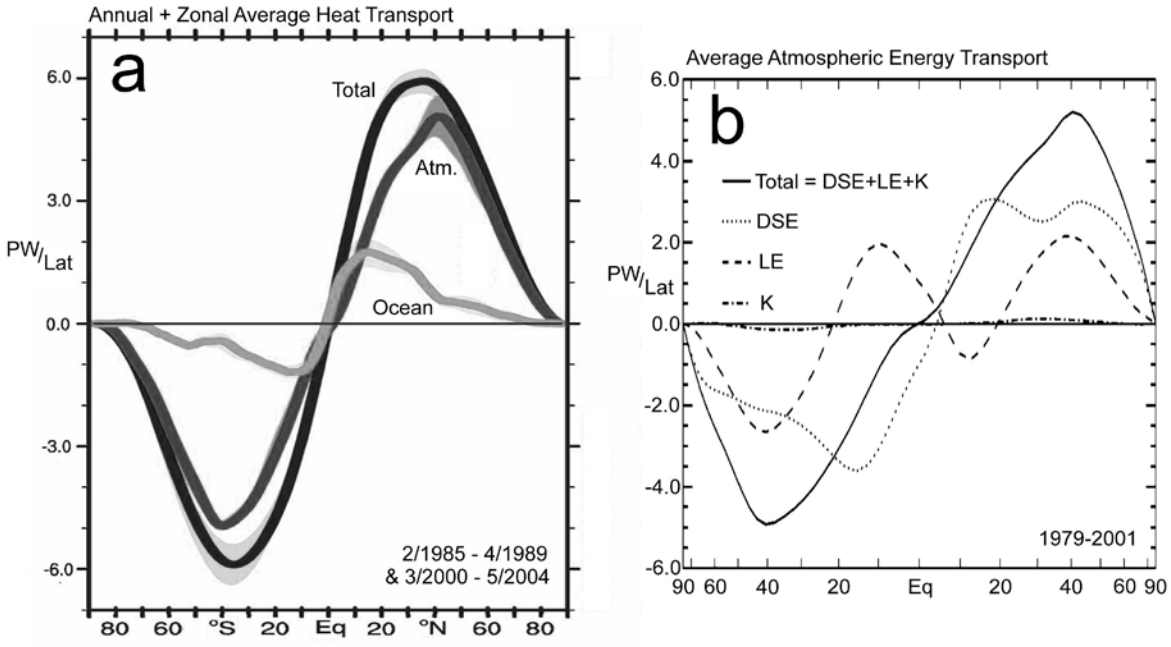

Figure 3.15. Annual and zonal average horizontal heat fluxes. a) Total, atmospheric, and oceanic heat fluxes expressed as PW within a 1 degree latitude band, based on two satellite observing periods redrawn and from Fasullo and Trenberth (2008b). Shading indicates ±2 standard deviations of interannual values. b) Atmospheric transport split into sensible (DSE) and latent heat fluxes as well as flux of kinetic energy, K, based on reanalysis data and redrawn from Trenberth and Stepaniak (2003a). Note the latitude scaling based on equal surface areas in b).

Color version available:

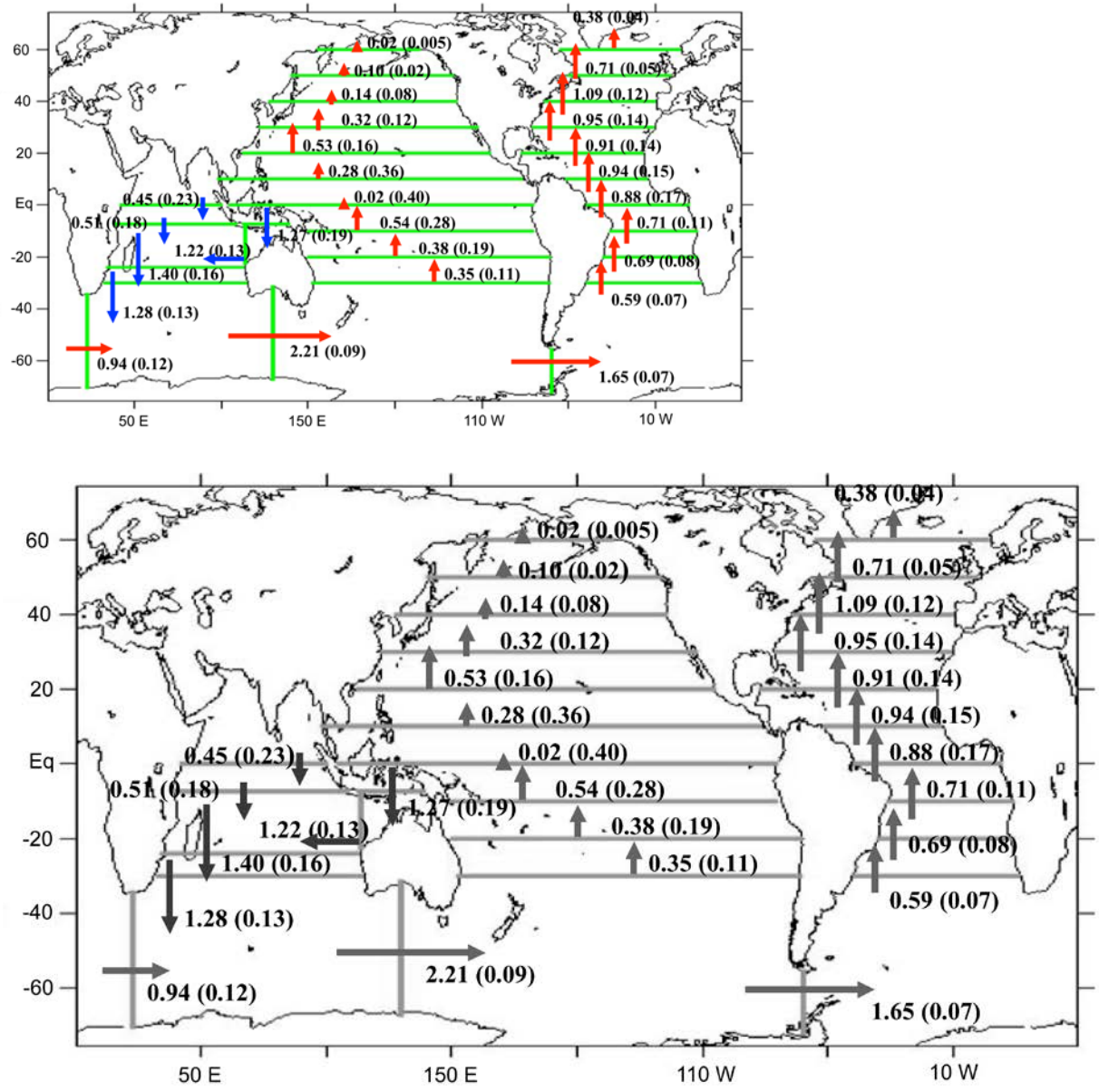

Figure 3.16. Time and horizontal average heat fluxes across indicated ocean transects estimated from 1958-2004 data. Standard deviation are included in parentheses. PW unit. Figure reproduced from Zheng and Giese (2009).

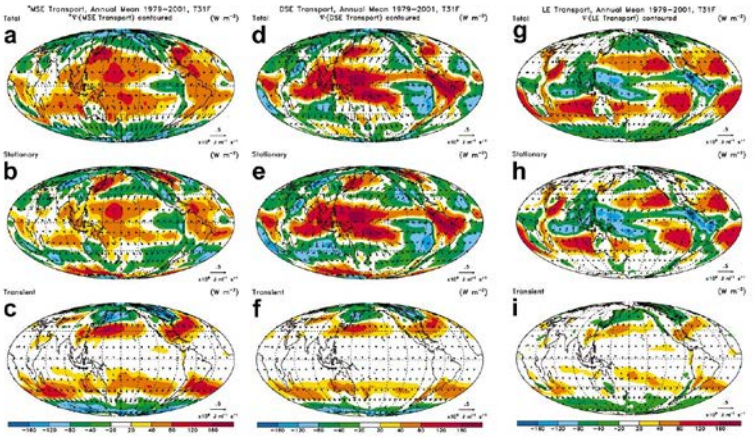

Color version is available

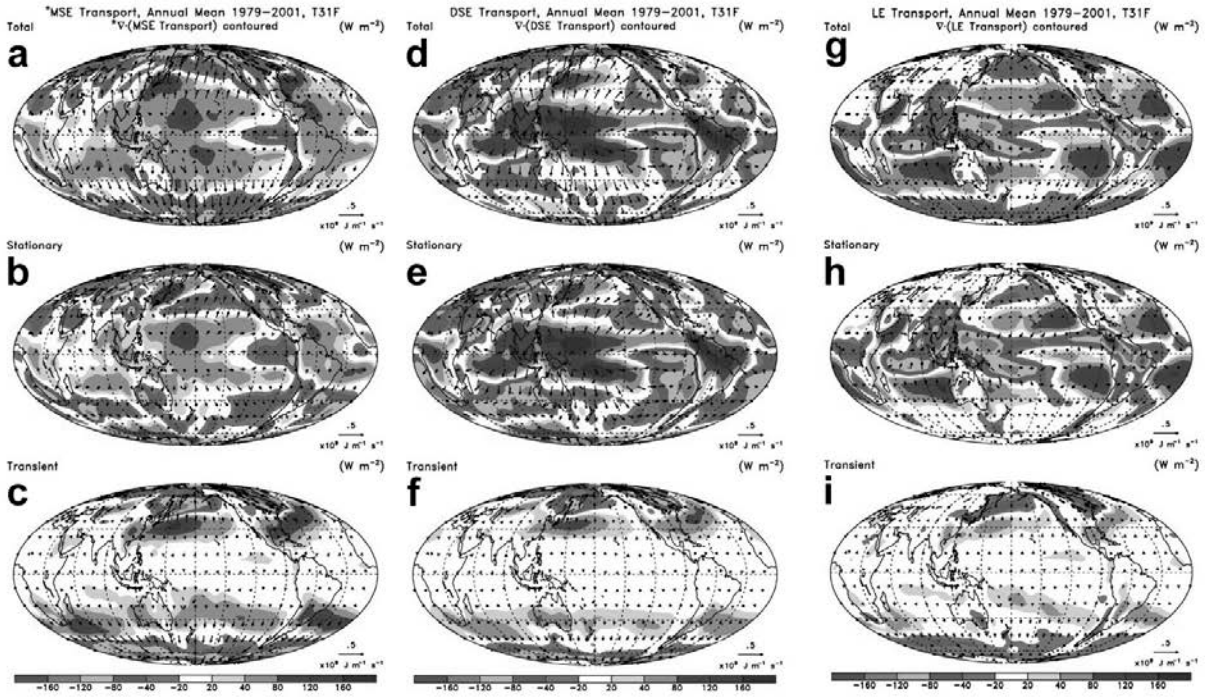

Figure 3.17. Annual average heat transport expressed as energy fluxes (arrows) and heating rates (contours). Shaded contour interval is the same in all figures; positive values increase as shading becomes progressively darker while increasing negative values start with dark and become lighter shading. a)-c) Total energy with the asterisk to indicate that it approximately equals MSE; d)-f) DSE component of MSE, and g)-i) the LE component of MSE. The top row are total values; the middle row shows contributions from quasi-stationary fields; the bottom row are transient (sub-monthly) fields. Reproduced from Trenberth and Stepaniak (2003b).

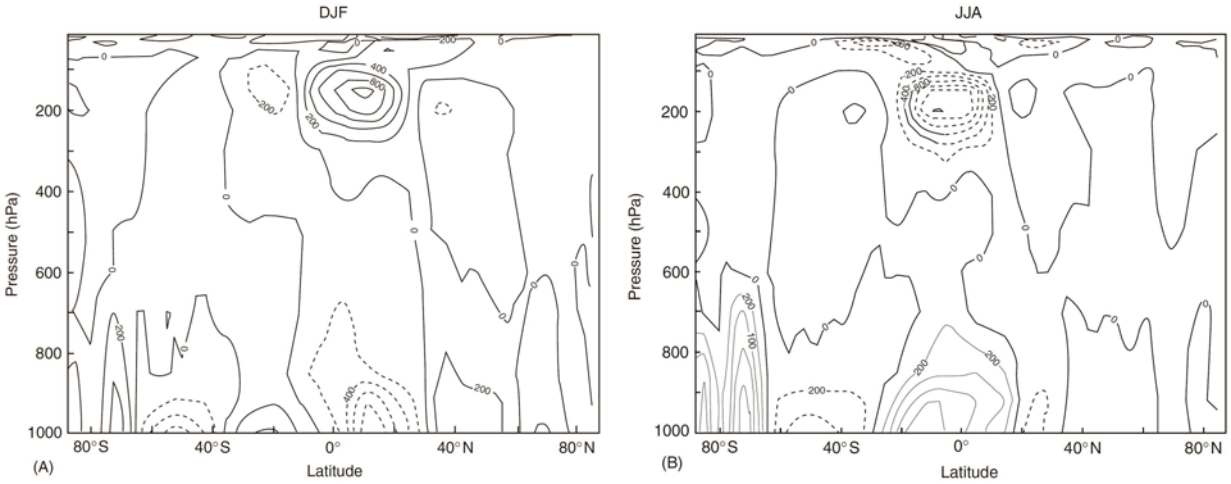

Figure 3.18. Zonal average heat flux defined as [vθ]. Includes transient and stationary (seasonally) and zonal mean and eddy contributions. (Reproduced from Grotjahn, 2015b)

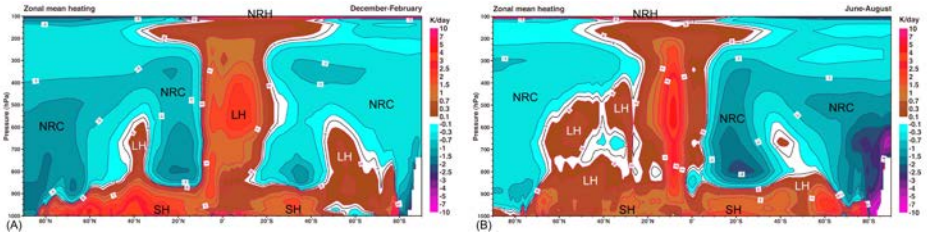

Color version available.

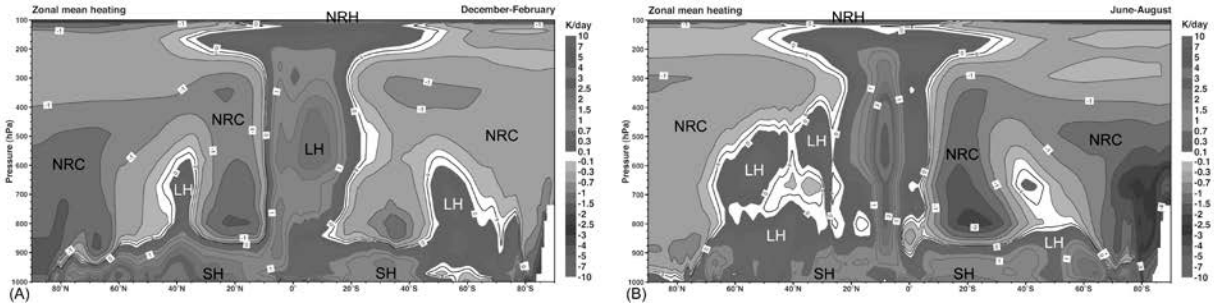

Figure 3.19. Zonal mean heating calculated as a residual in the temperature conservation equation. Areas near zero have no shading. Areas where shading darkens as values become larger in magnitude are negative values (cooling, 'blue' if in color). Areas where shading becomes lighter as values become larger are positive (heating, 'warm colors' if in color). Labels indicate the processes that tend to be larger in given regions. NRC indicates net radiative cooling, NRH means net radiative heating, LH indicates latent heating, SH indicates surface sensible heat flux mixed upward in the boundary layer. Units are Kelvin per day. Reproduced from Kållberg, et al., (2005).

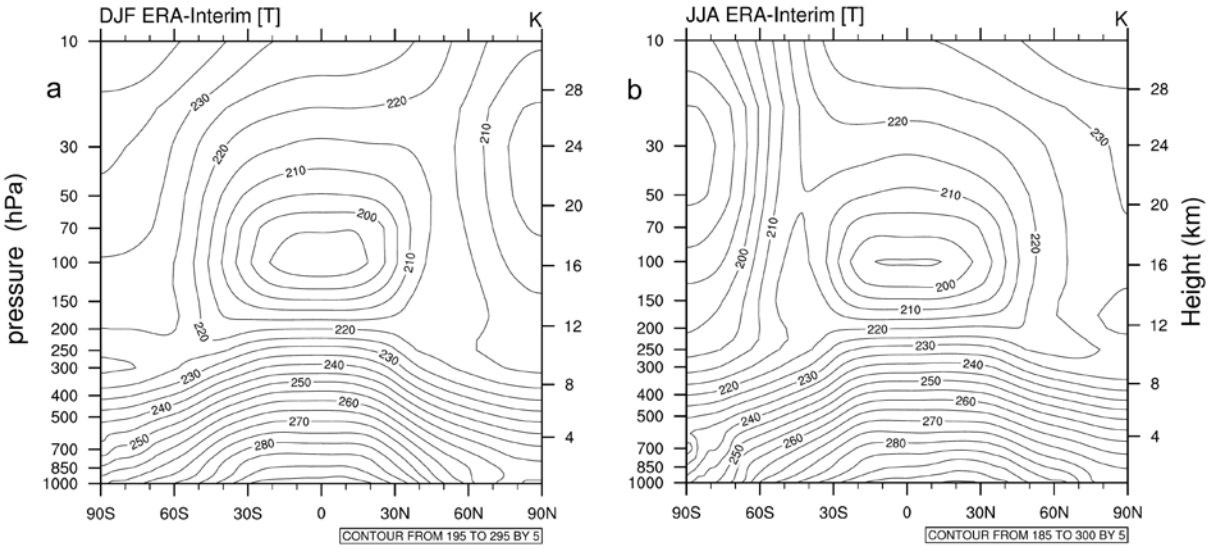

Figure 3.20. Zonal and time averages of seasonal mean T. ERA-Interim data used from 1979-2017. The contour interval is 5K.

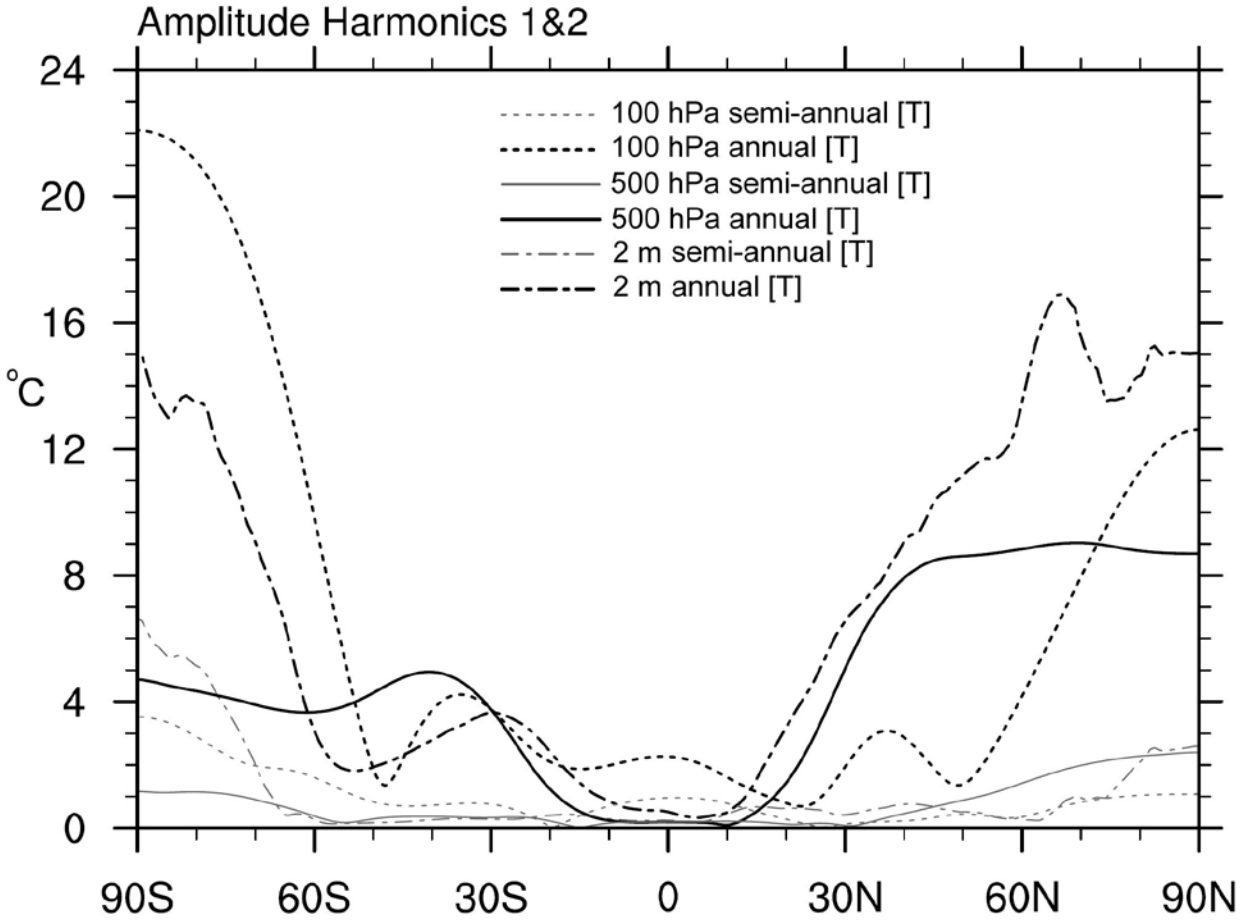

Figure 3.21 – The latitudinal variation of the annual and semi-annual cycles of [T]. Amplitudes shown at three levels: 2 m above surface and 500 and 100 hPa. Darker curves are used for the annual cycle, lighter curves are for the semi-annual cycle and are always less than the annual.

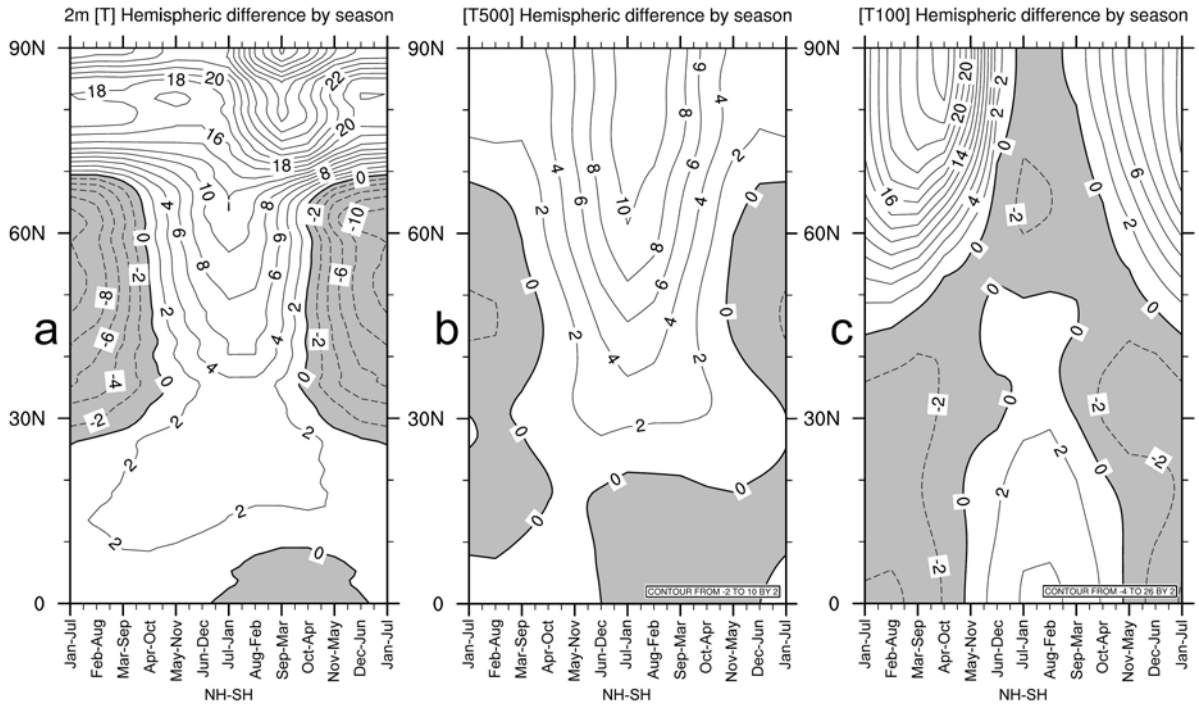

Figure 3.22. Interhemispheric differences at three levels: a) 2m above the surface, b) 500 hPa, and c) 100 hPa. Similar seasons in each hemisphere are differenced. The left and right edges of each plot have Southern Hemisphere July values subtracted from Northern Hemisphere January values and hence compare local ‘winter’ or ‘cool season’. The middle of each plot is northern July minus southern January, or local ‘summer’ or ‘warm season’. ERA-Interim data from 1979-2017 shown.

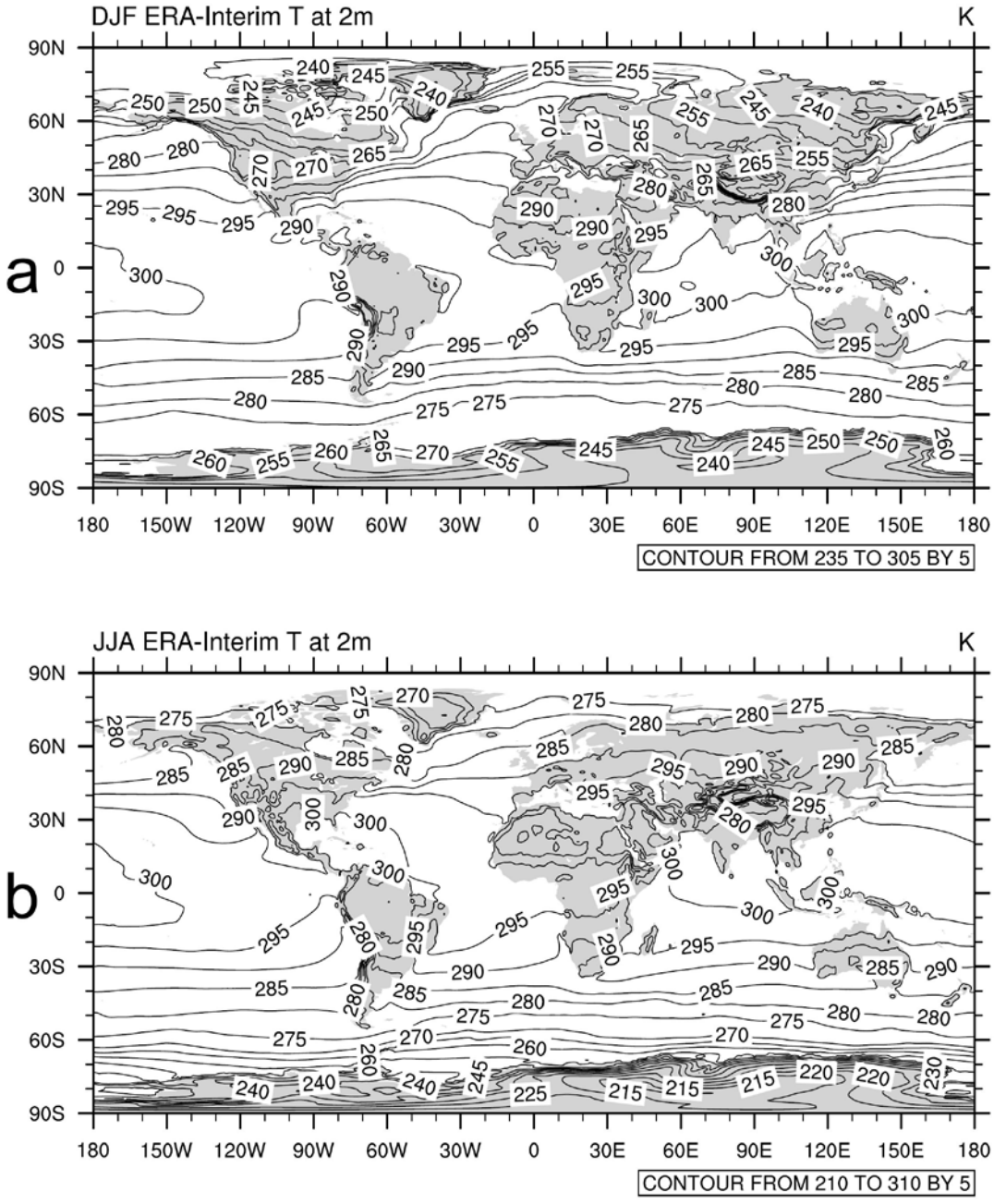

Figure 3.23. Seasonal mean temperature at 2m above the surface. a) December-February, b) June-August values. ERA-Interim data from 1979-2017 using 5K contour interval.

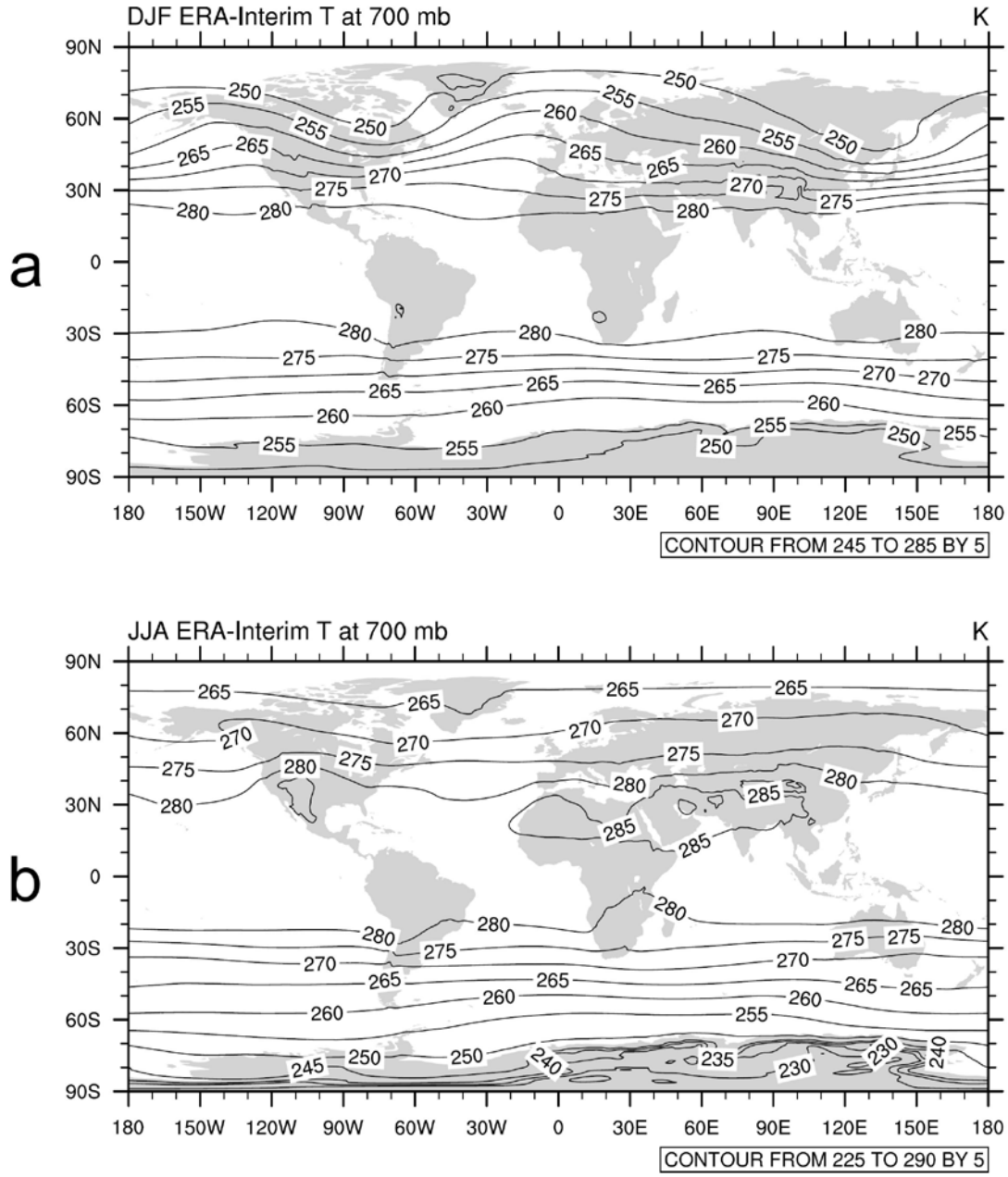

Figure 3.24. Seasonal mean temperature at 700 hPa, indicative of middle troposphere temperature patterns. a) December-February, b) June-August values. ERA-Interim data from 1979-2017 using 5K contour interval.

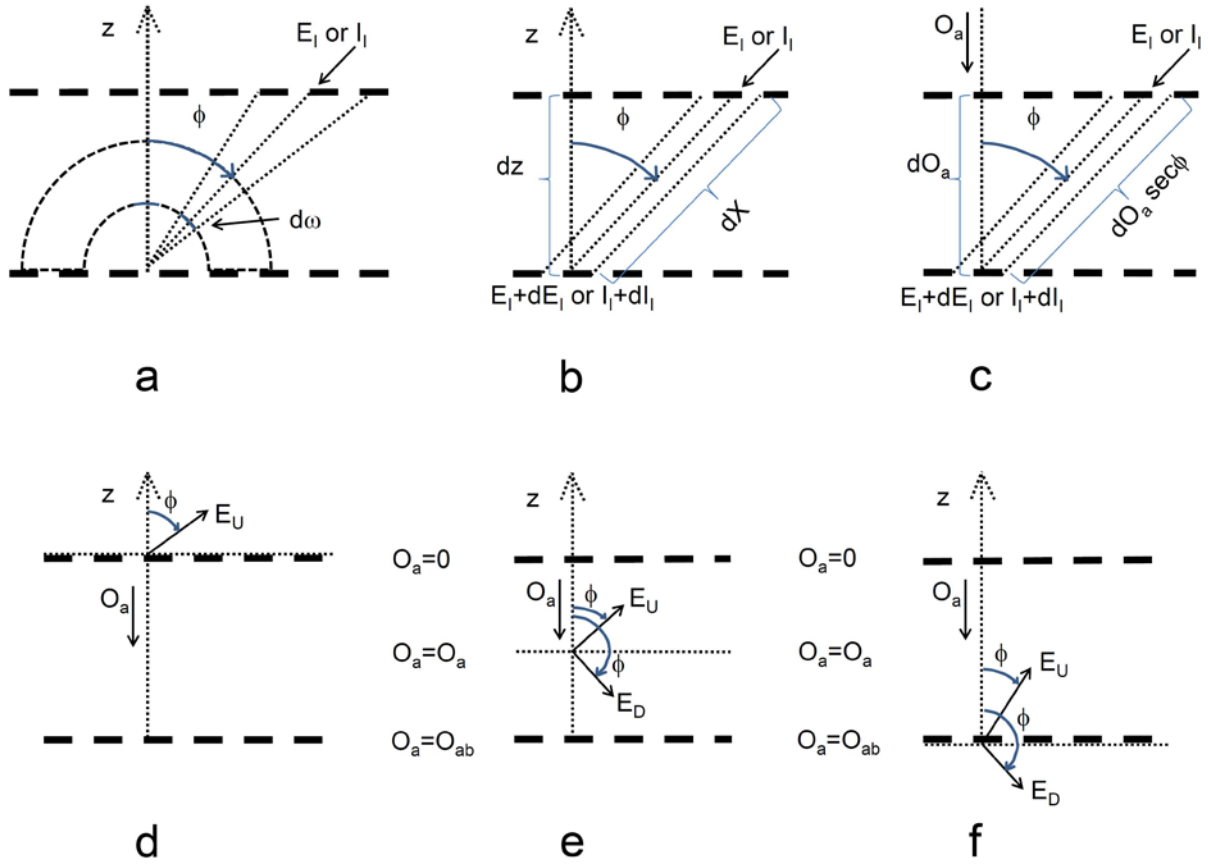

Figure 3.25. Geometry and notation used by the radiative-equilibrium and radiative-convective models.

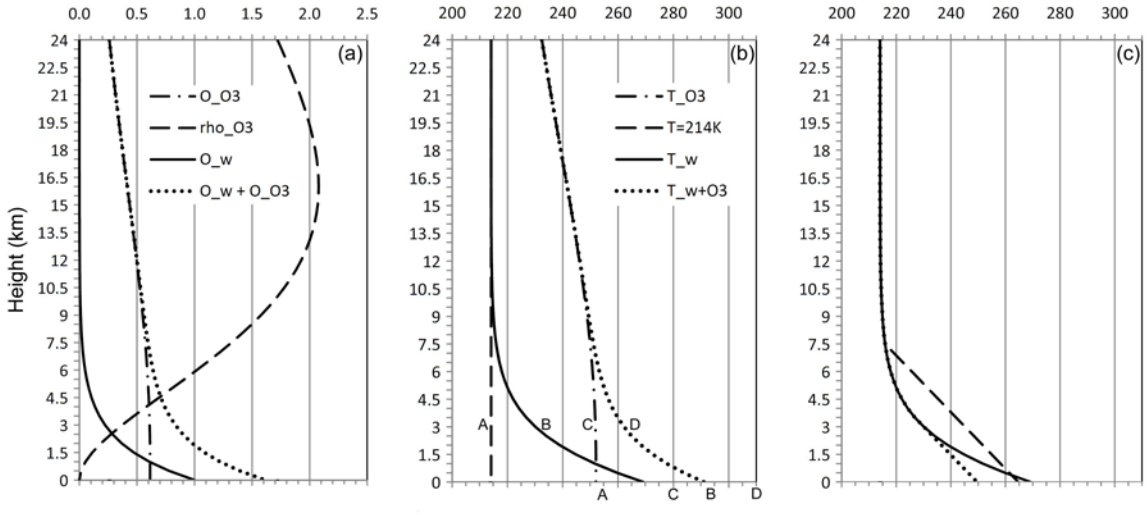

Figure 3.26. Simulated absorber profiles, resultant radiative equilibrium temperature profiles. (a) optical depths as a function of elevation used for water vapor (solid line), ozone (dot-dashed line), and the sum of those two optical depths. Also shown, the density of ozone (dashed line; values multiplied by 100). (b) Corresponding temperature profiles for the optical depths shown in (a) with the exception of the line labelled 'A' which is the skin temperature (T_{sa}) and assumes there is no atmospheric absorption in the sense to create emission downward. Each labelled curve has a corresponding letter below the bottom axis showing the temperature at the surface, T_G which is discontinuous with the temperature at the bottom of the atmosphere. (c) The temperature due to the water vapor optical depth (solid line, same as in (b)) with superadiabatic lapse rates removed assuming a 6.5 K/km maximum lapse rate. The dotted line is for levels where $T_A(z)$ is superadiabatic but still leaves the discontinuity at z=0; the dashed line distributes the temperature in a way that removes the discontinuity and distributes the heating vertically. I_F=952.2 W m^{-2}, A_{bld} =0.31, H_w =2 km, b= -0.125 km^{-1} , k_{O3} B=6x10^{-4} km^{-3} (z is in km), O_{ab}=1.

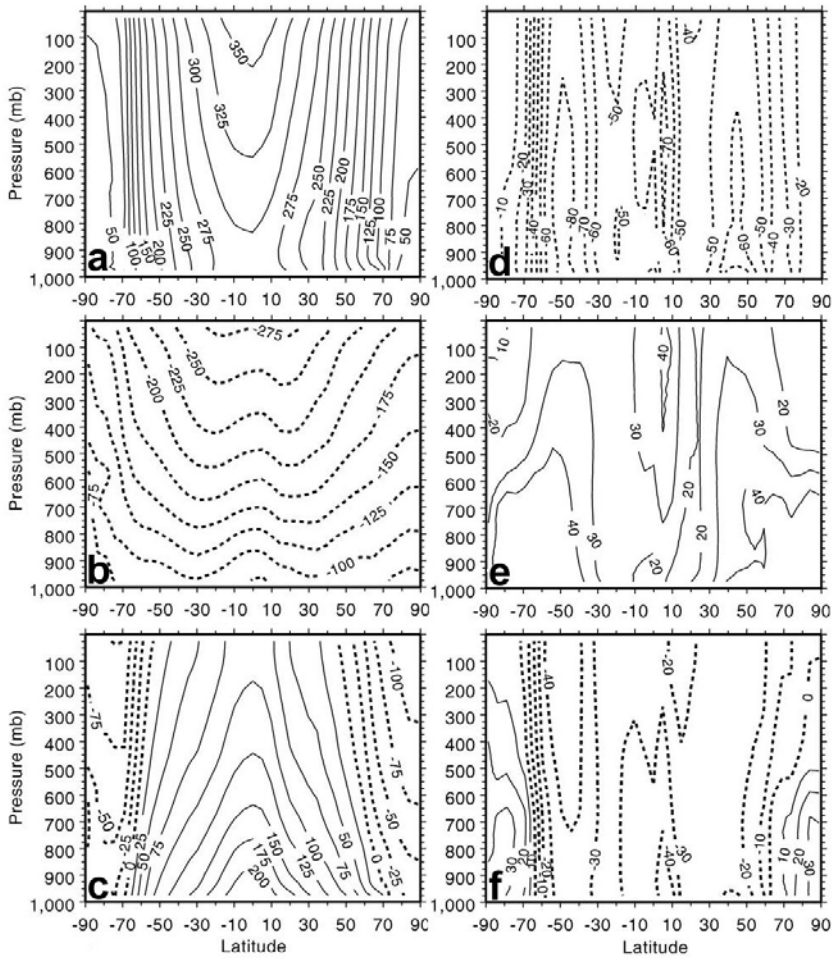

Figure 3.27. Radiant energy (W/m^2) gain below the indicated level as interpolated from four layers. (a) Solar radiation, showing decreasing values with elevation due to atmospheric absorption (especially by water vapor in the tropics). (b) Longwave radiative loss showing less variation with latitude due to meridional heat transports and more vertical variation because the atmosphere is more opaque to longwave than to shortwave radiation. (c) Net radiation distribution. Corresponding increments (d) – (f) to (a) – (c) due to the presence of clouds assigned to levels and latitudes based upon satellite observations from 1985-1989. Compare tops of (a+d) and (b+e) with Figure 3.8a and top and bottom of (a+d) with Figure 3.6a. Reproduced from Zhang et al. (2004).